Analysis and Control of Flapping Flight: from Biological to Robotic Insects[1]

by

Luca Schenato

Laurea (University of Padua), 1999

A dissertation submitted in partial satisfaction of the
requirements for the degree of
Doctor of Philosophy

in

Engineering - Electrical Engineering and Computer Sciences

in the

GRADUATE DIVISION
of the
UNIVERSITY of CALIFORNIA at BERKELEY

Committee in charge:

    Professor Shankar S. Sastry, Chair
    Professor Ronald Fearing
    Professor Andrew Packard

Fall 2003

The dissertation of Luca Schenato is approved:

_____

Chair   Date

_____

Date

_____

Date

University of California at Berkeley

Fall 2003

Analysis and Control of Flapping Flight: from Biological to Robotic Insects[1]

Copyright 2003

by

Luca Schenato

Abstract

Analysis and Control of Flapping Flight: from Biological to Robotic Insects[2]

by

Luca Schenato

Doctor of Philosophy in Engineering - Electrical Engineering and Computer Sciences

University of California at Berkeley

Professor Shankar S. Sastry, Chair

This dissertation explores flapping flight as an effective form of locomotion for unmanned micro aerial vehicles (MAVs). Flapping flight is analyzed from three different perspectives: biological, technological and control-theoretic. To the author's knowledge, this dissertation is one of the first attempts to study flapping flight from a control theory perspective.

From a biological perspective, the extraordinary maneuverability of many flying insects is the result of two main factors: (1) their ability to generate and control the production of large aerodynamic forces and torques from unsteady state aerodynamic mechanisms unique to flapping flight, and (2) a hierarchical architecture for their sensory and neuromotor systems. Inspired by real insects, this dissertation proposes a similar hierarchical architecture for the design of a control unit for micromechanical flying insects (MFIs). By combining averaging theory and biomimetic principles, it is shown that flapping flight allows the independent control of five degrees of freedom out of a total of six, as suggested but never experimentally confirmed by many biologists.

From a technological perspective, it is shown that a simple proportional feedback is sufficient to stabilize a wide range of flight modes such as hovering, cruising and steering. This is done under the assumption of the linearity of the wing-thorax dynamics and that the feedback's gain is a periodic function with the same period as the wingbeat. This is vital to the successful implementation of flight controllers given the limited computational resources available on MFIs. Moreover, the controller design methodology developed here is not limited to the mathematical models of aerodynamics considered in this thesis, but can be easily adapted to experimental data as it becomes

available.

      Finally, from a control-theoretical perspective, flapping flight is proposed as a compelling example of high-frequency control of an underactuated system present in nature. Averaging theory and separation of timescales is applied rigorously to ground the controller design approach and to highlight trade-offs between mechanical efficiency and overall responsiveness of the body dynamics.

Professor Shankar S. Sastry
Dissertation Committee Chair

To Beatrice

Acknowledgements

It is an arduous task to name and thank all the people who contributed to this achievement. That serendipitous decision to come to Berkeley more then six years ago turned out to be one that permanently changed my life, on a professional as well as personal level.

Berkeley, with its diverse, stimulating and constantly changing crowds of like-minded souls, has been an inextinguishable source of academic and personal challenges for me. I would like to thank first and foremost my girlfriend Beatrice for her continuous presence, support and encouragement. Also I would like to thank my family, whose love and attention made the time and distance between us appear much less than it really was.

A sincere and special thank you is owed to my advisor and mentor Shankar Sastry. He was the first to believe in my potential, and without him I would not be here today writing these lines.

I am also deeply grateful to Kameshwar Poolla, who, with his generosity, wisdom and sincerity has not only mentored me, but has also presented a constant example of how to be a wonderful human being.

Among all the many friends I made in Berkeley, I would like to particularly thank Bruno Sinopoli, with whom I not only shared the desk but also the many ups and downs of being a foreigner in a foreign land. Thank you, Bruno, for enduring my seemingly endless worries and complaints of what was actually a very quick six years.

I am also very grateful to my longtime house-mate Francesco Fornasiero for his altruism, generosity and help in times of need. And I cannot forget my computer gurus, Claudio Pinello and Alessandro Pinto, who spent many hours with me fighting Windows over the years.

I am also greatly indebted to my friends Charlotte Ley and Ranjana Sahai for spending all their spare time proofreading and editing this dissertation. I would like to thank Professor Fearing, all the guys in the MFI group, in particular Domenico Campolo, Xinyan Deng and Wei Chung Wu, who all shared in the complex layers of frustration and gratification of our group projects.

Last but not least, I want to remember Alessandra Nardi, Jin Kim, Dino Bellugi, Gianluca Donato, Andrea De Michelis, Rebecca Soffer, Anna Gatti, Ayako Yamazaki, the IISA "active" members, and all the countless number of friends that I met over the years and who all helped make my stay in Berkeley one that I will treasure and remember forever.

Contents

List of Figures

List of Tables

Chapter 1

Introduction

Who hasn't fruitlessly tried to catch an annoying fly? Or been amazed by mosquitos that seem to zigzag at incredible speeds only to stop suddenly and hang motionlessly in the air for interminable amounts of time? Who hasn't witnessed houseflies performing acrobatics while playing with one another? Everyone wondered at least once how such small and apparently simple animals can exhibit behaviors and aerial maneuvers so complex that they remain unmatched by any other animal group or manmade vehicle. Somebody has gone beyond this question and has wondered whether it is technologically feasible to fabricate a centimeter-size robotic flying vehicle with flapping wings that can replicate at least in part the extraordinary performance of flies. In fact, autonomous centimeter-size flying devices with the agility of flies would be beneficial for surveillance applications and for the monitoring of urban or cluttered environments where humans or larger autonomous vehicles like helicopters cannot penetrate or are too hazardous.

The goal of this dissertation is to analyze flapping flight in biological insects in order to develop a methodology for designing a flight control unit for robotic insects. It is the result of the work performed within a larger and ambitious project under way at the University of California, Berkeley, the Micromechanical Flying Insect (MFI) project. This main goal of this project is to fabricate a fully autonomous centimeter-sized flying robotic insect similar to a blow-fly that is capable of performing complex tasks such as searching and exploration [82]. The study of insect flight was used as the guideline for this work to propose a general theoretical framework for flapping flight that includes engineering constraints arising from the physical design. Therefore, it is not designed to mimic exactly biological insect flight control mechanisms, but rather to present a robotic insect flight control framework which is biologically inspired and technologically feasible.

A deeper understanding of flapping flight and the control mechanisms involved, is ex-

tremely valuable from three different perspectives: biological, technological and theoretical.

From a biological point of view, flapping flight is one of the most fascinating forms of biological locomotion. Analogously to aquatic locomotion, it relies on the interaction of some undulatory motion of body appendages or the body itself with the surrounding fluid. However, unlike fish locomotion where the animal weight can be balanced by the body buoyancy, flight insects needs to flap their wings to stay in air. In addition, flies can move in any direction in space, rotate their body rather easily, hover motionlessly, cruise at speeds of $1 - 10\frac{m}{s}$, fly upsidedown or backward, and perform a 90^0 change of direction within $50ms$. This is remarkable when one considers that the wings appear to move almost symmetrically and with the same periodic pattern most of the times.

The superior maneuverability of flies is the result of several factors: the enhanced aerodynamic force production of flapping flight at centimeter and sub-centimeter scale, the sophisticated neuromotor control system the allows large mobility of wings, and an heterogeneous sensory system that can quickly process external information. A vast literature in the biological community has appeared about insect flight. Paper topics include: aerodynamics, insect morphology and physiology, neuro-muscular mechanics of steering muscles, tethered and free-flight wing kinematics, neuromotor flight control system, sensory system and its interaction with the wings control. This literature is continuously being updated and many open questions still remain, however, in particular about the visual and inertial mechanosensory fusion in flight equilibrium and voluntary maneuvers. Biologists have proposed several hypotheses, but they can be tested only indirectly and with great difficulty on real insects, since they cannot be "controlled" directly. A mathematical framework of insect flight, such as the one proposed in this dissertation, could be used to validate or dismiss some of the proposed hypotheses.

From a technological point of view, there is a growing interest in biological and biomechanical locomotion. In fact, although aerial, terrestrial and aquatic manmade vehicles built on mechanisms such as rotors, fixed wings with jets, propellers, and wheels have achieved remarkable success, animals are still unmatched by man in many areas of performance. Fish locomotion exhibits silentness, hydrodynamic efficiency and maneuverability hardly matched by propeller-based underwater vehicles. Hexapodic locomotion shows incredible adaptability to different terrains and can overcome barriers unlike similarly sized wheeled-vehicles. Flapping flight locomotion, in addition to its maneuverability, applies to sub-centimeter sizes, which is more then a order of magnitude smaller then the smallest flying machine available today. Therefore, these untraditional forms of locomotion are appealing in unmanned and autonomous navigation for exploration of difficult environments such as seabeds, rocky and uneven terrains such as the Mars surface, and areas im-

penetrable by meter sized vehicles.

The reasons why only few examples of biomimetic locomotion in manmade vehicles are present today are numerous. One reason is technological since it is difficult to replicate the mechanical actuation of animal bodies or appendages. For example, it is not trivial to fabricate a mechanical structure that provides each wing with three or even two degrees of freedom as in insects, and only recently have new materials and tools been available to overcome this problem. The other reason is computational since, unlike in the mechanisms in current manmade vehicles, a direct actuation of the body appendages in the animals does not translate to locomotion in a straightforward manner. For example, rotation of a wheel corresponds to a direct translation of a car, while the undulatory motion of wing or a fin can result both in translation or rotation depending on the exact trajectory of the oscillation. In fact, only two wings are necessary for some insects to be able to move and rotate in any direction, and only the undulatory motion of the body is necessary for a eel to swim. As a consequence, common design tools for locomotion control and navigation in manmade vehicles do not help in biomimetic locomotion control. Current research in biomimetic locomotion control theory is aimed to fill this gap by developing theories and tools that can help the engineer to efficaciously design biomimetic locomotion vehicles. One of the goals of this dissertation is to reframe in a simple and yet accurate manner the main features of insect flight that can be used to evaluate different designs and navigation strategies.

From a theoretical point of view, many forms of biological locomotion belong to the class of *underactuated nonlinear mechanical control systems*. As the name suggests, these systems possess a number of inputs that is smaller then the number of degrees of freedom of the system, yet these systems can reach any configuration. Underactuated nonlinear control systems are challenging for several reasons. They are uncontrollable when linearized about an equilibrium and not all desired trajectories are feasible. However, the most limiting property is that many of these systems cannot be exponentially stabilized by any continuous feedback law. Although it has been shown that discontinuous feedback and time-varying feedback control can exponentially stabilize these systems, very few tools are available today to synthesize such controllers systematically. Besides, the diversity of locomotive mechanisms present in nature is difficult to capture into a unified framework, thus complicating the matter further.

Concurrently, research based on differential geometry and nonholonomic mechanics, which exploits the rich structure of these systems, has resulted in general and systematic analysis tools. Moreover, recent attention to periodic time-varying feedback has drawn attention to the averaging theory of dynamical systems, which seems to fit the quasi-periodic undulatory nature of biological

locomotion such as fish swimming and insect flapping flight. The current trend is to merge all these different disciplines into a general framework for a control-theoretic purposes. Flapping flight in particular is an excellent testbed to investigate nonlinear underactuated control system theory and to validate controller design tools. This dissertation is aimed at providing a systematic and rigorous methodology to design stabilizing feedback laws for flapping flight based partially on real insect observations, and to propose flapping flight as an example of underactuated control system present in nature.

The work in this dissertation looks at flapping flight control from all three different perspectives - biological, technological and theoretical, and is meant to give a holistic view of flapping flight that can benefit the engineer as well as the biologist and the theoretician to some extent. It is meant to be sufficiently self-consistent and the prior knowledge about the three areas by the reader is assumed to be minimal. Many topics, in particular those related to nonlinear underactuated control systems theory, are not treated in depth on purpose. This is done to make this dissertation more readable for those who are not familiar with a specific area, while still including the essential features and intuitions behind the scientific concepts.

1.1 Related Work

The research presented in this dissertation builds upon a diverse array of literature that ranges from biology to geometric control theory.

1.1.1 Insect flight

Aerodynamics

The aerodynamics of insect flight is substantially different from the aerodynamics associated to manmade fixed and rotary-winged vehicles. Traditional steady state solutions of hydrodynamics equations fail to give reasonable answers. This inconsistency between theory and experimental evidence generated the famous paradox which says that according to laws of physics bumble bees cannot fly, but since they don't know that, they do fly. Progress in understanding insect flight has been hampered by the difficultly of performing experiments with live animals because of their size. Research on the aerodynamics of insect flight gained momentum in 1980's with the seminal work by Ellington [27], who used force balancing arguments to estimate mean aerodynamic forces and coefficients. Another shift in understanding insect aerodynamics happened in the 1990's

thanks to the fabrication of dynamically scaled models of insect wings [24] [84]. These are robotic wings that are scaled to work in the same aerodynamic regime as insects. Besides being larger and slower then their biological counterpart (around 20-30 centimeter long and with a wingbeat frequency of about 0.2-2Hz), they can be used for controlled experiments to visualize the motion of the surrounding fluid or to measure directly the aerodynamic forces. The results of these experiments proved the existence of three main aerodynamics mechanisms [64] [6] [7] [28]. These mechanisms, namely the delayed stall, the rotational lift and the wake capture, result from the non-steady state nature of flapping flight. This pattern of flight produces larger aerodynamic forces at large angles of attack than those predicted by steady-state theory. Recently, numerical solutions of hydrodynamics equations for flapping flight confirmed the same observations [59] [71], thus reinforcing the validity of the experimental results obtained by mechanical scaled models. Although these aerodynamic mechanisms are non-steady state, Sane [64] showed that a quasi-steady state model based on steady-state equations, whose force coefficient are modified according the experimental results, can reasonably predict the instantaneous aerodynamic forces due to delayed stall and rotational lift during the course of a wingbeat. This is extremely valuable since simple models can be use to simulate aerodynamic forces given the wing kinematics without the necessity of using complex finite element solutions of the partial differential equation regulating flapping flight aerodynamics.

Wing Kinematics

Insect wings exhibit three degrees of freedom: they can flap back and forth, can rotate about the wing longitudinal axis, and can deviate from the stroke plane so that the wing tip can follow flat, elliptical, banana-like or figure-eight trajectories [27] [26]. The motion is actively determined by a complex structure of multiple groups of muscles that generate a rich set of wing kinematics [78] [25]. Since wing kinematics directly determine the generation of aerodynamic forces along the wingbeat, Dickinson *et al.* have tried to identify common kinematics patterns that are associated with specific maneuvers and body dynamics in tethered insects [23] [19] [43] [84] and during free flight [31]. They showed how a few kinematics parameters such as the mean angle of attack, the amplitude of the stroke angle, the timing of rotation at the wing reversals are voluntarily changed by the insect to perform a specific maneuver or to compensate an external disturbance. Sane *et al.* investigated the effect of the variation of these kinematic parameters on the aerodynamic force production by experimentally measuring aerodynamic forces with a dynamically scaled model of wings called Robofly [63]. They also suggested how these parameters could be used to actively

control the generation of mean aerodynamic forces and torques acting on the insect body.

Sensors and Visual-Mechanosensory Fusion

The remarkable maneuverability of insect flight would be incomplete without an understanding of the sensors and the neuromotor architecture responsible for the flight stabilization and navigation. Insects present different types of sensors which are related to flight. Mechanosensitive sensilla distributed along the wings can detect the wing deformation during flight [18]. Since wing deformations are directly related to aerodynamic forces acting on the wing surface, these sensors are believed to play an important role in wing kinematics optimization and fine compensation to external perturbation [34].

Two sets of sensors are directly related to flight stabilization and compensation of external disturbances: the ocelli and the halteres. The ocelli comprise three wide angle photoreceptors placed on the head of the insect [49]. They are oriented in such a way that they collect light from different regions of the sky. The ocelli act as a horizon detector by comparing the light intensity measured by the different photoreceptors [76] [36] [68]. In particular, Hengstenberg [35] have shown how a change in light distribution around an insect initiate a compensatory maneuver to counteract the external disturbance.

Halteres are two small evolutionarily modified hind wings that beat anti-phase to the wings and serve as a biological gyroscope during flight [54] [21]. The halteres beat through an amplitude of roughly 180°. As the fly rotates around the roll, pitch and yaw axes, angular velocity dependent Coriolis forces act on the beating halteres that are transduced into electrical signal by mechanosensitive sensilla at the halteres hinge. Both Dickinson [21] and Nalbach [54] observed halteres-mediated responses in head compensatory movements and in change of wing kinematics.

Halteres are not the only organs that can estimate angular velocity about the three body axes during flight. Insects are also equipped with compound eyes that provide low spatial resolution visual information. Downstream of the photoreceptors, motion-sensitive neurons in the visual system allow flies to track both small objects and large field rotations. Krapp *et al.* [41] have shown that compound eyes encode the optical flow fields that would be generated by self-motion such as forward translation, roll or pitch. The optomotor neural processing information is still not completely well understood and current research includes physiological [40], theoretical [56] and insect behavioral [57] approaches aimed to unveil it. The visual system does not only provide self-motion estimation, but also critical information for navigation [74] and object avoidance [75]. Also a very

active area of research is the visual-mechanosensory fusion of information [69] and the hierarchical neuromotor control architecture [15].

Flight Control

Explicit literature of insect flight from a strictly control perspective is not extensive, since it is generally only present in the context of complementary research on sensors or aerodynamics described above. Therefore, control architecture and algorithms can be only inferred, although some excellent reviews are available [60] [77].

1.1.2   Nonlinear underactuated control systems and Averaging Theory

Nonlinear underactuated control systems are systems that, loosely speaking, possess a number of control input that it is smaller then the number of degrees of freedom of the system, but they can be driven to any configuration with an appropriate input signal. Classic examples are wheeled and skating motion. Most of these systems arise from nonholonomic mechanics, which describes the motion of systems subject by constraints on the system velocities. Most research revolving around nonlinear control systems is concerned with controllability issues, i.e. in finding necessary and sufficient conditions that guarantee that a specific configuration (trajectory) can be reach (followed), and, even more importantly from a practical point of view, in finding algorithms that generate input signals to reach those configurations. A good review on nonholonomic mechanics from a control perspective can be found in [9] and [65]. One of the major problems of underactuated nonlinear control systems is that they cannot cannot be exponentially stabilized using continuous state feedback [12], which is one of the best understood and effective methodologies for controller design. Much success regarding the analysis and control of nonholonomic system has emerged from the tools of differential geometry [1] [45], as shown in [5] [8]. Sussmann [72] has proposed several directions to generate suitable control input signals for nonholonomic systems. In particular, he showed how high-frequency periodic signals can be used for controller synthesis of underactuated systems [73]. Stronger results and quantitative analysis using sinusoidal inputs for chained nonholonomic systems are given by Murray at al. [53].

High-frequency control relies on averaging theory tools. Sanders and Verhulst [61] give a detailed review of the averaging theory, including formulas for the average of a time-periodic vector field up to second order, as well as theorems concerning the stability of the flow of time-periodic vector fields with regards to stability of the flow due to the averaged vector field. Also a very clear

introduction to averaging theory can be found Chapter 4 of [66]. The convergence of nonholonomic control systems and averaging theory has witnessed a growing number of research papers aimed at developing a general framework for controller design synthesis [80] [13] [44] [46].

1.1.3   Control of aquatic biological locomotion

Aerial and aquatic biological locomotion are good examples of underactuated mechanical systems in which locomotion is generated by an oscillatory motion of one or a few body appendages within a viscous fluid [22] [85]. In particular, fish locomotion has attracted considerable interest because of its simplified planar dynamics, and because of possible practical applications [47]. High-frequency periodic controller design based on averaging and geometric control theory has been applied successfully to carangiform fish locomotion (such as tunas) [50] [79] and anguilliform locomotion [58] [48]. Aquatic biological locomotion presents several analogies with flapping flight locomotion.

1.2   Contribution

The purpose of this thesis is to give a coherent understanding of flapping flight by combining results and research from biology and theoretical control theory. Particular emphasis has been placed on the development of a general framework and practical tools to design a control unit for a biomimetic flapping robot.

Insect flight control   Based on models of flapping flight aerodynamics and biologically-inspired wing kinematics, it is shown that in flapping flight it is possible to independently control the three mean body torques and the vertical and forward forces by perturbing a symmetric wing kinematics. This is equivalent of saying that with flapping flight it is possible to control directly 5 degrees of freedom out of the total 6. Moreover it is given an estimate of the magnitude of mean forces and torques that can be generated with flapping flight. In particular, the model predicts linear accelerations up to $1.1 - 1.3g$ and angular acceleration up to $60,000 deg/sec^2$ which are consistent with observations in insects.

Flapping Flight Controller Design   In this dissertation a hierarchical architecture for the design of a control unit for a Micromechanical Flying Insect has been proposed similarly to the control structure observed in flying insects. The hierarchical structure simplifies the design of the overall

control unit without sacrificing maneuverability. Control of wing kinematics is posed as a tracking problem of wing trajectory that generates the desired mean torques and forces over a wingbeat. Wings trajectory are parameterized according to a few parameters that have been suggested by observation of real insects, such as mean angle of attack, timing of rotation and stroke plane amplitude. Dynamics of actuators have also been included to give a more accurate model of overall insect dynamics. The two most important aspects of the proposed design for attitude and hovering stabilization are that the overall feedback law from insect linear and angular position and velocity to the actuators input voltages is T-periodic affine, where T is the wingbeat period, and that in flapping flight it is possible to control directly the 5 degrees of freedom for the dynamics. This is very beneficial to the design of flying biomimetic robots, since computational resources on board the device are limited.

PWM control of wing actuators with single active degree of freedom   Motivated by the necessity of simplifying the mechanical design of the wing-thorax structure and the electronics driving the actuators, it is shown that a wing with a single active degree of freedom (stroke angle), and passive rotation at the inversion of motion, driven by a pulse width modulation (PWM), can still ensure controllability of five independent degrees of freedom in flight dynamics. However, the magnitude of the inputs controlling these five degree of freedom is decreased if compared with a two-degree of freedom wing analog control of the actuators.

Control of underactuated nonlinear systems   This dissertation shows how flapping flight belongs to the class of underactuated nonlinear control systems driven by high-frequency control inputs, where the inputs are the position and velocity of the wings. The main result is that an appropriate input parametrization based on biomimetic parametrization and averaging theory approximates the flight dynamics with a simpler nonlinear system that possesses a larger number of independent virtual inputs and it is amenable to standard continuous (actually linear) feedback controller design tools. The increase in the number of the controlled independent virtual inputs, namely the mean forces and torques, when moving from the exact system to the averaged system results from the fact that the inputs do not enter into the systems dynamics in an "affine" fashion. Therefore, it is possible to modulate the input trajectory within a single beat in order to affect only one direction of the force. Also, a rigorous treatment of the inclusion of actuators dynamics is given based on a multi-timescale separation of variables, which highlight tradeoffs between controllability and performance.

1.3 Outline

This dissertation is tailored for a wide audience including engineers as well as biologists interested in insect flight from a control theory perspective. Only general knowledge of classical control theory and Lyapunov stability analysis is required. The necessary tools for averaging theory are introduced when needed and references are given for the interested reader.

Chapter 2 This chapter gives an overview of flapping flight from a biological perspective. In particular, it reviews the aerodynamic mechanisms involved in flapping flight and highlights differences with fixed or rotary-winged vehicles aerodynamics, the sensory system physiology and and purpose of the most important sensors involved in flight stabilization, and the neuromotor-sensory architecture and the mechanics of in flapping flight stabilization in real insects.

Chapter 3 Chapter 3 gives an overview of flapping micromechanical flying insects. In particular, it gives an overview of micromechanical flying insects, proposes a control architecture for designing flight controllers, and introduces mathematical modeling for the flapping flight aerodynamics, the dynamics of insect body, and the wings' electromechanical actuators. These mathematical models will be used for simulations in Chapter 5.

Chapter 4 Chapter 4 introduces the mathematical background of averaging theory necessary to justify the controller design approach developed in Chapter 5. Although theorems and results are quite technical, particular attention is spent giving intuitive motivations and examples to facilitate understanding. In particular, we show that in nonlinear systems which are not affine in the control inputs, high-frequency periodic feedback can artificially increase the number of control inputs, thus approximating the original time-varying system with a simpler time-invariant system. Also, multi-timescale analysis of coupled systems with different timescale dynamics is presented to model the inclusion of actuator dynamics in the flight dynamics. Several examples are given to illustrate the theoretical results.

Chapter 5 Chapter 5 uses biomimetic principle to design wing kinematics that affect flight dynamics based on observations of real insects presented in Chapter 2. Results from Chapter 4 are then used to propose a controller synthesis for attitude control and hovering. Finally, a simpler electromechanical design consisting of pulse-width-modulation (PWM) scheme to control the wing actuators applied to a flapping wing with only one active degree of freedom and passive rotation, is

explored and it is shown that it can still guarantee controllability of flight at the price of a weaker authority on the magnitude of forces and torques that can be generated.

Chapter 6 Chapter 6 summarizes the results presented in the dissertation and discusses possible extensions, in particular from a theoretical perspective.

Chapter 2

Flapping flight in biological insects

Flies have inhabited our planet for over 300 million years, and today they account for more than 125,000 different species, so that they are one out of every tenth species known to man [26]. Their evolutionary success might spring from their insuperable maneuverability and agility, which enables them to, for example, chase mates at turning velocities of more than $3000^{o}s^{-1}$ with delay times of less than 30 ms. This unmatched maneuverability is the result of three main factors: larger aerodynamic forces generated by the flapping flight relative to fixed or rotary wings, high bandwidth and sensitivity sensors for self-motion estimation, and an effective neuromotor control architecture that quickly compensates for external flight disturbances without compromising voluntary maneuvers. We will review these aspects of biological insect flight in the next three sections.

2.1 Aerodynamic Mechanisms

The aerodynamics of flapping flight is quite different from fixed or rotary winged flight for two main reasons: the first is that the they act in two different aerodynamic regimes, and the second is that the velocity of the wing or blade relative to the fluid is time-varying. In insect flight, the Reynold's number, a dimensionless parameter that is related to fluid viscosity and wing velocity, ranges from few hundred to few thousand in insects and from few tens of thousands to hundred thousands in manmade vehicles. In addition, the velocity of the wing or blade relative to the fluid in flapping flight is time-varying, while it remains constant in fixed or rotary winged flight. Therefore, steady state hydrodynamics developed for man-made vehicles is not suitable to describe flapping flight. It seems that, according to a footnote in the history of biological sciences, researchers from the University of Goettingen, Germany, made a discovery in the 1930s that proved

it was aerodynamically impossible for bumblebees to fly. Bumblebees, of course, continued to fly about with blithe disregard for their results! The so-called "Bumblebee Paradox" became so famous that entered the public imagination, even inspiring the title of a well-known children's book ("The Bumblebee Flies Anyway", by Robert Cormier).

Although numerical solutions of hydrodynamical equations are available today [59] [71], a clear understanding of flapping flight aerodynamics have been obtained by dynamically scaled models of insect wings that can reproduce the same aerodynamics mechanisms present in insect flight [24] [84]. These experiments have unveiled three main aerodynamic mechanisms involved with flapping flight: the delayed stall, the rotational lift, and the wake capture.
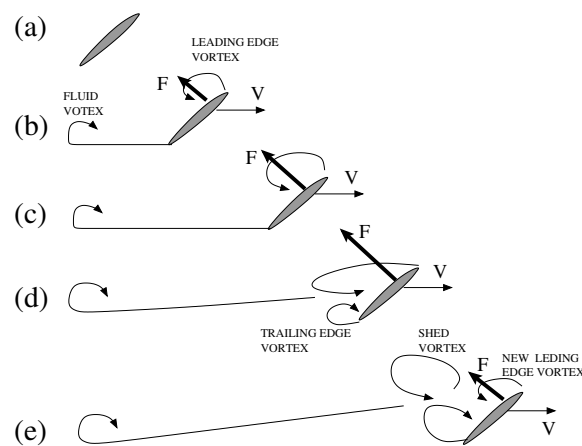
Figure 2.1: Cartoon of delayed-stall mechanism

The **delayed stall** appears at the onset of motion of the wing [20]. As the wing starts moving a small vortex appears behind the leading edge, and an asymmetric, opposite swirl appears in the fluid close to the original resting position of the wing as illustrated in Figure 2.1(b). The presence of two vortices moving in opposite directions but with identical strength is the equivalent principle of conservation of momentum for fluids. The vortex above the wing creates a lower pressure on its back surface, thus producing a net aerodynamic force perpendicular to the wing surface. As the wing moves, the vortex behind the leading edge increases along with the aerodynamic force (Figure 2.1(c)). However, after a certain distance a new vortex starts appearing behind the trailing edge to keep the total fluid momentum constant (Figure 2.1(d)). This vortex has a rotation direction opposite to that of the leading edge vortex and in turn decreases the force production. Moreover, the vortex on the leading edge keeps on increasing till it reaches a critical size at which point it

detaches from the wing and is shed into the fluid, thus decreasing even further the force production (Figure 2.1(e)). As soon as the leading edge vortex detaches, a new vortex starts appearing behind the leading edge and this process of the vortex building and detaching repeats itself endlessly.

The vortex shedding process appears after the wing has traversed a distance of a few chord lengths, therefore the increased aerodynamic force production can be captured only at the very beginning of the wing movement. Insect wings move only few wing chord lengths when they flap [27], and thus are able to capture this enhanced force production. Another very important characteristic of flapping flight is that the wings do not translate but rather rotate about their wing hinges. This means that the velocity of the wing with respect to the fluid is not constant along the wing longitudinal axis, but instead depends on the distance from the wing base. This creates a gradient of translational velocity along the wing axis. Ellington *et al.* [28] observed the presence of a base-to-tip axial flow entrained by the leading edge vortex, and argued that this property helps the stability of the leading edge vortex. In contrast to the fixed winged vehicles for which large angle of attacks give rise to turbulence, the leading edge vortex is stable for angles of attack up to 90 degrees. The aerodynamic force generated is an increasing function of the angle of attack [20]. The last important difference of delayed stall relative to fixed-winged vehicles is that the aerodynamic force is almost perpendicular to the wing profile rather then perpendicular to the wing velocity.

The **rotational lift** mechanism is the result of a combination of the translation and rotation of the wing [64]. This mechanism is analogous to the one that allows a ball to curve when it is thrown with some spin, as commonly seen in baseball or tennis. In fact, an aerodynamic force perpendicular to the translational velocity appears if the ball has a back-spin as shown in Figure 2.2. The magnitude of the aerodynamic force generated by the rotational lift is approximately proportional to the product of the angular velocity and translational velocity. However, there is a major difference between a rotating wing and a rotating ball. In fact, while the rotational lift is perpendicular to the velocity in a rotating ball, the rotational lift is perpendicular to the surface of
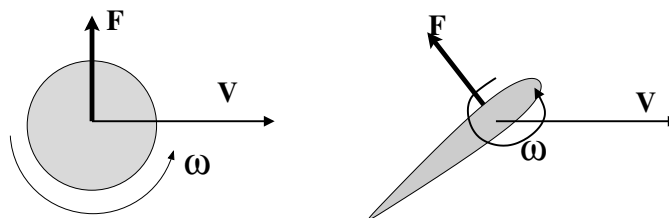
Figure 2.2: Rotational lift for a rotating ball and for a rotating wing

a rotating wing. Rotational lift is present in flapping flight at the end of each half-stroke when the wing is about to invert the direction of its motion.

The last mechanism present in flapping flight is the **wake capture** [6] [7]. It is present at the beginning of each half-stroke after the wing has inverted its motion and started to move. The wake capture appears when the wing interacts with the effects of past strokes on the ambient fluid environment. The fluid behind the wing is dragged along with the motion of the wing, as shown in Figure 2.3. As the wing slows down and inverts the direction of motion, it hits the fluid which is still moving because of its momentum. Therefore, the velocity of the wing relative to the fluid (which corresponds to $V - W$ using the notation of Figure 2.3) is larger than the velocity of the wing alone, and therefore results in the generation of a larger force. This is a simplified explanation of the principle behind the phenomenon of wake capture, and an interested reader should look to the work of Birch *et al.* for further insight [6]. The contribution of each of these three aerodynamic
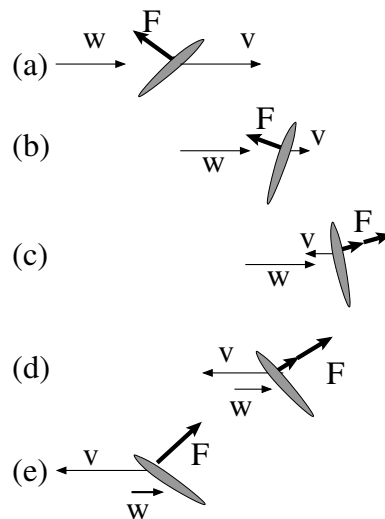
Figure 2.3: Cartoon of wake capture mechanism. *V* and *W* indicate the velocity of the wing and of the fluid wake relative to an inertial frame, respectively. Total velocity of the wing relative to the fluid is given by $V_{tot} = V - W$.

mechanisms has been measured using a dynamically scaled model of a wing [24]. Figure 2.4 shows the total aerodynamic forces for three representative wing kinematics, where the wing motion is the same for all three but the timing of the rotation of the wing is advanced, symmetrical and delayed, respectively, relative to the inversion of motion. It also artificially decomposes the total force according to the three different mechanisms. It is clear that the delayed stall accounts for most of the aerodynamic force production and that the rotational lift and wake capture are present only
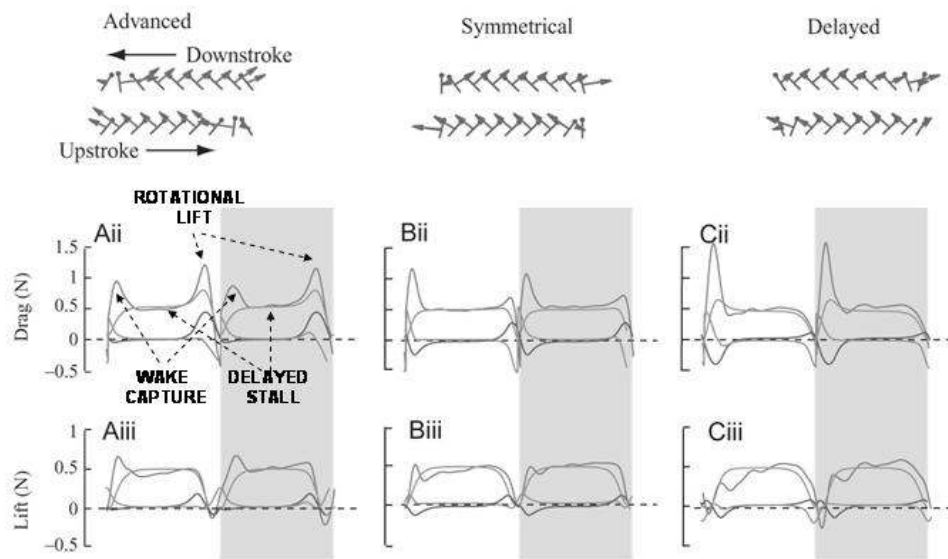
Figure 2.4: (*Top*) Wing kinematics diagram for three different wing trajectories in which the rotation of the wing is advanced, symmetric or delayed relative to the inversion of wing motion. (*Center and Bottom*) Aerodynamic drag and lift forces as measured by Robofly, a dynamically scaled model of an insect wing, during the course of a full wingbeat. The gray area corresponds to the upstroke portion of the wingbeat. Arrows indicate how specific aerodynamic mechanisms act during flapping flight. Courtesy of [24].

for the short period of the stroke when the wing rotates and changes direction of motion. Although these two mechanisms contribute only marginally to the mean lift, they play an important role in flight control since they can affect the distribution of forces.

2.2   The Sensory system

Flying insects possess a diverse set of sensors, ranging from mechanoreceptive to optical, and from inertial to chemical. Each of these sensors is dedicated to a specific task that ranges from flight stabilization to navigation.

Mechanoreceptors   Insects wings and other parts of the body such as the antennae, neck and legs are innervated by campaniform sensilla. These nerves can sense and encode pressure forces when they are stretched or strained [17] [18] (see Figure 2.5). A large number of sensilla are located at the base of the wing. They are thought to be able to measure aerodynamic forces acting on the wings during motion and to elicit a compensatory mechanism to stabilize flight as observed

by Hengstenberg [34]. In principle, these sensors could also be used by insect to compensate for external disturbances, although this has not been confirmed experimentally.
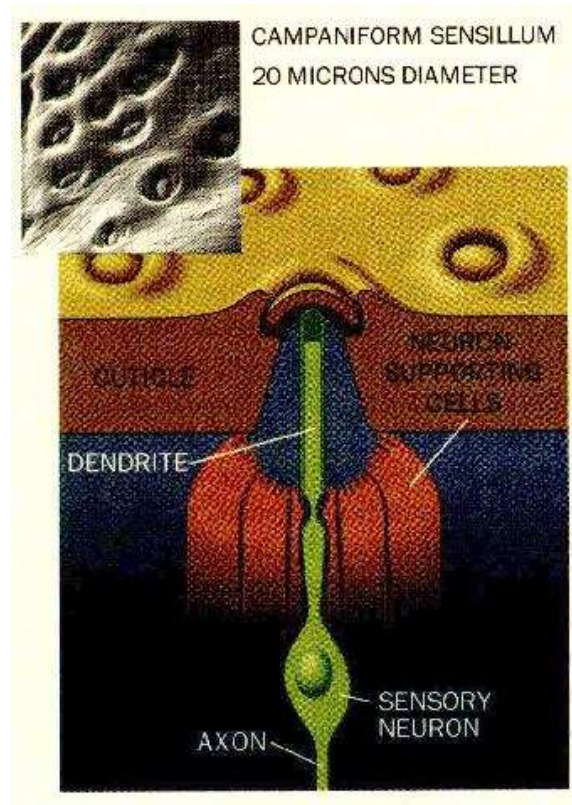
Figure 2.5: (*Top-left corner*) Microscope photo of campaniform sensilla on fly wing. (*Center*) Graphical rendering of sensilla structure.

Ocelli   Ocelli are a sensory system present in many flying insects [49]. This system comprises of three wide angle photoreceptors placed on the head of the insect (see Figure 2.6). They are oriented in such a way that they have poor image resolution, but are able to collect light from large regions of the sky. Although the exact physiology of ocelli and their role in insect flight is still not completely understood, it is believed that they play a fundamental role in insect attitude stabilization, particularly horizon stabilization [68] [36] [76]. Experimental results performed by Taylor [76] and Kastberger [36] on some insect species suggest that ocelli collaborate synergistically with compound eyes to minimize the delay of visual processing and to augment visual responsiveness when no sharp horizontal border is present. When an insect is presented with a moving artificial horizon,
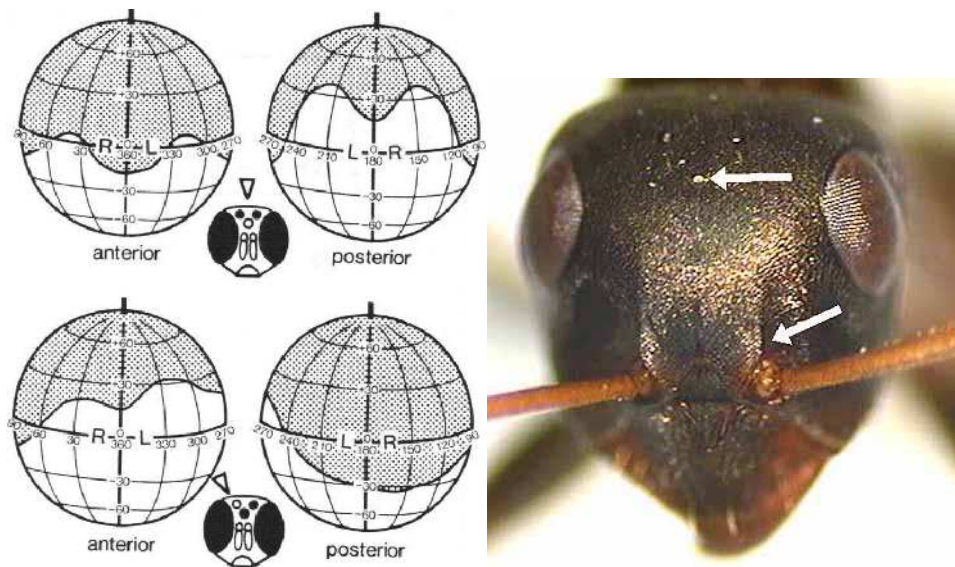
Figure 2.6: (*Left*) The ocelli of a blowfly and the visual fields of the median (top) and right lateral (bottom) ocelli. Courtesy of [68]. (*Right*) Photo of *locust* head and locations of ocelli photoreceptors.

it first tries to rotate its head in order to fixate the horizon on the retina. Only afterwards does it change its wing pattern to realign its abdomen with its head. Taylor observed that cauterization of ocelli doubles the latency between the horizon motion and the compensatory head movement. Moreover, in dimly lit environments ablated ocelli reduced insect sensitivity to horizon motions and resulted in a smaller mean amplitude of head motion. It can therefore be concluded that ocelli are especially important for the stabilization of the retinal image of the compound eyes during flight when disturbances are sudden and frequent. It seems that the high sensitivity to light and the quick response time of ocelli comes at the expense of acuity.

Two additional findings observed by Taylor [76] deserve mentioning. First, in cases where an insect had ablated compound eyes and intact ocelli and experienced an inverted horizon corresponding to that of an upside-down insect, its head remained motionless until the two lateral ocelli were unequally illuminated. This is the opposite reaction of insects with intact compound eyes. Second, an insect with disconnected compound eyes and intact ocelli quickly responded to the sudden displacement of the horizon, but quickly relaxed back in the rest position even when the horizon remained displaced. Animals with intact compound eyes kept their heads rotated. This observation suggests that the ocelli behave similarly to a high pass filter. This could be due to the fact that light distribution can change substantially during the course of the day as a result of sun motion, atmo-

spheric variations or simply because the insect during its flight has gone out from under a shady area. Nonetheless, these variations have a long timescale relative to the insect motion timescale and can be compensated for by the compound eyes. From an engineering perspective, insects combine low-bandwidth compound eyes with high-bandwidth ocelli to obtain an accurate horizon sensor for attitude stabilization over a large frequency domain.

Biologists believe that ocelli estimate the orientation of the insect with respect to the sky by comparing the intensity of light measured by the different photoreceptors. Their argument is based on the assumption that the intensity of light measured by the photoreceptors is only a function of its latitude relative to the light source.

Halteres Research on insect flight revealed that in order to maintain stability insects use structures called halteres which detect body rotational velocities by measuring gyroscopic forces. [34]. The halteres of a fly are located in its hindwings, and are hidden in the space between thorax and
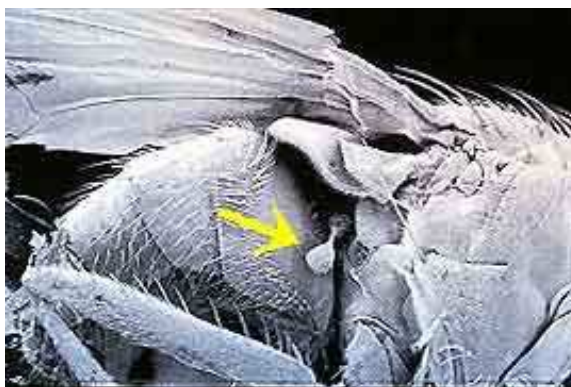
Figure 2.7: Photo of haltere in *Musca domestica*

abdomen where the air current has a negligible effect on them (see Figure 2.7). Halteres look like small balls attached to the end of thin rods. There are about 400 sensilla embedded in the flexible exoskeleton at the base of each haltere. These mechanoreceptors function as strain gauges to detect the Coriolis force exerted on the halteres [30]. During flight, the halteres beat up and down in vertical planes at an angle of nearly 180° anti-phase to the wings at the wingbeat frequency. When a fly's halteres are removed or immobilized, it quickly falls to the ground. In addition, the two halteres of a fly are non-coplanar (each is tilted backward from the transverse plane by about 30°). This non-coplanarity of the two halteres is essential for a fly to detect rotations about all three turning axes. In

fact, a fly with one haltere removed is unable to detect rotations about an axis perpendicular to the stroke plane of the remaining haltere [54]. Mathematical investigations and numerical simulations of the signal processing of the halteres presented in [67], confirm the idea that insects can indeed estimate the three components of the angular velocity.

2.3 Neuromotor Architecture of Flight Control

The extraordinary maneuverability exhibited by flying insects is the combination of a sophisticated neuromotor control system with highly specialized sensors. Presently little is known
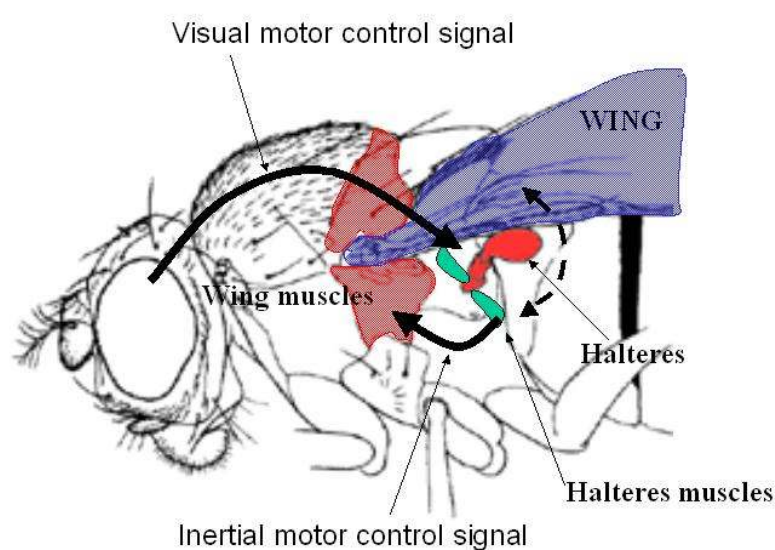
Figure 2.8: Neuromotor control physiology in flying insect.

about the flight control mechanisms and neuromotor physiology in real insects [15] [29] [26]. Experimental evidence suggests the existence of at least two levels of control, a hiher and a lower level as shown in Figure 2.8. At the lower level the halteres and the ocelli directly control the wing muscles in order to keep stable flight orientation. This lower level of control seems to be reactive, since it mediates corrective reflexes to compensate for external disturbances and maintain a stable flight posture. At the higher level, the brain, stimulated by visual and physiological stimuli, plays the role of the navigator, and plans a trajectory based on a goal such as foraging or chasing a mate. Different from the halteres-ocelli system, the visual system is connected directly to the halteres muscles rather than to the wing muscles. Therefore, the higher level of control indirectly affects

the flight behavior by influencing the motion of the halteres and thus creates an apparent external disturbance for which the lower level of control would try to compensate. This structure is similar to that between vestibular-ocular reflexes and active head rotation in vertebrates [62]. The reason for this hierarchical control architecture is that it is an efficient resolution to the conflict between flight stability reflexes while generating goal-orientated manoeuvres. Without some appropriate change in efficacy, haltere-mediated equilibrium reflexes would function to counter goal-orientated motion. To resolve this potential conflict, the nervous system must contain the means of attenuating equilibrium reflexes during the generation of controlled manoeuvres.

A third, even lower, level of control could exist in the pressure sensors that innervate the wings and haltere. These sensors perceive the aerodynamic forces acting on the wings. This bottom level serves to adjust the motion of a wing while it beats in order to improve aerodynamic efficiency and compensate for local turbulence [34].

2.4   Mechanics of Insect Flight Control

Insect flight control has been studied extensively from a physiological perspective, but its mechanics are less well known. Even when the given stimulus of the kinematic changes of a wing are defined, their consequences on the aerodynamic force production mechanisms often remain obscure. Moreover, although flapping flight shares many similarities to helicopter flight, it is not clear weather they have the same control strategy. The two most important unanswered questions about flapping flight today are how many degrees of freedom flying insects independently control and what are their available control inputs. The difficulty in answering these questions resides in the limited quantitative information available about insect flight. In fact, accurately reconstructing three-dimensional wing kinematics presents formidable technical difficulties, even if the insect is tethered. Only in a few experiments have direct measurements of the three forces and three moments on tethered insects been correlated with the observed changes in wing kinematics. Finally, accurate measurements of the position of the center of mass and moments of inertia have been rarely recorded. Nonetheless, Taylor [77] does offer several references and some qualitative observations, and these are summarized in this section.

The first point to note is that hovering insects, like hovering helicopters, possess no first-order passive stability about any axis. This is because the resultant flight force vector passes through the center of gravity at equilibrium and remains fixed in magnitude, position and direction with respect to the body axes as the insect's orientation changes [77]. Although second-order changes in

aerodynamics forces caused by translation or rotation of insect could in principle be present, no empirical data is available to corroborate this hypothesis. Even in the case that flapping flight possesses some form of passive stability, it is likely that it would be underdamped, as in modern aircrafts, and active control would be necessary to quickly damp out undesired oscillations. Therefore, active flight control is necessary not only for voluntary maneuvers, but also for flight stabilization in the presence of external disturbances.

The second point is that, unlike helicopters, which independently control rotations about the three body axes, insects vary symmetrically the motion of the wings in order to control the longitudinal forces and rotations, and asymmetrically in order to control lateral forces and rotations. The result is an effective doubling of the number of control inputs and a remarkable economy of control. From this observation it is clear that the longitudinal control in insects is independent of lateral control, i.e. pitch and vertical force can be controlled independently from roll and yaw. This is sufficient for an insect to move in space, since pitch control indirectly controls forward thrust generation, as in helicopters, the vertical force controls the altitude, and the roll-yaw controls the heading.

The third point is whether insects can independently control roll and yaw. This has been proven only be larger flies [81]. Independent control of roll and yaw indirectly implies that the insect can control lift and thrust generation independently on each wing. In fact, if lift and thrust can be controlled independently, asymmetric thrust generation would produce a yaw torque, and asymmetric lift generation would produce a roll torque. Moreover, independent lift and thrust generation implies that insects can control vertical and longitudinal forces independently, without necessarily changing the pitch. As a consequence, if an insect can independently control the yaw, roll and pitch moments, it can independently control vertical and longitudinal force, also. Therefore, insects can control five-degrees-of-freedom, which is from helicopters that can control only four, i.e. the three torques and the vertical thrust.

The fourth point regards which are the kinematic parameters that insects can control and how these parameters affect the generation of forces and torques. *Stroke amplitude* is normally considered the main control parameter that determines aerodynamic force output, in particular lift. Flies have been observed to change the amplitude of the stroke by adjusting the lower turning point of the wings. In fact the amplitude increases or decreases as the wings sweep more or less far forward on the downstroke [55]. This causes the center of mean lift to shift backward as well, thus creating a nose-down pitch moment.

Drosophila melanogaster is also able to vary the *offset of the stroke amplitude* independent

of amplitude, i.e. it can shift the wing motions forward or backward relative to its body. This mechanism should allow pitch to be modulated independently of its aerodynamic force output [88]. Stroke amplitude can be used by insects also to produce roll moments. In fact, the amplitude of the inside wing is reduced to shorten the stoke and to therefore reduce the aerodynamic force. The opposite changes occur on the outside wing, and the combination of these changes creates roll torques through an asymmetric lift production [55].

Timing of rotation is another important kinematic parameter for force control. Several species of insects have been observed delaying the rotation of the inside wing and advancing the rotation of the outside wing during maneuvers [23]. Moreover, experiments with model wings [24] have demonstrated that the timing of supination relative to stroke reversal (the point at which wing translation reverses direction) is critical in determining the magnitude of the forces produced. In particular, it affects thrust production more dramatically then lift production and thus suggests that the timing of rotation is a means to control lift and thrust independent of one another. In fact, the timing of supination seems to be independent of stroke amplitude in Drosophila melanogaster.

In addition to varying their wing kinematics, flies may control pitch by varying their *posture* [88]. Drosophila melanogaster elevate their abdomen in response to nose-down disturbances, displacing the position of the center of mass behind the axis of mean aerodynamic force, thus creating a nose-up moment. Some flies have been observed moving their legs during pitch stabilization in order to change the overall posture of their body. The change of posture could be the result of conservation of total body angular momentum, or the result of drag moments generated by the interaction of the legs with the air.

2.5 Conclusions

In this chapter, we reviewed some of the aspects related to flapping flight in biological insects. While aerodynamic mechanisms are well understood, the neuromotor and sensor fusion architecture and the mechanics of insect flight control are still being investigated. Nonetheless, some interesting observations have already emerged. In particular, there is a growing consensus that the neuromotor architecture possesses a hierarchical structure that is an optimal system for balancing the conflicting nature of an active navigation system with a reactive system necessary for coping with a reactive system necessary to cope with external disturbances. The active navigation commands from the visual system and the brain do not directly control the wing muscles, but do indirectly affect them by influencing the ocelli and halteres sensors that, in turn, control the wing

muscles. This architecture has been adopted as a model to design the flight control unit for a robotic flapping insect proposed in the next Chapter.

Also very relevant to the design of flight controllers for robotic insect, is an analysis of the biomechanical parameters and the mechanisms of wing motions that allow insects to generate net forces and torques to control the body dynamics. Although literature of the Biology community gives only qualitative descriptions of these mechanisms, they are fundamental to controller design since they suggest effective parametrization of wing motions to generate the desired body motions. Some of these biomechanical parameters will be used in Chapter 5 to design wing trajectories and we will show, using quantitative evidence based on simulations of the aerodynamic mechanisms, how these parameters indeed allow very effective control of body dynamics.

Chapter 3

Micromechanical Flying Insects: Control Architecture and Modeling

The recent interest in micro aerial vehicles (MAVs) [51], largely motivated by the need for aerial reconnaissance robots inside buildings and confined spaces, has led to the development of inch-size flapping wing MAVs that mimic at least part of the extraordinary performance of insect flight. This is a challenging endeavor for several reasons. The aerodynamics for inch-size flapping robots differ greatly from manmade fixed- or rotary-winged vehicles. Size constraints forbid the use of rotary electric motors and commercial inertial navigation system (INS), global positioning system (GPS) and cameras. Flapping frequency beyond $100Hz$ requires sensors and processing algorithms with bandwidth and sensitivity at least one order of magnitude higher than those usually found in today's aircrafts. And finally, energetic and computational constraints limit the choice of sensors and algorithms that can be feasibly designed. Even more challenging is the fabrication of fully autonomous vehicles capable of performing complex tasks such as the navigation and the exploration of an unknown environment. It must be pointed out that insects in nature constantly perform such tasks efficiently and efficaciously with little regard to their difficulty, and, consequently, provide an invaluable source of inspiration for the design of MFIs. In this chapter we give a brief overview of micromechanical flying insects (MFIs). We use the biological insights presented in the previous chapter to develop a general framework for the design of a flight control unit which enable MFIs to accomplish complex autonomous tasks such as searching, surveillance and monitoring. Finally, we give the mathematical models for insect aerodynamics, body dynamics and actuators dynamics that will be used in Chapter 5 to test the design of the controllers and to evaluate their performance via

simulations.

3.1 Overview

The design of the MFI is guided by studies of real flying insect studies, however. The challenges of a successful fabrication of a MFI includes such limitations as: small dimensions, low power consumption, high flapping frequency, and limited computational on-board resources. These have forced the development of novel approaches to electromechanical design and control algorithms and the adoption of new technologies. The goal of the MFI project is the fabrication
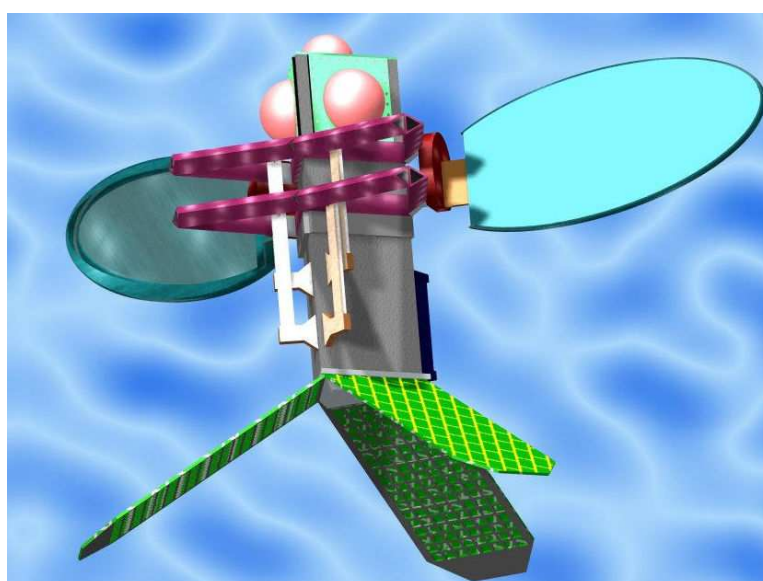
Figure 3.1: MFI artist's conception. Courtesy of R. Fearing.

an electromechanical device capable of autonomous flight and complex behaviors, specifically one that mimics the blowfly Calliphora. Figure 3.1 shows an artist's conception of the MFI prototype. The fabrication of such a device requires the design of several components. It is possible to identify five main units (Figure 3.2), each of which is responsible for a distinct task: the *locomotory unit*, the *sensory system unit* , the *power supply unit*, the *communication unit* and the *control unit*.

The locomotory unit, composed of the electromechanical thorax-wings system, is responsible for controlling the motion of the wings and therefore, for indirectly generating the necessary aerodynamic forces for the flight navigation. One of the most challenging parts of this project is the design of the mechanical structure which provides mobility to the wings efficient enough to
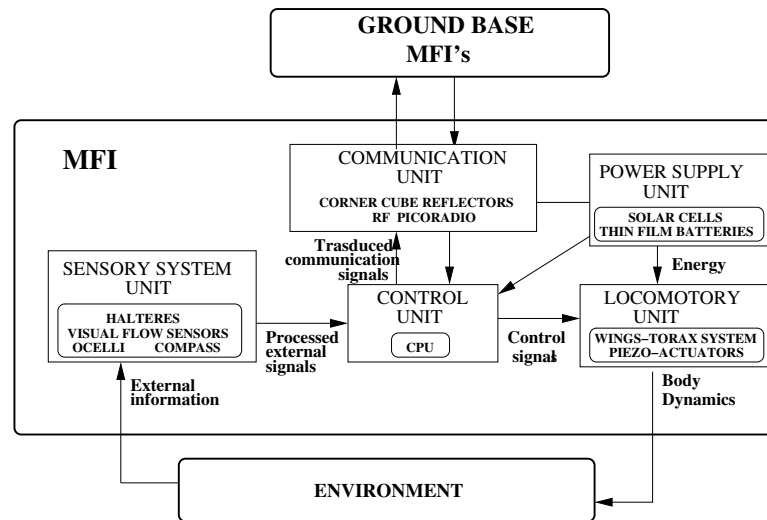
Figure 3.2: MFI structure

generate the desired wings kinematics. This issue is not in the scope of this dissertation and we recommend the interested reader to more detailed work [3] [4] [87]. The current design provides two independent wings with two degrees of freedom: flapping and rotation.

The sensory system unit is comprised of different sensors: the halteres, biomimetic gyros for angular velocity detection; the ocelli, biomimetic photosensitive device for roll-pitch estimation; the magnetic compass for heading estimation; and the optical flow detectors for self-motion detection and object avoidance. These sensors provides the control unit with the input information necessary to stabilize flight and to plan desired trajectories. Other kinds of MEMS sensors can be installed, such as temperature and chemical sensors, which can than be used for searching and recognition of objects or hazardous chemicals.

The power supply unit consists of three thin sheets of solar cells placed on a pyramidal configuration at the base of the MFI body (see Figure 3.1). The solar cells generates the power necessary for the wing actuators and the electronics of all the units. This sheet of solar cell can generate up to $20 mW cm^{-1}$ during a bright day. Underneath the solar cell, thin films of lithium batteries can store energy for dim-lit or night conditions of operation.

The communication unit, based on micro Corner Cube Reflectors (CCR) [89], a novel optoelectronic transmitter, or on ultra-low-power RF transmitters, provides a MFI with the possibility to communicate with a ground base or with others MFI's.

Finally, the control unit, embedded in the MFI computational circuitry, is responsible both

for stabilizing the flight and for planning the appropriate trajectory for each desired task.

3.2 Control Unit Architecture

The hierarchical architecture, partially inspired by real flying insects, as described above, and UAV research [39], decomposes the original global control problem into a multilevel set of simpler control problems. Moreover, thanks to this approach, the controllers on each level can be designed independently of those on higher levels, thus allowing the possibility to incrementally build more and more articulated control structures. Figure 3.3 shows the architecture proposed for the MFI control unit. It is possible to identify three main levels: the *trajectory planner*, the *flight mode stabilizer* and the *wing kinematics controllers*.
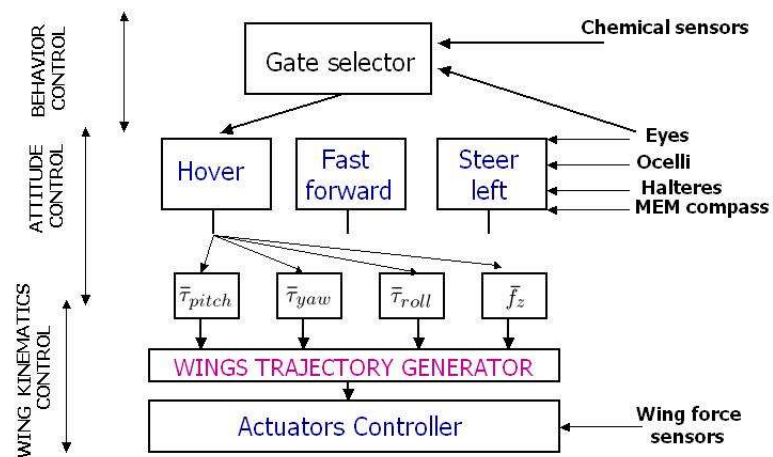
Figure 3.3: Design architecture for the control unit of the MFI.

This architecture is built in a top-down fashion, namely each level can interact with the lower level, but not vice versa. The top level is a voluntary since planning is determined by the MFI goals. The two lower levels are more reactive since the purpose of the attitude controller and the wing kinematic controller is to maintain the desired flight posture and the desired wing trajectory in the presence of external disturbances, respectively.

Different sensors influence each level of the the control unit. At the bottom level, force sensors at the wing base can estimate instantaneous wing position and thus improve wing trajectory

control. At the middle level halteres, ocelli and compass-like sensors can estimate insect orientation and velocity with a delay smaller then the wingbeat period. Large flow estimates from the compound eyes can provide redundant information about orientation and angular velocity. Although large-field optical flow estimates have lower bandwidth than ocelli and halteres, they have lower bias, and the fusion of all sensors information can therefore guarantee excellent performance.

At the top-level, the compound eyes provide the information necessary for guided navigation, mainly object avoidance and small-field object fixation. These sensors require a more sophisticated signal processing and therefore require a response time of a few wingbeats.

At the top level of the control unit there is the *trajectory planner*. Besides sensory input from the visual system, this unit receives commands from a communication link as well as information from application-specific sensors such as chemical or temperature sensors. The purpose of the top level control is to choose the appropriate flight modes, such as cruising, hovering or landing, to navigate the environment and achieve the desired task such as foraging, territory exploration, object tracking and more. Exploration and tracking algorithms, as well as object avoidance maneuvers, are implemented by the trajectory planner.

The middle level is the *flight mode stabilizer*. This level is responsible for stabilizing flight modes available to the MFI, namely *hovering, fast forward, power efficient forward, take off, landing, steering left, steering right, and moving up, down and sideways*. The number of different flight modes is arbitrary, but it should be rich enough to generate any desired trajectory or motion dictated by the trajectory planner. Each flight mode is provided with a controller that takes the input signals from halteres, ocelli, magnetic compass and large-field optical flow estimates. Based on this information, the controller chooses the appropriate values for the desired torques and forces that must be applied to MFI body to compensate for possible disturbances. The desired torques and forces are then passed to the bottom level, which maps them into the appropriate trajectory for the wings. Desired torques and forces are updated on the order of one or more wingbeats.

The bottom level is the *wing kinematics controller*. This level is responsible for generating the electrical signals for the actuators in order to generate motion of the wings corresponding to the desired torques and forces given by the flight mode stabilizer. The set of possible wing trajectories is parameterized according to some biokinematic elements. These parameters are chosen based on biomimetic principles, i.e. they can mimic most of the wing trajectories observed in real insects. These parameters are associated with important features of wing kinematics, such as the stroke angle amplitude and offset, timing of rotation, mean angle of attack and upstroke-to-downstroke wing speed ratio. Each set of desired torques and forces is mapped statically to a set of biokinematic

parameters, and thus to a wing trajectory that can generate these torques and forces as an average over a wingbeat period. Then, every wing trajectory is mapped to the corresponding actuator voltage via another static map. A detail description of this approach is given in Chapter 5. The wing kinematics controller receives input information from force sensors placed at the base of the wings. This input information can be directly used to estimate instantaneously the position and velocity of the wings, thus improving wing motion control through feedback, as proposed in [86].

Note how sensor bandwidths decrease from the bottom level to the top level. In fact, visual information, which is richer and more accurate since it estimates position as well as linear and angular velocity, is close to the top level since its processing requires more times than the sensors necessary to stabilize the insect flight.

3.3 Modeling

In this section, we describe the mathematical modeling used throughout this dissertation to design and evaluate controller designs.

3.3.1 Aerodynamics
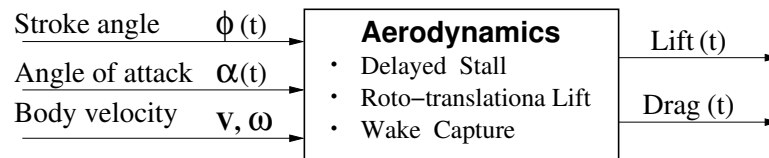
Figure 3.4: Block diagram of the Aeodynamical Module

Insect flight aerodynamics, which belongs to the regime of Reynolds's number between $30 - 1000$, has been a very active area of research in the past decades after the seminal work of Ellington [27]. Although, at present, some numerical simulations of unsteady insect flight aerodynamics based on the finite element solution of Navier-Stokes equations give accurate results for the estimated aerodynamics forces [59] [71], their implementation is unsuitable for control purposes since they require several hours of processing for simulating a single wingbeat, even on multiprocessor computers. However, several advances have been achieved in comprehending qualitatively and quantitatively unsteady-state aerodynamics mechanisms thanks to a scale model of flapping wing [24]. This apparatus, known as Robofly, consists of a two $25cm$-long wings system that mim-

ics the wing motion of flying insects. It is provided with force sensors at the wing base, which can measure instantaneous wing forces along a wingbeat.

Results obtained with this apparatus have identified 3 main aerodynamics mechanisms: *delayed stall*,*rotational lift* and *wake capture*, which have been described in Section 2.1 of Chapter 2.
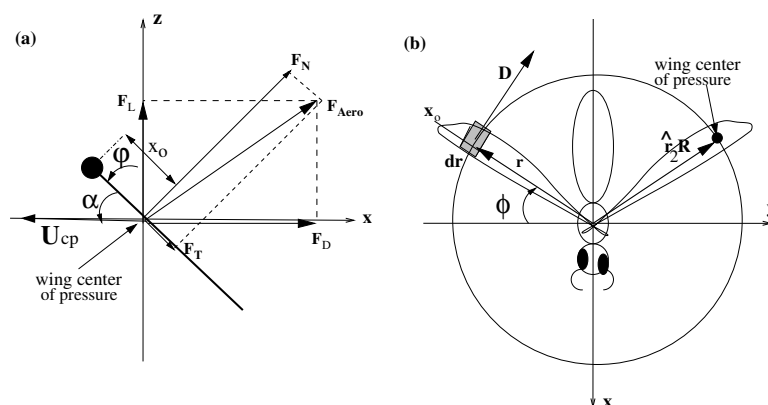
Figure 3.5: Force Decomposition for Horizontal Stroke Plane: (a) lateral view; (b) top view

The aerodynamic modeling described here is a combination of an analytical model, based on quasi-steady state equations for the delayed stall and rotational lift, and an empirically matched model based on Robofly data. Wake capture is very complex to treat analytically and it has not been considered in this work. However, this mechanism seems to have a small contribution for the sinusoidal-like motion of the wings, motion that it is widely used in simulations in this dissertation (see two bottom plots of Figure 3.7).
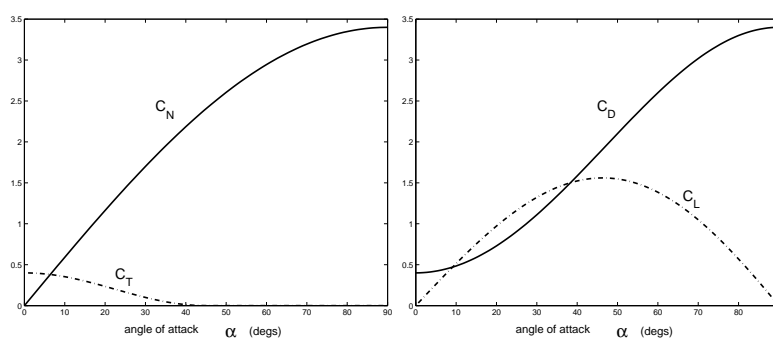
Figure 3.6: Aerodynamic force coefficients empirically obtained from RoboFly data.

A quasi-state state aerodynamic model assumes that force equations derived for 2D thin

aerofoils translating with constant velocity and constant angle of attack, hold also for time varying 3D flapping wings. In a steady state condition, the aerodynamic force per unit length exerted on a aerofoil due to delayed stall is given [42]:

$$
\begin{aligned}
F'_{tr,N} &= \frac{1}{2}C_N(\alpha)\rho c U^2 \\
F'_{tr,T} &= \frac{1}{2}C_T(\alpha)\rho c U^2
\end{aligned}
\tag{3.1}
$$

where $F'_{tr,N}$ and $F'_{tr,N}$ are, respectively, the normal and tangential components of the force with respect to the airfoil profile, c is the cord width of the aerofoil, ρ is the density of air, α is the angle of attack defined as the angle between the wing profile and the wing velocity relative to the fluid, U, and C_N and C_T are the dimensionless force coefficients. The orientation of these forces is always opposite to the wing velocity. Figure 3.5 shows a graphical representation of these forces. A good empirical approximation for the force coefficients is given by:

$$
\begin{aligned}
C_N(\alpha) &= 3.4\sin\alpha \\
C_T(\alpha) &= \begin{cases} 0.4\cos^2(2\alpha) & 0 \leq \alpha \leq 45^o \\ 0 & \text{otherwise} \end{cases}
\end{aligned}
\tag{3.2}
$$

as shown in [24] and [64]. In the aerodynamics literature, it is more common to find the lift and drag force coefficients, C_L and C_D. Lift, F_L and drag, F_D are defined, respectively, as the normal and tangential components of the total aerodynamic force, F_{aero}, with respect to the stroke plane, i.e. the plane of motion of the wings with respect to the body (see Figure 3.5a). However, the force decomposition in normal and tangential components is more intuitive, since aerodynamic forces are mainly pressure forces which act perpendicularly to the surface. Figure 3.6 shows the empirical values for the force coefficients obtained with RoboFly. These coefficients have been obtained from Equations (3.1) by measuring aerodynamic forces for different angles of attack and translational velocities. It is clear how, for high angles of attack, the tangential component, mainly due to skin friction, gives only a minor contribution. Nevertheless, lift and drag can be readily computed as:

$$
\begin{aligned}
C_L(\alpha) &= C_N\cos\alpha - C_T\sin\alpha \\
C_D(\alpha) &= C_N\sin\alpha + C_T\cos\alpha
\end{aligned}
\tag{3.3}
$$

Note how the maximum lift coefficient is achieved for angles of attack of approximately 45°, considerably different from fixed and rotary wings which produce maximum lift for angles of about 5°.

The aerodynamic force per unit length exerted on an aerofoil due to rotational lift is given by [33]:

$$F'_{rot,N} = \frac{1}{2}C_{rot}\rho\, c^2\, U\, \omega \tag{3.4}$$

where $C_{rot} = 2\pi\left(\frac{3}{4} - \hat{x}_o\right)$ is the rotational force coefficients, approximately independent of the angle of attack, x_o is the dimensionless distance of the rotation axis from the leading edge, and ω is the angular velocity of the wing with respects to that axis. In most flying insects x_o is about $\frac{1}{4}$, which corresponds to the theoretical value of the mean center of pressure along the wing chord direction. This is a pure pressure force and therefore acts perpendicularly to the wing profile, in the opposite direction of wing velocity.

According to the quasi-steady state approach, the total force on a wing is computed by dividing the wing into infinitesimal blades as shown in Figure 3.5. First, we calculate the total force on each blade:

$$
\begin{aligned}
dF_{tr,N}(t,r) &= \frac{1}{2}C_N(\alpha(t))\rho\, c(r)\, U^2(t,r)\, dr \\
dF_{tr,T}(t,r) &= \frac{1}{2}C_T(\alpha(t))\rho\, c(r)\, U^2(t,r)\, dr \\
dF_{rot,N}(t) &= \frac{1}{2}C_{rot}\rho\, c(r)^2\, U(t,r)\, \dot{\alpha}(t)\, dr \\
U(t,r) &= \dot{\phi}(t)r
\end{aligned}
\tag{3.5}
$$

where ϕ is the stroke angle and U_{body} is the velocity of the insect body w.r.t. an inertial system, and the wing angular velocity, ω is approximately $\dot{\alpha}$. Then we integrate the forces in Equations (3.5) along the wing, i.e. $F_{tr,N}(t) = \int_0^R dF_{tr,N}(t,r)$, to get:

$$
\begin{aligned}
F_{tr,N}(t) &= \frac{1}{2}\rho A_w C_N(\alpha(t))\, U^2_{cp}(t) & \tag{3.6}
\end{aligned}
$$

$$
\begin{aligned}
F_{tr,T}(t) &= \frac{1}{2}\rho A_w C_T(\alpha(t))\, U^2_{cp}(t) & \tag{3.7}
\end{aligned}
$$

$$
\begin{aligned}
F_{rot,N}(t) &= \frac{1}{2}\rho A_w C_{rot}\, \hat{c}\, c_{max}\, \dot{\alpha}(t)\, U_{cp}(t) & \tag{3.8}
\end{aligned}
$$

$$
\begin{aligned}
U_{cp}(t) &= \hat{r}_2 R\, \dot{\phi}(t) & \tag{3.9}
\end{aligned}
$$

where, A_w is the wing area, R is the wing length, U_{cp} is the velocity of the wing at the center of pressure, $\hat{r}_2$ is the normalized center of pressure, c_{max} is maximum wing chord width, and $\hat{c}$ is the normalized rotational chord. The former two parameters are defined as follows:

$$
\begin{aligned}
\hat{r}_2^2 &= \frac{\int_0^R c(r)\, r^2\, dr}{R^2 A_w} \\
\hat{c} &= \frac{\int_0^R c^2(r)\, r\, dr}{\hat{r}_2 R A_w c_{max}}
\end{aligned}
$$
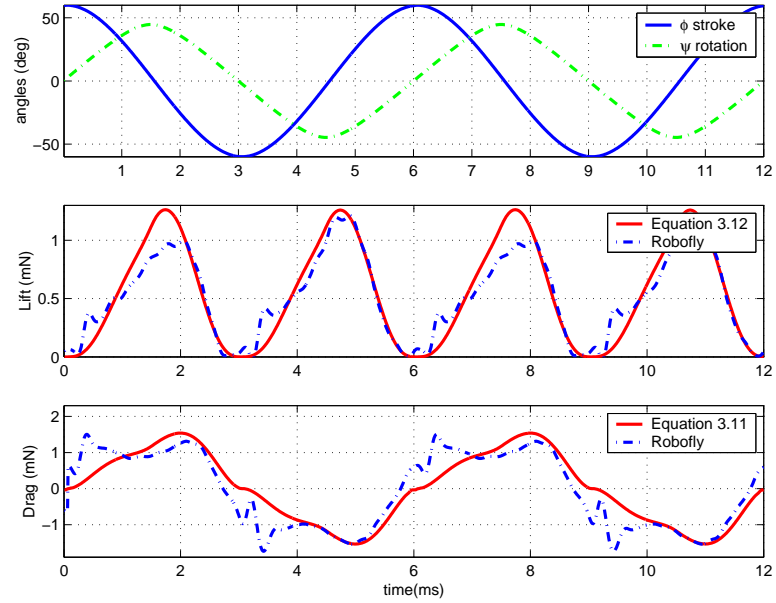
Figure 3.7: From top to bottom: stroke angle φ, rotation angle ψ, lift given by Equation (3.12) and drag given by Equation (3.11). These are traces corresponding to two wingbeat periods. In the last two plots, measured lift and drag forces obtained from Robofly data, a dynamically scaled model of insect wing, are also displayed (Robofly data are courtesy of M.H. Dickinson).

The normalized center of pressure, $\hat{r}_2$, and the normalized rotational chord, $\hat{c}$, depend only on the wing morphology, and in most of flying insects their range is approximately $\hat{r}_2 = 0.6 - 0.7$ and $\hat{c} = 0.5 - 0.75$ [27]. As a result of this approach, the wing forces can be assumed to be applied at a distance, $r_{cp} = r_2 R$, from the wing base. According to thin aerofoil theory, the center of pressure r_{cp} lies about $\frac{1}{4}$ of chord length from the leading edge. This has been confirmed by numerical simulations of insect flight which do not assume a quasi-steady state aerodynamic regime [59], and by experiments performed by scaled model of wings [64].

If the velocity of the insect body is comparable with the mean wing velocity of the center of pressure, as during cruising flight mode, a more accurate model for estimating the aerodynamic forces is based on finding the absolute velocity of the center of pressure of the wing relative to an inertial frame, which is obtained by substituting Equation (3.9) with the following:

$$U_{cp}(t) = \hat{r}_2 R \dot{\phi}(t) + v^b(t) \tag{3.10}$$

where $v^b(t)$ is the velocity of the insect body relative to the inertial frame represented in the wing frame coordinate system.

The total lift and drag forces acting on the wing can be derived through a trigonometric

transformation analogous to the one used in Equations (3.3) as follows:

$$
\begin{aligned}
F_N(t) &= F_{tr,N}(t) + F_{rot,N}(t) \\
F_T(t) &= F_{tr,T}(t) \\
F_D(t) &= F_N(t)\cos\alpha(t) - F_T(t)\sin\alpha(t) \quad\quad\quad (3.11)\\
F_L(t) &= F_N(t)\sin\alpha(t) + F_T(t)\cos\alpha(t) \quad\quad\quad (3.12)
\end{aligned}
$$

where $F_{tr,N}, F_{tr,T}, F_{rot,N}$ are given in Equations (3.6)-(3.7)-(3.8), respectively, and $U_{cp}(t)$ is given in Equation (3.10).

The total aerodynamic forces used for simulations throughout this dissertation are based on Equations (3.11)-(3.12). Figure 3.7 shows the simulated aerodynamic forces for a typical wing motion and the corresponding experimental data obtained with a dynamically scaled model of insect wing (Robofly traces).

3.3.2   Body Dynamics
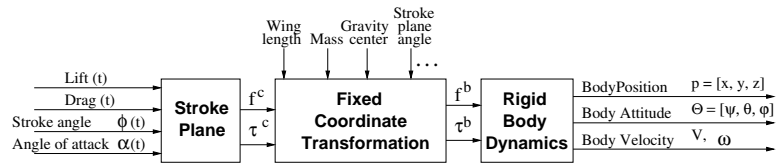
Figure 3.8: Body Dynamics Block Diagram

The body dynamics equations compute the evolution of the dynamics of the insect center of mass and insect orientation with respect to an inertial frame. This evolution is the result of the wings' inertial forces, and the external forces, specifically aerodynamic forces, body damping forces and the force of gravity. However, the mass of the wings is a small percentage of the insect's body mass and as they move almost symmetrically, their effect on insect body dynamics is likely to cancel out within a single wingbeat. In fact, even if wing inertial forces are larger than aerodynamic forces, nonholonomic rotations would be possible for frictionless robots with moving links (see [52] Example 7.2) only if the links, in our case the wings, would flap out of sync with each other, an activity not observed in real insects. Thus, based on this observation, it seems safe to assume that one can disregard inertial forces and simplify the evolution of insect dynamics to a single rigid body under the effects of external forces. Nonetheless, a more detailed analysis to validate this assumption would be beneficial.

As shown in [52], the equations for rigid body motion are subject to an external wrench $F^b = [f^b, \tau^b]^T$ applied at the center of mass and specified with respect to the body coordinate frame. These are given as:

$$\begin{bmatrix} m\mathrm{I} & 0 \\ 0 & I \end{bmatrix} \begin{bmatrix} \dot{v}^b \\ \dot{\omega}^b \end{bmatrix} + \begin{bmatrix} \omega^b \times mv^b \\ \omega^b \times I\omega^b \end{bmatrix} = \begin{bmatrix} f^b \\ \tau^b \end{bmatrix} \tag{3.13}$$

where m is the mass of the insect, I is the insect body inertia matrix relative to the center of mass, v^b is the velocity vector of the center of mass in body frame coordinates, and ω^b is the angular velocity vector in the body frame. The values for the body and wing morphological parameters, such as length and mass, used for the simulations in this dissertation are those of a typical blowfly.

The total force and torque vectors in the body frame are given by the sum of the three external forces, i.e. the aerodynamic forces, f_a^b, the body damping forces, f_d^b, and the gravity forces, f_g^b:

$$\begin{aligned} f^b &= f_a^b + f_g^b + f_d^b \\ \tau^b &= \tau_a^b + \tau_g^b + \tau_d^b \end{aligned} \tag{3.14}$$

The aerodynamic forces and torques relative to the insect center of mass, can be obtained by a sequence of fixed coordinate transformations, starting from lift and drag forces and wings kinematics calculated by the aerodynamic module as follows:

$$\begin{aligned} f_a^b(t) &= f_a^l(t) + f_a^r(t) \\ \tau_a^b(t) &= p_l(t) \times f_a^l(t) + p_r(t) \times f_a^r(t) \end{aligned} \tag{3.15}$$

where the subscripts l, r stand for left and right wing, respectively, and $p(t)$ is the position of the center of pressure of the wing relative to the center of mass.

Since the lift and drag forces are calculated relative to the *stroke plane frame*, a coordinate transformation is necessary before obtaining the forces and torques acting on the *body frame*. To this purpose, three coordinate systems and their corresponding parameters need to be defined.
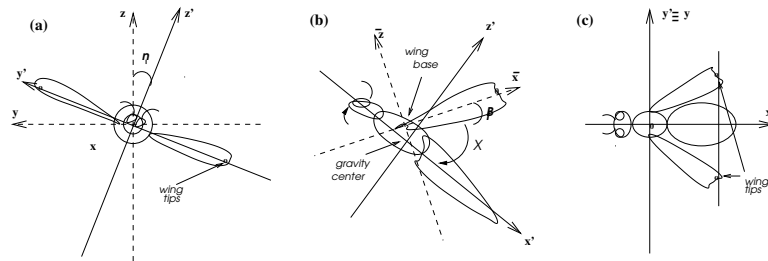
Figure 3.9: Coordinate Systems: (a) Front View; (b) Lateral View; (c) Top View

As seen from Figure 3.9, the *fixed (inertial) frame* is identified by the axis (x, y, z). The *insect body frame* is described by the coordinate system (x', y', z') attached to the body center of gravity and with x-axis oriented from tail to head, the y-axis from right wing hinge to left wing hinge, and the z-axis from ventral to dorsal side of the abdomen. Since these are the axes of symmetry of the insect, the matrix of inertia is diagonal in the body frame. The *stroke plane frame* is identified by the new axis $(\bar{x}, \bar{y}, \bar{z})$, and is attached to the wing base. The *stroke plane frame* is defined as the plane to which the wing motion is approximately confined during flapping flight.

Given the lift and drag generated by aerodynamics, together with the stroke angle, the forces and torques in *stroke plane* can be calculated as

$$
f_a^c = \begin{bmatrix} -F_D^l \cos\phi_l - F_D^r \cos\phi_r \\ F_D^l \sin\phi_l - F_D^r \sin\phi_r \\ F_L^l + F_L^r \end{bmatrix} \tag{3.16}
$$

$$
\tau_a^c = \hat{r}_2 R \begin{bmatrix} F_L^l \cos\phi_l - F_L^r \cos\phi_r \\ -F_D^l \sin\phi_l - F_D^r \sin\phi_r \\ F_D^l - F_D^r \end{bmatrix} \tag{3.17}
$$

where we used $\mathbf{p}_l^w(t) = \hat{r}_2 R(\sin\phi_l, \cos\phi_l, 0)$ and $\mathbf{p}_r^w(t) = \hat{r}_2 R(\sin\phi_r, -\cos\phi_r, 0)$. To obtain the aerodynamics forces and torques in the *body frame*, we do a coordinate transformation as:

$$
\begin{bmatrix} f_a^b \\ \tau_a^b \end{bmatrix} = \begin{bmatrix} R_{cb}^T & 0 \\ -R_{cb}^T \hat{p}_{cb} & R_{cb}^T \end{bmatrix} \begin{bmatrix} f_a^c \\ \tau_a^c \end{bmatrix}
$$

where R_{cb} is the rotation matrix of the body frame relative to the stroke plane, and p_{cb} represents the translation of the origin of the body frame from the stroke plane. This is a fixed transformation that depends only on the morphology of the insect or MFI.

The gravitational forces and torques in the *body frame*, are given by:

$$
\begin{bmatrix} f_g^b \\ \tau_g^b \end{bmatrix} = \begin{bmatrix} R^T \begin{bmatrix} 0 \\ 0 \\ mg \end{bmatrix} \\ 0 \end{bmatrix}
$$

where R is the rotational matrix of the body frame relative to the spatial frame, and g is the gravitational acceleration.

The viscous damping exerted by the air on the insect body are approximately given by:

$$\begin{bmatrix} f_d^b \\ \tau_d^b \end{bmatrix} = \begin{bmatrix} -b\,v^b \\ 0 \end{bmatrix}$$

where b is the viscous damping coefficient. The reason for the linearity in the velocity of the drag force is that the velocity of the insect is small relative to insect size, therefore viscous damping prevails over quadratic inertial drag. Empirical evidence for a linear damping has been recently observed by the author by analyzing the free flight dynamics of fruit flies. Analytical estimation and experimental data of rotational damping of insects show that the resulting torques are negligible relative to aerodynamic forces even during rapid body rotation and can therefore be neglected. Thus, it can be concluded that insect body attitude dynamics behaves like an underdamped system [31].

A block diagram representation of insect dynamics is shown in Figure 3.8.

Numerical solutions of Equations (3.13) have been implemented using Euler's angle representation for the rotation matrix. In particular, we consider the new variables $\dot{P} = v^p = Rv^b$ and $\hat{\omega}^b = R^T\dot{R}$.

For $R \in SO(3)$, we parametrize R by *ZYX* Euler's angles with φ, θ, and ψ about *x,y,z* axes respectively, and hence $R = e^{\hat{z}\psi}e^{\hat{y}\theta}e^{\hat{x}\varphi}$ with $x = [1\ 0\ 0]^T$, $y = [1\ 0\ 0]^T$, $z = [0\ 0\ 1]^T$ and $\hat{x}, \hat{y}, \hat{z} \in so(3)$. By differentiating R with respect to time, we have the state equations of the Euler angles, $\Theta = [\varphi\ \theta\ \psi]^T$, which can be defined as $\dot{\Theta} = W\omega^b$. By defining the state vector $[P, \Theta] \in R^3 \times R^3$ where P is the position of the center of mass with respect to the inertial frame, and Θ are the euler angles which we use to parametrize the rotation matrix R, we can rewrite the equations of motion of a rigid body as:

$$\begin{aligned} \ddot{\Theta} &= (IW)^{-1}[\tau^b - W\dot{\Theta} \times IW\dot{\Theta} - I\dot{W}\dot{\Theta}] \\ \ddot{P} &= \frac{1}{m}Rf^b \end{aligned}$$
(3.18)

where the body forces and torques are time-varying, nonlinear functions of the wing kinematics as

$$\begin{aligned} f^b &= f^b(\phi_i(t), \dot{\phi}_i(t), \alpha_i(t), \dot{\alpha}_i(t)) \\ \tau^b &= \tau^b(\phi_i(t), \dot{\phi}_i(t), \alpha_i(t), \dot{\alpha}_i(t)) \end{aligned}$$
(3.19)

where $i \in \{l, r\}$ represents the left and right wing, respectively.

3.3.3 Actuators Dynamics

Each wing is moved by the thorax, a complex trapezoidal structure actuated by two piezo-electric actuators at its base, as shown in Figure 3.10. A complete nonlinear model for the thorax,
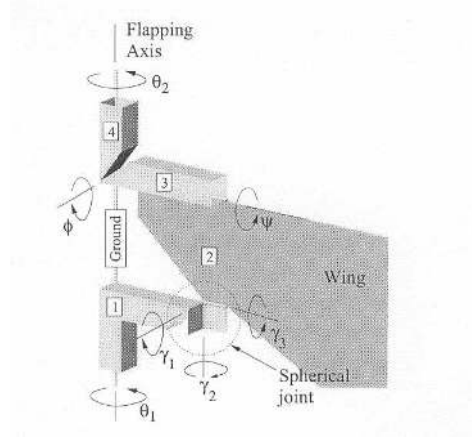
Figure 3.10: Wing-Thorax structure. Courtesy of [4].

developed in [4], can be written as follows

$$M \begin{bmatrix} \ddot{\theta}_2 \\ \ddot{\alpha} \end{bmatrix} + B \begin{bmatrix} \dot{\theta}_2 \\ \dot{\alpha} \end{bmatrix} + K \begin{bmatrix} \theta_2 \\ \alpha \end{bmatrix} + \begin{bmatrix} 0 \\ f(\dot{\alpha}) \end{bmatrix} = T \begin{bmatrix} u_1 \\ u_2 \end{bmatrix} \qquad (3.20)$$

where $f(\dot{\alpha}) = \frac{1}{2}m'_{\omega,2}(\dot{\alpha})^2$, θ_2 is the leading edge flapping angle from the four bar mechanism, $\alpha = \theta_1 - \theta_2$ is the phase difference between the four bar output angles, u_1 and u_2 are the control input torques to the actuators, M and B are the inertia and damping matrices and are assumed to be constant. However, parameters in K and T matrices include some slow time variable terms, and the control inputs (u_1, u_2) are limited to $10\mu Nm$ by physical constraints.

The relationship between the state variables in Equation (3.20) and the wing motion variables (stroke angle ϕ, rotation angle φ, see Figure 3.5) can be approximated as $\phi = \theta_2$ and $\varphi = 2\alpha$. Based on Equation (3.20), with a change of variables, neglecting the nonlinear components, we can derive the linear actuator model as

$$M_0 \begin{bmatrix} \ddot{\phi} \\ \ddot{\varphi} \end{bmatrix} + B_0 \begin{bmatrix} \dot{\phi} \\ \dot{\varphi} \end{bmatrix} + K_0 \begin{bmatrix} \phi \\ \varphi \end{bmatrix} = T_0 \begin{bmatrix} u_1 \\ u_2 \end{bmatrix} \qquad (3.21)$$

where M_0, B_0, K_0, and T_0 are constant matrices calculated from the data provided in [4].

Equation (3.21) is a stable linear MIMO system and can also be written using a transfer function representation in the frequency domain:

$$Y(j\omega) = G(j\omega)U(j\omega)$$

where Y, U are the Fourier transformations of the output vector $y = (\phi, \varphi)$, and the input vector $u = (u_1, u_2)$, respectively. The electromechanical structure has been designed so that the input-output frequency response of the system is almost decoupled at all frequencies, i.e. $|G_{11}(j\omega)| \simeq |G_{22}(j\omega)| \gg |G_{12}(j\omega)| \simeq |G_{21}(j\omega)|, \forall \omega$, where G_{ik} represents the $i - k$ entry of the matrix G, and $\omega = 2\pi f$. Moreover, the system has also been designed to achieve a quality factor $Q = 3$ at the desired resonant frequency of $f_0 = 150Hz$, i.e. $|G_{ii}(j2\pi f_0)| \simeq Q|G_{ii}(0)|$. A low quality factor Q is necessary to easily control the wing trajectory even when the wingbeat frequency is the same as the resonant frequency. In fact, large Qs would practically remove all higher order harmonics from the input signals and the wing would simply oscillate along the same sinusoidal trajectory. A more detailed exploration about these tradeoffs is considered in Example 4.2.2 in the next Chapter.

The model presented in this paragraph along with additional details can be found in [3] and [4].

3.4 Conclusions

In this chapter we gave a brief overview of both the purpose and the challanges facing the fabrication of MFIs. Taking our cues from real insects, we propose a hierarchical architecture that divides the control unit into three main levels: the lowest level is designed to track a desired wing trajectory, the middle level is designed to stabilize flight modes in the event of external disturbances and the top level is designed to allow the insect to navigate in varying environments. The hierarchical structure is meant to simplify the controller design process and to optimally blend both a reactive control system that is necessary to compensate for external disturbances and a voluntary control system necessary to navigate in the environment that would otherwise would conflict with each other. Different sensors provide the necessary information for each level: at the low level, force sensors are located at the wing base and are used for fine tuning of trajectory tracking; at the middle level ocelli and halteres to estimate quickly orientation and angular velocities necessary to compensate for external disturbances; and at the top level are compound eyes used for fine orientation estimation, object avoidance and object tracking.

We also gave a mathematical model for two of the three aerodynamic mechanisms described in the previous chapter: the delayed stall and the rotational lift. These are solely functions of the instantaneous position and velocity of insect wings. These models will be used in simulations of insect flight in Chapter 5. A simple model for the wake capture is currently unavailable outside of the numerical solutions of hydrodynamic equations, which can be performed only on su-

percomputers. However, comparisons between simulations of our model with the experimental data obtained from dynamically scaled wings show only small differences. Although these differences are certainly non-negligible, they are unlikely to change the qualitative results obtained in Chapter 5.

The dynamics of the insect body is modeled on the dynamics of a rigid body subject only to external forces: the gravity force, the wing aerodynamic forces, and the body viscous drag. Although the inertial forces generated by the two wings are comparable in magnitude with aerodynamic forces, they are unlikely to give rise to a change in the overall dynamics of the insect body via non-holonomic effects as the wings move almost symmetrically and the inertial forces approximately cancel each other. Nonetheless, a rigorous validation of this argument should be considered and it is left as future work.

Finally, a model of the MFI wing-thorax dynamics is included to give a more realistic approximation of the insect dynamics. Electromechanical parameters of this structure, such as the resonant frequency and quality factor, have been designed following biomimetic principles. In Chapter 6, we will show how the particular choice of these parameters might be linked to a trade-off between the aerodynamic efficiency and the responsiveness of body dynamics.

Chapter 4

Averaging theory for high-frequency non-affine control systems

Averaging theory has become an important tool in analyzing underactuated systems driven by high frequency signals [13]. The reason for this is that in underactuated systems not all degrees of freedom can be controlled directly and independently, since the number of inputs is smaller then the number of degrees of freedom. However, in nonholonomic systems [73] [44], in particular in controlled systems nonlinear in the inputs [11], it is possible to *approximately* control a number of degrees of freedom that is larger than the number of input channels by appropriately exciting the system with high-frequency input signals.

Averaging theory serves to quantify this approximation in terms of the dynamics of the averaged system. Informally speaking, high-frequency control means that the period of the oscillating signal is much smaller than the time necessary for the system to change substantially. This is a vague definition, but it is unavoidable since it is not possible to give a formal definition of bandwidth for a generic nonlinear system. The reason for high-frequency control lies in the fact that the system dynamics is much slower than the frequency of the signals. Thus, only mean signals determine the evolution of the systems. A simple example is a light bulb. The light is generated by an oscillating AC current at $60Hz$. However the light intensity seems to be constant because the incandescent wire inside the bulb cannot turn on and off as fast as the current and our eyes cannot capture changes in environment that are faster than $25Hz$. In fact, if one could measure accurately light intensity with an oscilloscope, one would notice that the signal oscillates around a mean value with a frequency of $60Hz$ and an amplitude that is much smaller than the mean value.

The purpose of this chapter is to give a rigorous understanding at a similar phenomenon, and in particular high-frequency control for a class of underactuated control systems, based on averaging theory. Particular attention is placed on giving an intuitive understanding of theorems, in order to facilitate readers unfamiliar with averaging theory. Averaging theory and its applications for control are vast, but a comprehensive theory is not yet available. Several results are available for driftless affine systems, i.e. systems of the form $\dot{x} = f(x) + \sum_{i=1}^{m} g_i(x)u_i$ where $u_i \in \mathbb{R}$ and $f(x) \equiv 0$, as shown in [72] [53] [44]. Recently, there has been considerable effort to extend some of these results to affine systems with drift, i.e. systems for which $f(x) \neq 0$. These systems are much more difficult to study in general terms and advances have been obtained only when systems possess an underlying geometric structure as shown in [13] [46] [80]. Finally, averaging theory and control have been applied to aquatic [79] [50] and anguilliform locomotion [58]. Averaging and nonholonomic control theories deserve a longer discussion which is not within the scope of this dissertation. The goal of this dissertation, and this chapter in particular, is to show that the averaging theory is an intuitive approach to the analysis of dynamical systems, even though the tools necessary are quite sophisticated. Flapping flight will be analyzed only using the tools developed in this chapter.

This chapter is structured as follows: Section 4.1 gives a simple example to introduce high-frequency systems and averaging theory. Section 4.2 introduces the fundamental theorem of first order averaging and extends it to controlled systems. Section 4.3 shows how averaging theory can be applied to underactuated non-affine control systems, and in particular how the approximating systems can have a larger number of virtual independent control inputs. Finally, Section 4.4 extends the previous theorems to systems in which actuators dynamics is included and shows the limiting tradeoff between performance and efficiency.

4.1   A motivating example

Intuitively, everybody knows that in a low-pass linear system driven by a periodic input only the mean value appears at the output, while the zero-mean component of the periodic input is filtered out if the frequency is much larger than the bandwidth of the system. In fact, let us consider the linear system

$$\dot{x} = f(x,t) = -x + A\sin(\frac{2\pi}{T}t) \quad \text{for } t \geq 0 \tag{4.1}$$

whose explicit solution can be found in any linear systems theory textbook and is given by:

$$x(t) = e^{-t}x_0 + \frac{T}{2\pi\sqrt{1+\frac{T^2}{4\pi^2}}} A\sin(\frac{2\pi}{T}t + \phi)$$

where $\phi = \tan^{-1}(\frac{2\pi}{T})$. Let us now consider the averaged vector field defined as follows:

$$\bar{f}(x) \triangleq \frac{1}{T}\int_0^T f(x,t)dt$$

and the evolution of the associated averaged system:

$$\dot{\bar{x}} = \bar{f}(\bar{x},t) = -\bar{x} \tag{4.2}$$

whose solution is given by

$$\bar{x}(t) = e^{-t}x_0.$$

If we compare the solution of the two systems we notice a few facts. The first fact is that the evolution of the averaged system (4.2) approximates the evolution of the exact system (4.1), since we have

$$|x(t) - \bar{x}(t)| = \left|\frac{T}{2\pi\sqrt{1+\frac{T^2}{4\pi^2}}} A\sin(\frac{2\pi}{T}t + \phi)\right| \leq \frac{A}{2\pi}T$$

and the approximation becomes more accurate as the period of the forcing signal decreases.

The second fact is that the solution of the original system (4.1) converges exponentially to a T-periodic limit cycle $x_T(t)$ from any initial condition:

$$x_T(t) \triangleq \frac{T}{2\pi\sqrt{1+\frac{T^2}{4\pi^2}}} A\sin(\frac{2\pi}{T}t + \phi)$$

$$\lim_{t\to+\infty} |x(t) - x_T(t)| = \lim_{t\to+\infty} |x_0|e^{-t} = 0.$$

Moreover, the magnitude of the periodic solution $x_T(t)$ decreases linearly with the period of the forcing:

$$|x_T(t)| \leq \frac{A}{2\pi}T$$

The third fact is that the origin of the system (4.1) is not an equilibrium point, i.e. $f(0,t) \neq 0$, but the origin of the averaged system (4.2) is exponentially stable.

These three facts are quite natural for linear systems driven by a periodic signal, but fortunately they hold also for general nonlinear periodic non-autonomous systems $\dot{x} = f(x,t)$ under some technical conditions.

Before continuing, we need to show how high-frequency systems are related to averaging theory. In particular, we are interested in studying the evolution of a system when the frequency is increased. To this purpose, let us consider the general nonlinear system:

$$\dot{x} = f(x,t) \tag{4.3}$$

where $f(x,t)$ is T-periodic in its second argument, i.e. $f(x,t+T) = f(x,t)$. The following change of timescale $t = T\tau$, which is equivalent to normalizing the dynamics of the system to the period of the oscillating vector field $f(x,t)$, gives the following system:

$$\frac{dx}{d\tau} = Tf(x,T\tau) = T\tilde{f}(x,\tau) \tag{4.4}$$

where the vector field $\tilde{f}(x,\tau)$ is 1-periodic in its second argument. If $x(\tau)$ is the solution of the system (4.4), then the solution of the system (4.4) with the same initial condition is simply $x(\frac{t}{T})$. Since we assume that T is a "small" parameter, high-frequency system belong to the more general system considered in averaging theory:

$$\dot{x} = \varepsilon f(t,x,\varepsilon) \tag{4.5}$$

where $f(t,x,\varepsilon)$ is T-periodic in t. It is important to note that the high frequency system of Equation (4.4) looks like the system commonly presented in standard averaging theory given by Equation (4.5) when the following points are taken into account: (1) the period T in system (4.4) plays the role of ε in system (4.5), (2) the period T system (4.5) is explicitly set to unity and (3) there is no dependence on ε in the vector field $f(x,t,\varepsilon)$ of the system (4.5), (i.e. $f(x,t,\varepsilon) = f(x,t)$).

The next section gives the main theorem of averaging theory and its application to high-frequency systems.

4.2   First Order Averaging Theory

Theorem 4.2.1. Theorem of Averaging [37]

Let $f(x,y,\varepsilon)$ and its partial derivatives with respect to (x,ε) up to the second order be continuous and bounded for $(t,x,\varepsilon) \in [0,\infty) \times D_0 \times [0,\varepsilon_0]$, for every compact set $D_0 \subset D$, where $D \in \mathbb{R}^n$ is a domain. Suppose f is T-periodic in t for some $T > 0$, and ε is a positive parameter. Let $x(t,\varepsilon)$ and $\bar{x}(\varepsilon t)$ be the solution of the systems:

$$\dot{x} = \varepsilon f(x,t,\varepsilon) \tag{4.6}$$

$$\dot{\bar{x}} = \varepsilon \bar{f}(\bar{x},\varepsilon) \tag{4.7}$$

respectively, where $\bar{f}(x) \overset{\Delta}{=} \frac{1}{T} \int_0^T f(x,t,0)dt$.

- *If $\bar{x}(\varepsilon t) \in D \;\; \forall t \in [0, \frac{b}{\varepsilon}]$ and $x(0,\varepsilon) - \bar{x}(0) = O(\varepsilon)$, then there exists $\varepsilon^* > 0$ such that for all $0 < \varepsilon < \varepsilon^*$, $x(t,\varepsilon)$ is defined and*

$$x(t,\varepsilon) - \bar{x}(\varepsilon t) = O(\varepsilon) \;\; on \;\; [0, \frac{b}{\varepsilon}]$$

- *If the origin $x = 0 \in D$ is an exponentially stable equilibrium point of the averaged system (4.7), $\Omega \subset D$ is a compact subset of its region of attraction, $\bar{x}(0) \in \omega$, and $x(0,\varepsilon) - \bar{x}(0) = O(\varepsilon)$, then there exists $\varepsilon^* > 0$ such that for all $0 < \varepsilon < \varepsilon^*$, $x(t,\varepsilon)$ is defined and*

$$x(t,\varepsilon) - \bar{x}(\varepsilon t) = O(\varepsilon) \;\; on \;\; [0,\infty)$$

- *If the origin $x = 0 \in D$ is an exponentially stable equilibrium point of the averaged system (4.7), then there exist positive constants ε^* and k such that, for all $0 < \varepsilon < \varepsilon^*$, the system (4.6) has a unique, locally exponentially stable, T-periodic solution $x_T(t,\varepsilon)$ with the property $||x_T(t,\varepsilon)|| \le k\varepsilon$.*

- *If the origin $x = 0 \in D$ is an exponentially stable equilibrium point of the averaged system (4.7), and also an equilibrium point of the system (4.6), i.e. $f(0,t,\varepsilon) = 0 \;\; \forall(t,\varepsilon)$, then the origin is exponentially stable equilibrium point for the system (4.6)*

Proof. Here we give only a sketch of the proof that can be found in Theorem 10.4 in Khalil's book [37], which shows that there exists a change of variables which rewrites the system (4.6) as the averaged vector field plus a periodic perturbation whose magnitude decreases linearly with the parameter ε. The change of variable is the following:

$$x = y + \varepsilon u(t,y) \tag{4.8}$$

where the function $u(t,y)$ is defined as follows:

$$u(t,y) = \int_0^t \left(f(t,y,0) - \bar{f}(y) \right) d\tau$$

By construction, the function $u(t,y)$ is T-periodic in t and differentially continuous up to second order in its arguments. Differentiating both sides with respect to t, and after some algebraic manipulations the differential equation for variable y is given by:

$$\dot{y} = \varepsilon \bar{f}(y) + \varepsilon^2 q(t,y,\varepsilon)$$

where the function $q(t,y,\varepsilon)$ is T-periodic in t, and $\bar{f}(y)$, $q(t,y,\varepsilon)$, and their first partial derivatives with respect to (y,ε) are continuous and bounded on $[0,\infty) \times D_0$ for sufficiently small ε. All the statements in the theorem hold for the trajectories $y(t)$, as they directly follow from perturbation theory (see Chapter 9-10 in [37]). By substituting the solution $y(t)$ into Equation (4.8), all the statements can be proven true for the variable x, also. $\qquad\square$

High-frequency systems can be reframed within the averaging theory setup as shown in the following lemma:

Lemma 4.2.1. *Let $f(x, \frac{t}{T})$ and its partial derivatives with respect to (x,t) up to the second order be continuous and bounded for $(t,x) \in [0,\infty) \times D_0$, for every compact set $D_0 \subset D$, where $D \in \mathbb{R}^n$ is a domain. Suppose $f(x,\tau)$ is 1-periodic in τ. Let $x(t,T)$ and $\bar{x}(t)$ be the solution of the systems:*

$$\dot{x} = f(x, \frac{t}{T}) \tag{4.9}$$

$$\dot{\bar{x}} = \bar{f}(\bar{x}) \tag{4.10}$$

respectively, where $\bar{f}(x) \overset{\Delta}{=} \frac{1}{T}\int_0^T f(x, \frac{t}{T})dt = \int_0^1 f(x,\tau)d\tau$.

- *If $\bar{x}(t) \in D \ \forall t \in [0,b]$ and $x(0,T) - \bar{x}(0) = O(\varepsilon)$, then there exists $T^* > 0$ such that for all $0 < T < T^*$, $x(t,T)$ is defined and*

$$x(t,T) - \bar{x}(t) = O(1) \ \text{ on } \ [0,b]$$

- *If the origin $x = 0 \in D$ is an exponentially stable equilibrium point of the averaged system (4.10), $\Omega \subset D$ is a compact subset of its region of attraction, $\bar{x}(0) \in \omega$, and $x(0,T) - \bar{x}(0) = O(T)$, then there exists $T^* > 0$ such that for all $0 < T < T^*$, $x(t,T)$ is defined and*

$$x(t,T) - \bar{x}(t) = O(T) \ \text{ on } \ [0,\infty)$$

- *If the origin $x = 0 \in D$ is an exponentially stable equilibrium point of the averaged system (4.10), then there exist positive constants T^* and k such that, for all $0 < T < T^*$, the system (4.9) has a unique, locally exponentially stable, T-periodic solution $x_T(t)$ with the property $\|x_T(t)\| \le kT$.*

- *If the origin $x = 0 \in D$ is an exponentially stable equilibrium point of the averaged system (4.10), and also an equilibrium point of the system (4.9), i.e. $f(0,t) = 0 \ \forall t$, then the origin is exponentially stable equilibrium point for the system (4.9)*

Proof. The proof follows directly from Theorem 4.2.1 after the change of timescale $\tau = \frac{t}{T}$. □

This theorem states that if the frequency $f = \frac{1}{T}$ of the vector field is sufficiently high, then the trajectory of the time-varying system (4.9) is approximated by the averaged system (4.10) and the approximation improves as the frequency increases. Moreover, if the averaged system has an exponentially stable equilibrium point, then the original system converges exponentially to a periodic limit cycle, whose magnitude decreases as the frequency increases. In some practical applications the magnitude of this limit cycle can be extremely small to the extent that it is undistinguished from the origin. This is the case of the light bulb mentioned at the beginning of this chapter: to human eyes, powering a light bulb with a DC (continuous) current is undistinguishable from powering a light bulb with a high frequency AC (periodic) current which gives the same mean power. The next example shows an application of the previous lemma to a simple system:

Example 4.2.1.
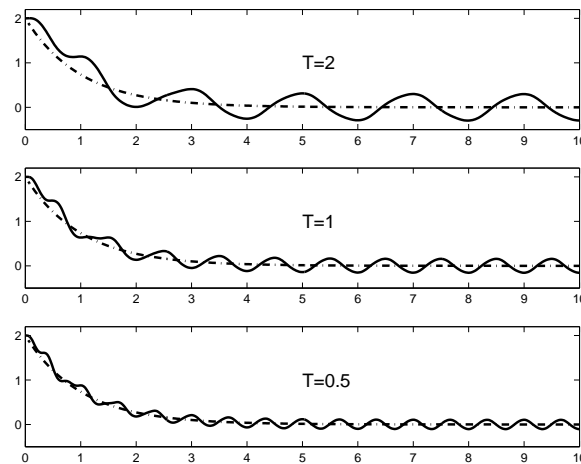
Figure 4.1: The exact (solid) and averaged (dash-dot) solutions of Example 4.2.1

Consider the following dynamical system:

$$\dot{x} = f(x, \frac{t}{T}) = -2x\sin^2(\frac{t}{T}) + \sin(\frac{t}{T})$$

and the corresponding averaged system as defined in Lemma 4.2.1:

$$\dot{\bar{x}} = \bar{f}(\bar{x}) = -\bar{x}$$

The averaged system is exponentially stable and the averaged solution is simply $\bar{x}(t) = e^{-t}x_0$. Figure 4.1 clearly illustrates how the solution of the averaged system averages the exact solution and how the exact solution converges to a periodic limit cycle. Also, the figure shows how the averaged solution becomes closer to the exact solution as the frequency increases, and the magnitude of the limit cycle decreases.

4.3 Averaging for non-affine control systems

In this section we extend the theorem developed in the previous section to controlled systems.

Theorem 4.3.1. *Let us consider the controlled system:*

$$\dot{x} = f(x, u) \tag{4.11}$$

where $f(x, u)$ and its partial derivatives with respect to (x, u) up to the second order are continuous, where $x \in \mathbb{R}^n$ and $u \in \mathbb{R}^m$. Let us consider the periodic open-loop control

$$u = g(v, \frac{t}{T}) \tag{4.12}$$

where $g(v, \tau)$ is 1-periodic in τ, and is continuously differentiable up to the second order, where $v \in \mathbb{R}^p$. Consider the new periodic controlled system:

$$\dot{x} = f_g(x, v, \frac{t}{T}) \triangleq f(x, g(v, \frac{t}{T})) \tag{4.13}$$

and the averaged system

$$\dot{\bar{x}} = \bar{f}_g(x, v) \triangleq \int_0^1 f(x, g(v, \tau)) d\tau \tag{4.14}$$

Finally, consider the feedback control:

$$v = h(x) \tag{4.15}$$

where h and its derivatives up to second order are continuous. If the origin $x = 0$ is an exponentially stable equilibrium point of the averaged system $\dot{\bar{x}} = \bar{f}_{gh}(x) \triangleq \bar{f}_g(x, h(x))$, $\Omega \subset D$ is a compact subset of its region of attraction, $\bar{x}(0) \in \Omega$, and $x(0, T) - \bar{x}(0) = O(T)$, where $x(t, T)$ is the solution of the system given by Equations (4.13) and (4.15), then there exists $T^* > 0$ such that for all $0 < T < T^*$, $x(t, T)$ is defined and

$$x(t, T) - \bar{x}(t) = O(T) \ \ on \ \ [0, \infty)$$

Moreover, there exists a positive constant k such that, for all $0 < T < T^*$, the system given by Equations (4.13) and (4.15) has a unique, locally exponentially stable, T-periodic solution $x_T(t)$ with the property $||x_T(t)|| \leq kT$.

Proof. The proof follows directly from Lemma 4.2.1 with $f(x, \frac{t}{T}) \leftarrow f_{gh}(x, \frac{t}{T})$ and $\bar{f}(x) \leftarrow \bar{f}_{gh}(x)$.

$\square$

This theorem might look a little obscure at first. In fact, there are three main issues with this approach.

1. The first issue is that one needs to design $g(v,t)$ appropriately to obtain a "nice" structure for the averaged vector field $\bar{f}_g(x, v)$. This is the most challenging part and we will come back to it at the end of this section after illustrating the previous theorem with some clarifying examples.

2. The second issue is associated with the computation of the averaged vector field $\bar{f}_g(x, v) = \int_0^T f(x, g(v, \tau)) d\tau$. This exact computation of the integral is possible only for simple systems, but in general it is not so. As we will see, flapping flight belongs to this class.

3. The third issue is associated with the period T. The theorem gives only an "existential" proof of the critical period T^* and the constant k for which the exact system can be approximated by the averaged system. In principle one would like to choose a very small period T, but in practice, the period T is constrained by technological limitations.

We will come back to all these problems at the end of this section, but for now we want to focus on the advantages of this approach. As shown in the next examples, high-frequency control and averaging are powerful tools to analyze and control a certain class of nonlinear systems.

The following example, for instance, shows how the approach can be applied to systems that cannot be stabilized by a static feedback.

Example 4.3.1.

Consider the following dynamical system:

$$\dot{x} = f(x, u) = 2u^2 - 1 \tag{4.16}$$

where the input u is bounded, i.e. $|u| \leq U$. This is the simplest model for the dynamics of insect vertical velocity during hovering, where u is position of the stroke angle of both wings and the

offset -1 plays the role of gravity, as will be shown in next chapter. We want to design a continuous control feedback such that the origin of the system is exponentially stable. It is immediately evident that this is not possible since the origin is not a feasible equilibrium point. Only $u(t) = a_0 \pm \frac{1}{\sqrt{2}}t$ would make the origin an equilibrium point, but it does not satisfy the constraints on u. The best we can do is to design a control feedback that approximately stabilizes the system close to the origin. To this purpose, consider the periodic control

$$u = g(v, \frac{t}{T}) = v\sin(2\pi\frac{t}{T})$$

where the amplitude v is a new control parameter. The dynamics of the system becomes:

$$\dot{x} = f_g(x, v, \frac{t}{T}) = 2v^2(\frac{2\pi}{T})^2\cos^2(2\pi\frac{t}{T}) - 1$$

Let us consider the averaged system

$$\dot{\bar{x}} = \frac{1}{T}\int_0^T f_g(\bar{x}, v, \frac{t}{T})dt = v^2(\frac{2\pi}{T})^2 - 1 \tag{4.17}$$

The origin of the averaged system is an equilibrium point for $v^* = \frac{T}{2\pi}$. We can now look for a stabilizing feedback for the averaged system. The simplest approach is to linearize the averaged system (4.17) about the equilibrium point $(x^*, v^*) = (0, \frac{T}{2\pi})$, which gives the following system:

$$\dot{\bar{x}}_l = \frac{2\pi}{T}(v - v^*)$$

Therefore if we choose

$$v = h(x) = v^* - \frac{T}{2\pi}\bar{x}_l$$

the origin of the averaged system is locally exponentially stable. By Theorem 4.3.1, we know that for sufficiently small T, the original system with the following feedback law:

$$u(x, \frac{t}{T}) = \frac{T}{2\pi}(1 - x)\sin(2\pi\frac{t}{T}) \tag{4.18}$$

converges to a T-periodic limit cycle whose magnitude is bounded by kT where $k > 0$. Figure 4.2 shows how the exact system (4.16) with feedback (4.18) converges to a periodic limit cycle near the origin whose magnitude decreases as the period decreases. Note also that the magnitude of the input decreases with the period due to the fact that it is the derivative of u that drives the system state x.

In the next example we show how a different choice of input parametrization $u = g(v,t)$ which still satisfies the assumptions of Theorem 4.3.1, gives rise to an improved approximation bound at any given period T.

Figure 4.2: The exact solutions (left) and corresponding inputs (right) of Example 4.3.1 for different periods T.

Example 4.3.2.

Consider the same dynamical system as above:

$$\dot{x} = f(x,u) = 2\dot{u}^2 - 1$$

where the input u is bounded, i.e. $|u| \leq U$. Consider now the following periodic control

$$u = g(v, \frac{t}{T}) = \begin{cases} v(4\frac{t}{T} - 1) & t \in [kT, kT + 0.5T) \\ v(1 - 4\frac{t - 0.5T}{T}) & t \in [kT + 0.5T, kT + T) \end{cases}$$

which is shown in Figure 4.3. The dynamical system becomes:

$$\dot{x} = f(x, g(v, \frac{t}{T})) = \frac{32}{T^2}v^2 - 1$$

The system is now time independent, therefore the averaged system is the same. The origin can be locally exponentially stabilized using the feedback law

$$v = h(x) = \frac{T}{4\sqrt{2}}(1 - x)$$
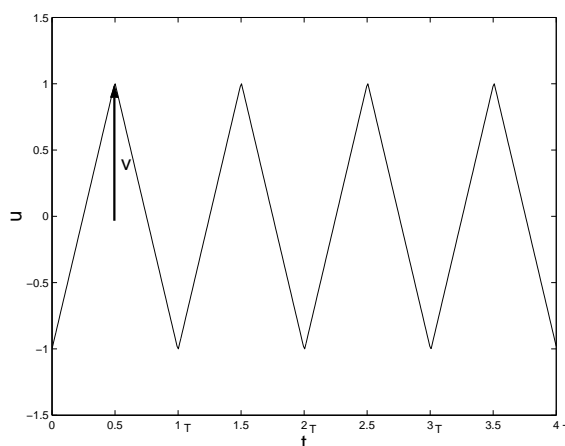
Figure 4.3: Sawtooth input with amplitude v.

so that the closed loop system becomes:

$$\dot{x} = (1-x)^2 - 1$$

Figure 4.4 shows that for the particular choice of periodic feedback, the limit cycle $x_T(t) = 0$ to which the solution of the exact system converges is identically zero. This is of course a fortunate co-incidence, but it indicates how different choices of the function $g(v,t)$ can affect the approximation for a given period T. This means that the value of the positive constant k that appears in $|x_T(t)| \leq kT$ depends on the particular choice of the functions $u = g(v,t)$ that we consider.

The next example illustrates how high frequency control can be used to virtually augment the number of control inputs in non-affine systems:

Example 4.3.3.

Consider the same dynamical system:

$$\begin{aligned} \dot{x} &= u \\ \dot{y} &= u^3 \end{aligned} \tag{4.19}$$

This is an underactuated system since the number of inputs is smaller than the degrees of free-dom. The origin of the system is an equilibrium point, but there is no continuous feedback law $u = u(x,y)$ that can exponentially stabilize it. This is because Brockett's necessary condition on smooth feedback stabilization [12] for a general continuously differentiable system $\dot{x} = f(x,u)$ with
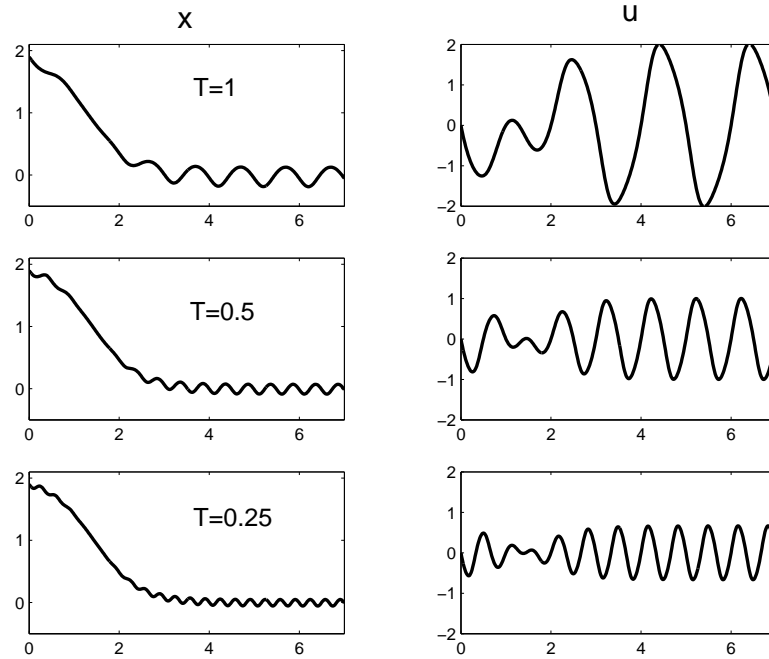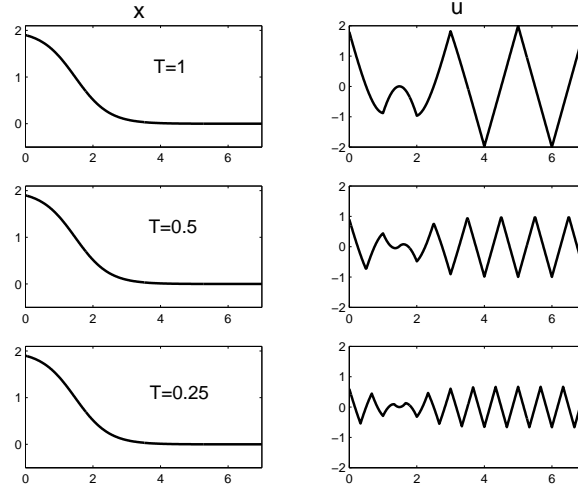
Figure 4.4: The exact solutions (left) and corresponding inputs (right) of Example 4.3.2 for different periods T.

$f(0,0) = 0$, requires that the mapping $\gamma: N \times \mathbb{R}^m \to \mathbb{R}^n$, where N is a neighborhood of the origin, and $\gamma: (x,u) \to f(x,u)$ should contain an open set of the origin. In our case, the image of the map is simply the curve $V = \{(x,y)| y = x^3\}$ which does not include an open set of the origin $(x,y) = (0,0)$. Consider now the following PWM-like periodic control

$$u = g(t,v_1,v_2) = \begin{cases} v_1 & t \in [kT, kT+0.75T) \\ -v_2 & t \in [kT+0.75T, kT+T) \end{cases} \tag{4.20}$$

where (v_1, v_2) are new control parameters. Figure 4.5 gives a graphical representation of the periodic control. Let us consider the averaged system:

$$\begin{aligned} \dot{\bar{x}} &= 0.75v_1 - 0.25v_2 \\ \dot{\bar{y}} &= 0.75v_1^3 - 0.25v_2^3 \end{aligned} \tag{4.21}$$

obtained by substituting Equation (4.20) into the system (4.19), and then averaging over a period T. The averaged system now has two inputs, and it is possible to show that the map $\phi: (v_1, v_2) \to (V_1, V_2)$ defined as follows:

$$V_1 = 0.75v_1 - 0.25v_2 \tag{4.22}$$
$$V_2 = 0.75v_1^3 - 0.25v_2^3, \tag{4.23}$$

is invertible, i.e. $(v_1, v_2) = \phi^{-1}(V_1, V_2)$ exists. In fact, the set of nonlinear Equations (4.22)-(4.23) can be solved by substituting $v_2 = 3v_1 - 4V_1$ from Equation (4.22) into Equation (4.23) and then
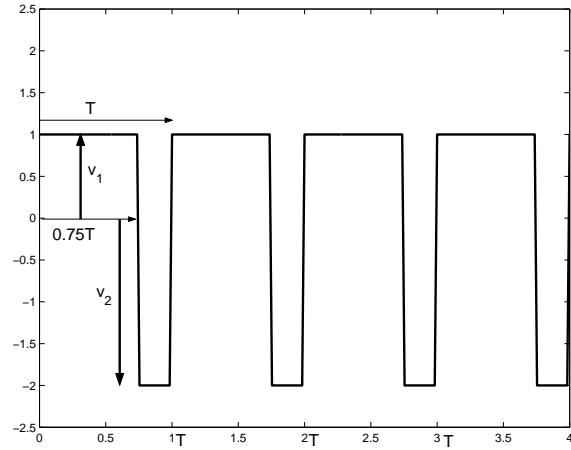
Figure 4.5: PWM input with varying amplitudes and duty-cycle $\rho = 0.75$.

finding the zeros of the third order algebraic equation in v_1. Since there is at least one real zero, the map ϕ can be inverted. Although it is not possible to find a closed solution for the real zero, the zero can be found easily with numerical algorithms. If we substitute the inverse map into the averaged system 4.21, we obtain:

$$
\begin{aligned}
\dot{\bar{x}} &= V_1 \\
\dot{\bar{y}} &= V_2
\end{aligned}
\tag{4.24}
$$

This means that the two degrees of freedom of the averaged system can be controlled independently. Therefore, an exponentially stabilizing feedback law $(V_1, V_2) = h(x, y)$ for the averaged system is given by:

$$
\begin{aligned}
V_1 &= -\bar{x} \\
V_2 &= -\bar{y}
\end{aligned}
\tag{4.25}
$$

Figure 4.6 shows the solutions of the closed loop solution given by the system:

$$
\begin{aligned}
\begin{bmatrix} \dot{x} \\ \dot{y} \end{bmatrix} &= \begin{bmatrix} u \\ u^3 \end{bmatrix} \\
u &= u(t, v_1, v_2) \quad \text{Equation (4.20)} \\
(v_1, v_2) &= \phi^{-1}(V_1, V_2) \quad \text{Equations (4.22)} - (4.23) \\
(V_1, V_2) &= h(x, y) \qquad \text{Equation (4.25)}
\end{aligned}
\tag{4.26}
$$
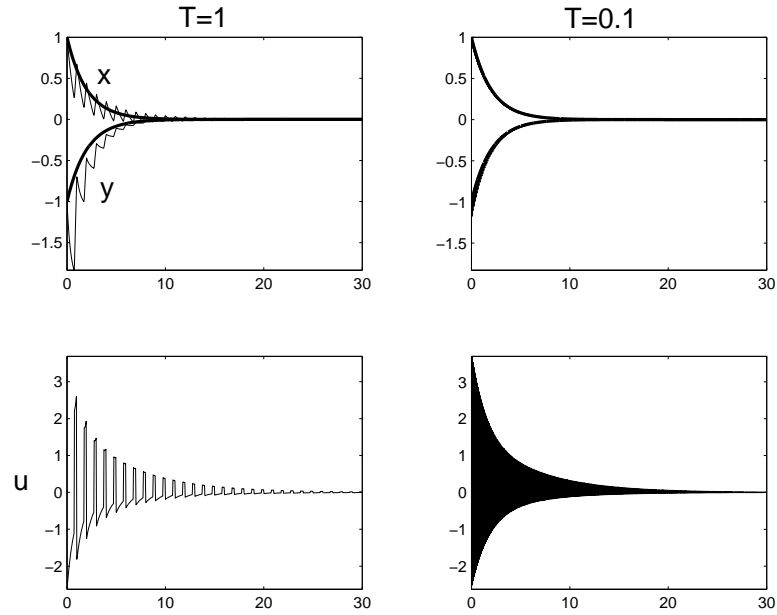
Figure 4.6: Stabilization to origin of Example 4.3.3 for different periods T (top) and corresponding control input u (bottom). The thick solid lines in top plots correspond to the solution of the averaged system, and the thin solid lines correspond to the exact solution.

Clearly, the origin is exponentially stable and the exact solution gets closer to the solution of the averaged system as the period T decreases.

The fact that the two degrees of the averaged system are decoupled means that the averaged system can track any desired trajectory $(x^*(t), y^*(t))$. From the theorem of averaging, it follows that the original system would exponentially converge to a trajectory that is close to the desired one, and the error becomes smaller as the period decreases. For example, consider the tracking of a figure-eight curve in the (x,y)-plane, given by $(x^*(t), y^*(t)) = (\sin(2\pi t), \sin(4\pi t))$. The closed loop system for tracking this curve is the same as the system (4.26) where the last equation is substituted with the following:

$$
\begin{aligned}
V_1 &= -(\bar{x} - \sin(2\pi t)) \\
V_2 &= -(\bar{y} - \sin(4\pi t))
\end{aligned}
\tag{4.27}
$$

Figure 4.7 illustrates the exact solution of original system for different time periods. It is evident how the approximation improves as the period decreases. Also note how the oscillations around the desired trajectory are greater when the tangent to the desired curve is negative. This is because it is not possible to generate a vector field with that orientation. In fact, the closed loop system

approximates that direction by zigzagging so that the mean vector field has negative direction over the course of a period.
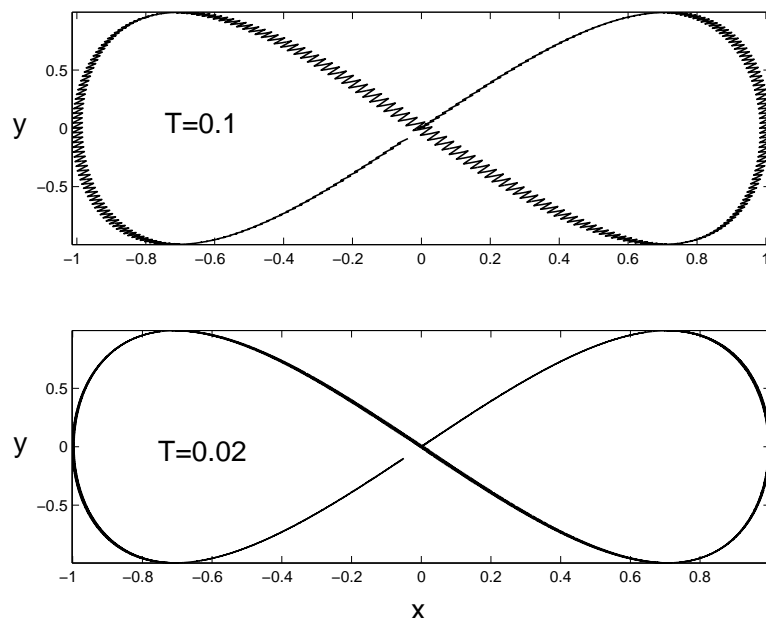
Figure 4.7: Tracking of figure-eight trajectory of Example 4.3.3 for different periods T.

The previous examples showed how high-frequency control can help design effective control law for systems which do not possess equilibrium points or cannot be stabilized via continuous feedback laws. Let us now go back to the three issues mentioned before:

1. In the previous examples we showed that a good choice of the input parametrization $u = g(v,t)$ leads to an averaged system which is simpler to control. However, we did not show how to design such a parametrization $g(v,t)$, given a general nonlinear system in the form $\dot{x} = f(x,u)$. The synthesis of "good" input parametrization $u = g(v,t)$ is in general a formidable problem and very few results are available. As mentioned at the beginning of this chapter, many researchers have tried to consider specific classes of nonlinear systems, and have given constructive algorithms to design the function $g(v,t)$. This has been done for driftless affine systems [73], and recently for a certain class of nonholonomic systems with drift [13] [46] [80]. Unfortunately, flapping flight cannot be reformulated within those frameworks. We will instead resort to biomimetic principles, i.e. we will design input parametrization based on observations of real flying insects. As we will show in the next chapter, these parametrizations

give rise to a simpler control problem.

2. In the examples above the averaged vector field could be computed explicitly, however in practical applications this is not possible. In general, one can compute the averaged vector field $\bar{f}(x,v)$ for an instantiation of the parameter vector v. It is therefore necessary to find an estimate $\hat{f}(x,v)$ of the true mean vector field $\bar{f}(x,v)$, based on a finite number of observations $\{v_n, \bar{f}(x,v_n)\}_{n=1}^{N}$. Even this problem is not easy in general. However, in the specific case of flapping flight, the computation of the mean vector field reduces to the estimation of the mean aerodynamic forces and torques over the course of a wingbeat. These forces and torques turn out to be well approximated by a linear relationship with the parameter vector v. The fact that the dependence is almost linear allows the use of simple least square algorithms to estimate $\bar{f}(x,v)$.

3. Finally, the choice of the period T is mainly dictated by technological constraints. Whether its value is sufficiently small is case-dependent and should be considered in advance. In the specific case of flapping flight, the wingbeat period of flying insects is small enough so that the theory developed in this chapter can be applied safely.

4.4   Averaging for multi-timescale systems

In the previous section, we assumed that we had perfect control over the input u in the system $\dot{x} = f_f(x,u)$. However, in many practical applications the control u cannot be controlled directly, but it is the output of another dynamical system, i.e. $\dot{u} = f_s(u,v)$, where v is the control input. For example, this is the case for mechanical systems where we have strong authority only over few mechanical parts. Consider, in fact, the case of a robotic flying insect. Initially, to simplify the controller design, we can assume that we can directly control the trajectory of the wings, but in reality they have their own dynamics that is controlled indirectly through the actuators. Therefore, in reality we have the following system:

$$\dot{x} = f_f(x,u) \tag{4.28}$$

$$\dot{u} = f_s(u,v) \tag{4.29}$$

Intuitively, if the dynamics of the wings is much faster than the dynamics of the insect body and we can track any desired wing trajectory, then it appears as if we can directly control the wing trajectories. This is illustrated in Figure 4.8 where there are two separated systems: one with fast

dynamics and one with slow dynamics. Initially, we assume that the input to the slow system, u, can be controlled directly and we search for a feedback control law $u = h(x)$ that can stabilize the state variable x to the desired state x^*. Then, we look for a stabilizing control feedback $v = g(u)$ for the
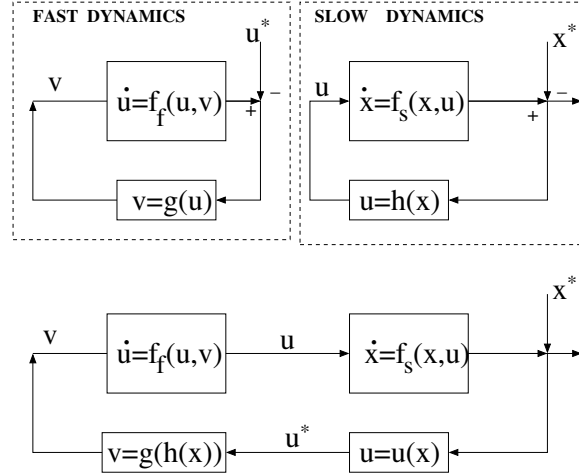
Figure 4.8: Block diagram for the two time-scale dynamical system. (Top) Disconnected modeling. (Bottom) Real interconnected system.

fast system that can track any desired trajectory u^* that belongs to the image of $u^* \in U = \{u \mid u = h(x)\}$. If we connect the two systems as in the bottom block diagram in Figure 4.8, then the overall system should be able to track the desired state x^* even if u cannot be controlled directly. In this section we give a formal proof of this controller design approach based on a two timescale system, which can be considered as an extension of singular perturbation methods that can be found in [38] and [37].

Consider the following system:

$$
\begin{aligned}
\dot{x} &= f(x, y) \\
\varepsilon \dot{y} &= Ay + v \\
v &= g(t, u) \\
u &= h(x)
\end{aligned}
\tag{4.30}
$$

where A is Hurwitz[1], $g(t, u)$ is T-periodic in t. The state y corresponds to the dynamics of the controlled mechanical part. The parameter ε is related to the ratio of the timescale between the two

---

[1] A matrix A is called Hurwitz if all its eigenvalues have negative real part.

systems. In fact, as explained at the beginning of this chapter, the parameter ε can be eliminated by re-scaling the time as $\tau = \frac{t}{\varepsilon}$ in the first equation in system (4.30). Therefore, the smaller ε is, the faster the dynamics of the state z relative to the state x is. The system model written in this form highlights a very important aspect of the two-timescale system driven by periodic input. In fact, in many mechanical systems, the function $f(x,z)$ is given, but the matrix A_z and the functions g and h can be designed. Therefore, the dynamics of the state z can be made as fast as desired. However, there is a price to pay; in fact, the magnitude of the input $v = \frac{1}{\varepsilon}g(\frac{\tau}{\varepsilon}, h(x))$ to the fast system must increase as ε decreases, which can be technologically difficult to achieve. We will explore this problem in the examples after we state the main theorems. The following theorem and lemma give a formal proof of the intuitive idea of decoupling two interconnected systems which have different timescales and designing two controllers separately.

The next theorem for autonomous systems is a preliminary theorem that will be extended for high-frequency perturbed singular systems.

Theorem 4.4.1. *Consider the perturbed system:*

$$\dot{x} = f(x,y) \tag{4.31}$$

$$\varepsilon\dot{y} = A_y y + \varepsilon p(x,y) \tag{4.32}$$

where $f(x,y)$ and $p(x,y)$ are continuously differentiable, $f(0,0) = 0$, and the matrices A_y and $A_x \triangleq \frac{\partial f}{\partial x}(0,0)$ are Hurwitz. Then there exists a positive constant ε^* such that, for $0 < \varepsilon < \varepsilon^*$, the system above has a unique equilibrium point $(x^*, y^*) = O(\varepsilon)$ and it is locally exponentially stable. Moreover, if $p(0,0) = 0$, then $(x^*, y^*) = (0,0)$ for all $0 < \varepsilon < \varepsilon^*$.

Proof. The proof for this theorem is a little tedious and it is moved to the Appendix at the end of this chapter. $\square$

The previous theorem can be extended to periodic non-autonomous systems:

Theorem 4.4.2. *Consider the perturbed system:*

$$\dot{x} = f(x,z) \tag{4.33}$$

$$\varepsilon\dot{z} = A_z z + g(x,t) \tag{4.34}$$

where $g(x,t) = g(x,t+T)$ and A_z is a Hurwitz matrix. Then there exists a unique function $h_T(x,t)$ such that

$$\varepsilon\frac{\partial}{\partial t}h_T(x,t) = A_z h_T(x,t) + g(x,t)$$

$$h_T(x,t+T) = h_T(x,t)$$

Assume also that the functions f, g, h and their partial derivatives up to the second order are continuous for all

$$(t, x, z, \varepsilon) \in [0, \infty) \times B_{r_1} \times B_{r_2} \times [0, \varepsilon_0]$$

where $B_r(x) \triangleq \{x \mid ||x|| \leq r\}$, and that origin of the system $\dot{x} = \bar{f}_T(x)$ is a locally exponentially stable equilibrium point, where the vector field $\bar{f}_T$ is defined as follows:

$$\bar{f}_T(x) = \frac{1}{T} \int_0^T f(x, h_T(x,t)) dt$$

Then there exist positive constants ε^*, T^*, and k such that, for all $0 < \varepsilon < \varepsilon^*$, and for all $0 < T < T^*$, the system (4.33)-(4.34) has a unique, locally exponentially stable, T-periodic solution $(x_{T,\varepsilon}(t), z_{T,\varepsilon}(t))$ function of T and ε, with the property

$$||x_{T,\varepsilon}(t)|| \leq k(\varepsilon + T)$$

$$||z_{T,\varepsilon}(t) - h_{T,\varepsilon}(0,t)|| \leq k(\varepsilon + T).$$

If in addition $\bar{p}(0,0) = 0$, where the function $\bar{p}(x,y)$ is defined as:

$$\bar{p}(x,y) = \frac{1}{T} \int_0^T \frac{\partial h_T}{\partial x}(x,t) f(x, h_\varepsilon(x,t) + y) dt$$

then

$$||x_{T,\varepsilon}(t)|| \leq kT$$

$$||z_{T,\varepsilon}(t) - h_{T,\varepsilon}(0,t)|| \leq kT$$

Proof. The function $h_T(x,t)$ is the steady state solution of Equation 4.32, when x is assumed to be constant. The existence, uniqueness and T-periodicity of $h_T(x,t)$ is a well known fact of periodically forced linear systems. Let us consider now the following change of variable $y = z - h_T(x,t)$. After multiplying both sides by ε and differentiating, we get:

$$\begin{aligned}
\varepsilon \dot{y} &= \varepsilon \dot{z} - \varepsilon \frac{\partial}{\partial t} h_T(x,t) - \varepsilon \frac{\partial}{\partial t} h_T(x,t) \dot{x} \\
&= A_z z + g(x,t) - A_z h_T(x,t) - g(x,t) - \varepsilon \frac{\partial}{\partial t} h_T(x,t) f(x,z) \\
&= A_z y - \varepsilon \frac{\partial}{\partial t} h_T(x,t) f(x, y + h(x,t))
\end{aligned}$$

Substituting this equation into Equations 4.33 and 4.34, we get:

$$\dot{x} = \varepsilon f(x, h_T(x,t) + y) = \varepsilon \tilde{f}(x,y,t) \tag{4.35}$$

$$\varepsilon \dot{y} = A_z y + \varepsilon \frac{\partial h_\varepsilon}{\partial x}(x,t) f(x, h_T(x,t) + y) = A_z y + \varepsilon p(x,y,t) \tag{4.36}$$

where the functions $\tilde{f}(x,y,t)$ and $p(x,y,t)$ are T-periodic in t. Now consider the averaged system:

$$\dot{\bar{x}} = \bar{f}(\bar{x},\bar{y}) \tag{4.37}$$

$$\dot{\bar{y}} = A_z\bar{y} + \varepsilon p(\bar{x},\bar{y}) \tag{4.38}$$

where

$$\bar{f}(x,y) = \frac{1}{T}\int_0^T \tilde{f}(x,y,t)dt = \frac{1}{T}\int_0^T f(x,h_T(x,t)+y)dt$$

$$\bar{p}(x,y) = \frac{1}{T}\int_0^T p(x,y,t)dt = \frac{1}{T}\int_0^T \frac{\partial h_T}{\partial x}(x,t)f(x,h_\varepsilon(x,t)+y)dt$$

By assumption, the origin of the system $\dot{x} = \bar{f}_T(x) = \bar{f}(x,0)$ is an exponentially stable equilibrium point, therefore $\frac{\partial \bar{f}}{\partial x}(0,0) = \frac{d\bar{f}_0}{dx}(0) = A_x$ is Hurwitz. The averaged system (4.37)-(4.38) satisfies the conditions of Theorem 4.4.1; therefore, the averaged system has a unique exponentially stable equilibrium point $(\bar{x}_\varepsilon^*, \bar{y}_\varepsilon^*)$ with the properties $||\bar{x}_\varepsilon^*|| \leq k_1\varepsilon$ and $||\bar{y}_\varepsilon^*|| \leq k_1\varepsilon$ for all $0 < \varepsilon < \varepsilon^*$, where ε^* is a positive constant. Since the equilibrium point of the averaged system is exponentially stable, then, by Theorem 4.2.1, there exist positive constants $T^*(\varepsilon)$ and k_2 such that, for all $0 < T < T^*(\varepsilon)$, the system (4.33)-(4.34) has a unique, locally exponentially stable, T-periodic solution $(x_{T,\varepsilon}(t), z_{T,\varepsilon}(t))$ with the property $||x_{T,\varepsilon}(t) - x_\varepsilon^*|| \leq k_2T$ and $||z_{T,\varepsilon}(t) - h_T(x_{T,\varepsilon}(t),t) - y_\varepsilon^*|| \leq k_2T$. Moreover, we have:

$$||x_{T,\varepsilon}(t)|| \leq ||x_{T,\varepsilon}(t) - x_\varepsilon^*|| + ||x_\varepsilon^*|| \leq k_2T + k_1\varepsilon$$

and

$$\begin{aligned}
||z_{T,\varepsilon}(t) - h_T(0,t)|| &\leq ||z_{T,\varepsilon}(t) - h_T(x_{T,\varepsilon}(t),t) - y_\varepsilon^*|| + \\
&+ ||h_T(x_{T,\varepsilon}(t),t) - h_T(0,t)|| + ||y_\varepsilon^*|| \\
&\leq k_2T + L||x_{T,\varepsilon}(t)|| + k_1\varepsilon \leq (1+L)(k_1\varepsilon + k_2T)
\end{aligned}$$

Setting $k = (1+L)\max(k_1,k_2)$ proves the second part of the theorem. If in addition $\bar{p}(0,0) = 0$, then $||x_\varepsilon^*|| = ||y_\varepsilon^*|| = 0$, therefore the inequalities reduce to $||x_{T,\varepsilon}(t)|| \leq kT$ and $||z_{T,\varepsilon}(t) - h_{T,\varepsilon}(0,t)|| \leq kT$, which concludes the proof. □

The following lemma extends the previous theorem to systems in which the input to the fast system is parameterized.

Lemma 4.4.1. *Consider the following controlled system:*

$$\dot{x} = f(x,z) \tag{4.39}$$

$$\varepsilon\dot{z} = A_zz + g(v,t) \tag{4.40}$$

where A_z is a Hurwitz matrix, g is T-periodic in t, and the functions f, g and their partial derivatives are continuous up to second order. Let the function $h_T(v,t)$ be the steady state solution of the subsystem (4.40), i.e.

$$\frac{dh_T(v,t)}{dt} = A_z h_T(v,t) + g_\varepsilon(v,t)$$

Let the vector field $\bar{f}(x,v)$ be defined as follows:

$$\bar{f}(x,v) = \frac{1}{T} \int_0^T f(x, h_T(v,t)) dt$$

If there exists a feedback law $v = l(x)$, such that the origin of the system $\dot{x} = \bar{f}(x, l(x))$ is exponentially stable, then there exist positive constants ε^*, T^* and k such that, for all $0 < \varepsilon < \varepsilon^*$ and for all $0 < T < T^*$ the system (4.39)-(4.40) has a unique, locally exponentially stable, T-periodic solution $(x_{T,\varepsilon}(t), z_{T,\varepsilon}(t))$ with the property $\|x_{T,\varepsilon}(t)\| \leq k(\varepsilon + T)$ and $\|z_{T,\varepsilon}(t) - h_T(l(0),t)\| \leq k(\varepsilon + T)$. If in addition $\bar{p}(0,0) = 0$, where the function $\bar{p}(x,y)$ is defined as:

$$\bar{p}(x,y) = \frac{1}{T} \int_0^T \frac{\partial h_T}{\partial u}(l(x),t) \frac{dl}{dx}(x) f(x, h_T(l(x),t) + y) dt$$

then $\|x_{T,\varepsilon}(t)\| \leq kT$ and $\|z_{T,\varepsilon}(t) - h_T(l(0),t)\| \leq kT$.

Proof. The proof follows directly from Theorem 4.4.2, by substituting the feedback law $v(x)$ into system (4.39)-(4.40). □

Remark Note that a sufficient condition for the existence of a exponentially stabilizing law $v = v(x)$ is that the linearized averaged system

$$\dot{x}_l = \frac{\partial \bar{f}}{\partial x}(0,0)x_l + \frac{\partial \bar{f}}{\partial v}(0,0)u = Ax_l + Bv$$

is stabilizable. In fact, if (A, B) is stabilizable, then there exist linear feedback laws $v = Kx$ that stabilize the origin. This is an important fact for two reasons: the first reason is that it is possible to use standard linear system theory tools to design the matrix K, and the second reason is that it is easy to implement physically the feedback $v = Kx$. As we will see in next chapter, the averaged dynamics of flapping flight possess this controllability property, thus making the design of controllers much simpler.

The following examples illustrate some of the most important aspects of the theorems and lemma given above and show how to design controllers for systems with input.

Example 4.4.1.
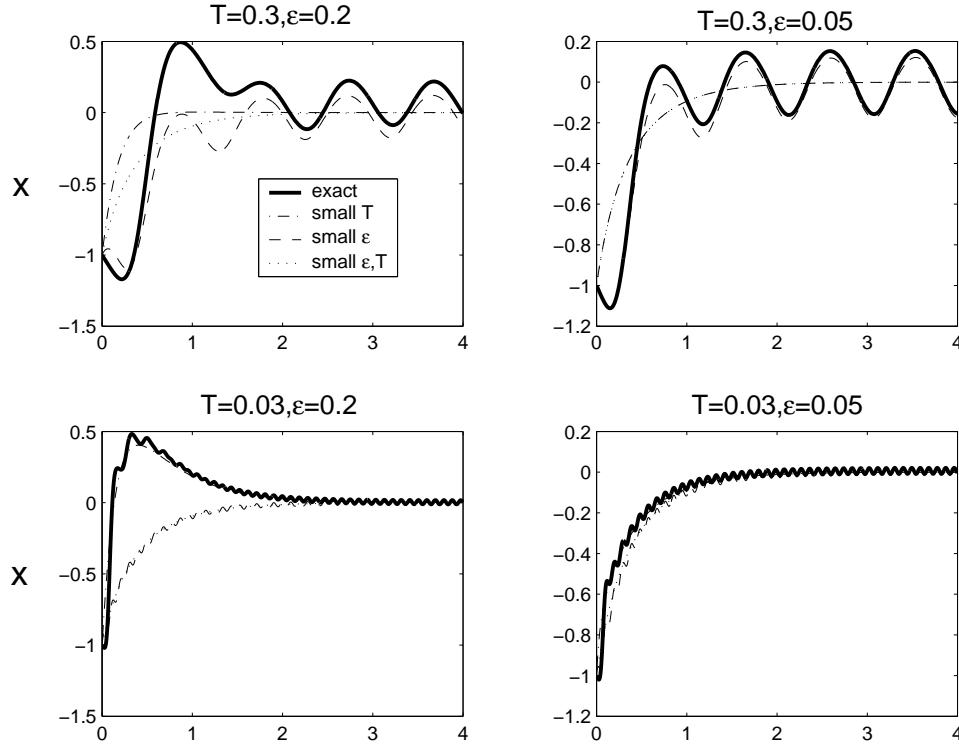
Figure 4.9: Solutions of state x for closed loop feedback of Example 4.4.1 for different value of parameter ε and T. The different traces correspond to System (4.42) (exact), System (4.43) (small ε), System (4.44) (small T), and System (4.45) (small ε, T).

Consider the dynamical system:

$$\begin{aligned}
\dot{x} &= f(x,z) = 2z^2 - 1 \\
\dot{z} &= -\frac{1}{\varepsilon}z + u \\
u &= \frac{1}{\varepsilon}v\sin(\frac{t}{T})
\end{aligned} \tag{4.41}$$

where v is a control parameter. Our goal is to find a function $v = l(x)$ that stabilizes the origin of the slow system x. As shown in Example 4.3.1, the origin is not an equilibrium point for the system, therefore the best we can hope for is finding a feedback law $v = l(x)$ that exponentially stabilizes the origin x of the averaged system. Let us assume at first that v is constant. Then the steady state solution $h(v,t)$ of the fast dynamics $\dot{z} = -z + v\sin(\frac{t}{T})$ is given by:

$$h(u,t) = v\frac{T}{\sqrt{\varepsilon^2 + T^2}}\sin(\frac{t}{T} - \phi)$$

T=0.3, ε=0.2   T=0.3, ε=0.05

T=0.03, ε=0.2   T=0.03, ε=0.05
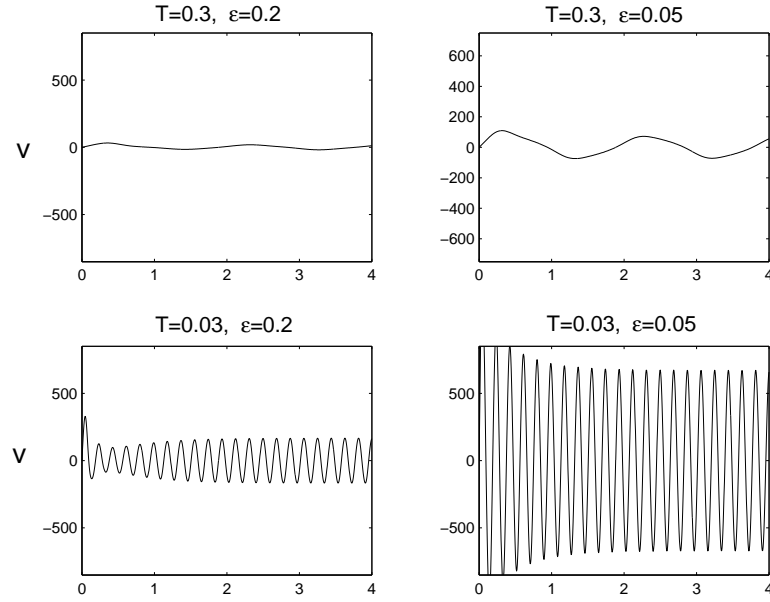
Figure 4.10: Input v for closed loop feedback corresponding to Figure 4.9

where $\phi = \tan^{-1}(\frac{\varepsilon}{T})$. The averaged vector field as defined in Theorem 4.4.2 is given by:

$$\bar{f}(x,h(v,t)) = \frac{1}{T}\int_0^T f(x,h(v,t))dt = v^2\frac{T^2}{\varepsilon^2+T^2} - 1$$

As shown in Example 4.3.1 a locally stabilizing control law for the origin is

$$v = l(x) = \frac{\sqrt{\varepsilon^2+T^2}}{T}(1-x)$$

so that the closed loop system becomes:

$$\begin{aligned}
\dot{x} &= 2z^2 - 1 \\
\dot{z} &= -\frac{1}{\varepsilon}z + \frac{\sqrt{\varepsilon^2+T^2}}{\varepsilon T}(1-x)\sin(\frac{t}{T})
\end{aligned}$$ (4.42)

Figure 4.9 shows some simulations of the closed loop system for different values of T and ε. From Figure 4.9 it is clear that the parameter ε affects the responsiveness of the closed loop behavior; a small value of ε increases the ratio between the timescales of the slow and fast dynamics, so that the slow system behaves closely to

$$\begin{aligned}
\dot{x} &= f(x,h_T(l(x),t)) = 2(1-x)^2\sin^2(\frac{t}{T}-\phi) - 1 \\
z(t) &= h_T(l(x),t) = (1-x)\sin(\frac{t}{T}-\phi)
\end{aligned}$$ (4.43)

The period T of the forcing function affects the accuracy of approximation between the exact system and the averaged system, i.e. for small values T the system behaves closely to

$$
\begin{aligned}
\dot{x} &= \bar{f}(x,y) = (1-x)^2 + 2y^2 - 1 \\
\dot{y} &= -\frac{1}{\varepsilon}y + \bar{p}(x,y) = -\frac{1}{\varepsilon}y + 2(1-x)y
\end{aligned}
\tag{4.44}
$$

where $y = z - h_T(l(x),t)$ and the functions $\bar{f}$ and $\bar{p}$ are defined in Theorem 4.4.2.

If both T and ε are very small then the system behaves as:

$$
\begin{aligned}
\dot{x} &= f(x, h_T(l(x),t)) = (1-x)^2 - 1 \\
z(t) &= h_T(l(x),t) = (1-x)\sin^2(\frac{t}{T} - \phi)
\end{aligned}
\tag{4.45}
$$

It is important to notice how ε and T affect the input signal v given by:

$$
v(x,t) = \frac{1}{\varepsilon}l(x)\sin(\frac{t}{T}) = \frac{\sqrt{\varepsilon^2 + T^2}}{\varepsilon T}(1-x)\sin(\frac{t}{T})
\tag{4.46}
$$

Figure 4.10 shows the input signal v corresponding to the simulations of Figure 4.9. Clearly, both parameters have the effect of requiring a larger amplitude, thus evidencing a tradeoff between accuracy and responsiveness of overall system versus input magnitude and frequency limitations.

In the next example we consider a slightly different system that does not strictly belong to the class of systems considered, but which still presents a separation of timescales. This system, being an archetype for many mechanical systems driven by actuators, plays an important role in many practical applications, including the wings-thorax dynamics considered in the next Chapter.

Example 4.4.2.

Consider the following system:

$$
\begin{aligned}
\dot{x} &= f(x,z,\dot{z}) = 2\dot{z}^2 - 1 \\
m\ddot{z} &= -b\dot{z} - kz + v
\end{aligned}
$$

where x is the variable we want to control, and it is driven indirectly by a simple second order mechanical system z. The goal is to design a control input $v = v(x,z,t)$, such that the variable x can be stabilized, at least approximately, around the origin. This is a typical case for a mechanical system, where mass and damping are in general fixed, but the stiffness of the structure can be chosen.
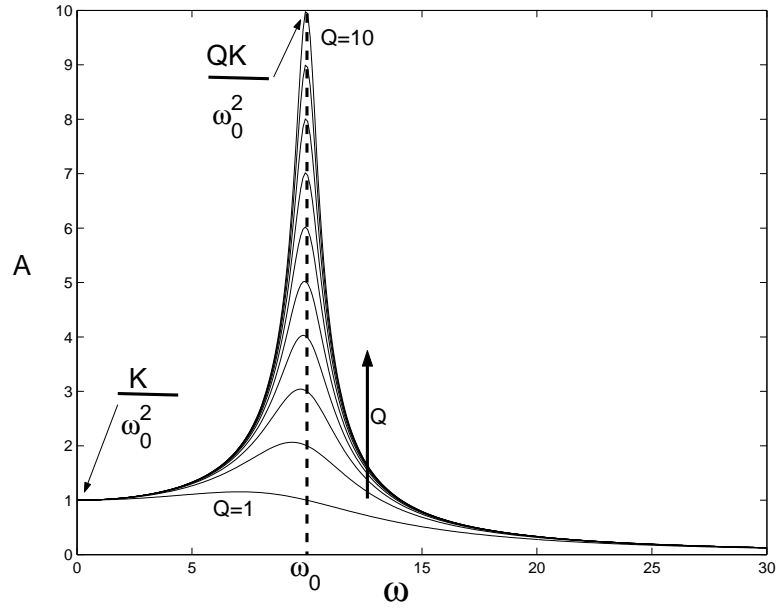
Figure 4.11: Magnitude of transfer function of a general second order system

As shown in the previous examples, the variable x cannot be stabilized to any point x^*, therefore we resort to a high-frequency signal control input:

$$v(u,t) = u\sin(\omega t)$$

The steady state solution $h_\omega(u,t)$ of the position of the mechanical system is:

$$h_\omega(u,t) = Au\sin(\omega t + \phi)$$

where $A = A(\omega, m, b, k)$ and $\phi = \phi(\omega, m, b, k)$ are the magnitude and the phase of the transfer function $T(s) = \frac{1}{ms^2 + bs + k}$, i.e. $A(\omega) = |T(j\omega)|$ and $\phi = \angle T(j\omega)$. Assuming as usual that the dynamics of the variable z is much faster than the dynamics of the variable x, we can consider the approximation $z \simeq h_\omega(u,t)$, which leads to the following approximate dynamics for the variable x:

$$\dot{x} = 2\omega^2 A^2 u^2 \cos^2(\omega t + \phi) - 1$$

By choosing the following control feedback $u = l(x) = \frac{1}{\omega A}(1 - x)$ the dynamics of the system becomes:

$$\dot{x} = 2(1-x)^2 \cos^2(\omega t + \phi) - 1$$
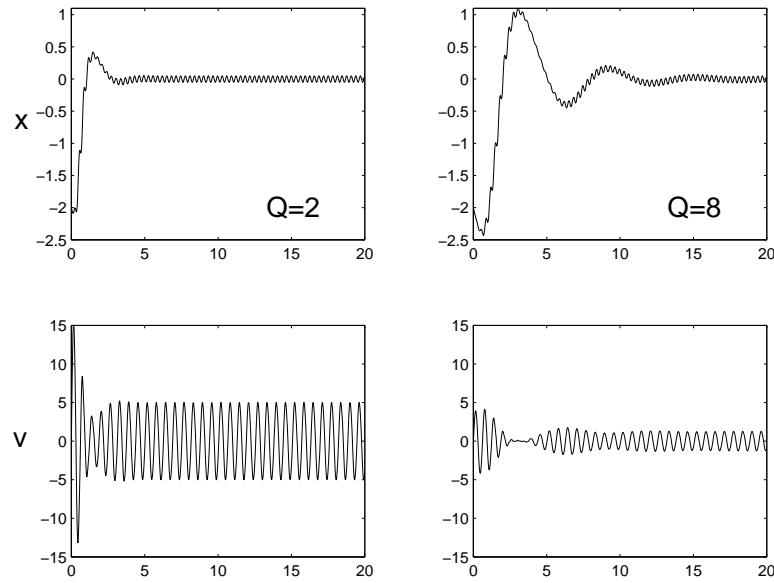
Figure 4.12: Close loop system of Example 4.4.2 for different values of the quality factor Q. State x (*top*). Input v (*bottom*).

which was studied in some of the previous examples. Therefore, the input to the system becomes:

$$v(x,t) = \frac{1}{\omega A}(1-x)\sin(\omega t)$$

Now we want to explore how the parameters m, b, k, ω affect the dynamics of the variable x. Let us first rewrite the transfer function as follows:

$$T(s) = \frac{K}{s^2 + \frac{\omega_0}{Q}s + \omega_0^2}$$

where $K = \frac{1}{m}$ is the static gain, $\omega_0 = \sqrt{\frac{k}{m}}$ is the resonant frequency, and $Q = \frac{\sqrt{mk}}{b}$ is the quality factor. Figure 4.11 show the magnitude A as a function of the parameters Q, ω_0, K.

From a technological point of view it is desirable to keep the magnitude of input v as small as possible, since this means we can use smaller actuators. This is equivalent to making the magnitude of the transfer function A as large as possible. A natural approach is to design the system that is driven by a signal close to the resonant frequency ω_0, i.e. $\omega = \omega_0$, and to choose a large value for the quality factor. In fact the magnitude at resonant frequency is $A(\omega_0) = \frac{QK}{\omega_0^2}$. Let us consider the dynamics of the system with input

$$v(x,t) = \frac{\omega_0}{Q}(1-x)\sin(\omega_0 t)$$
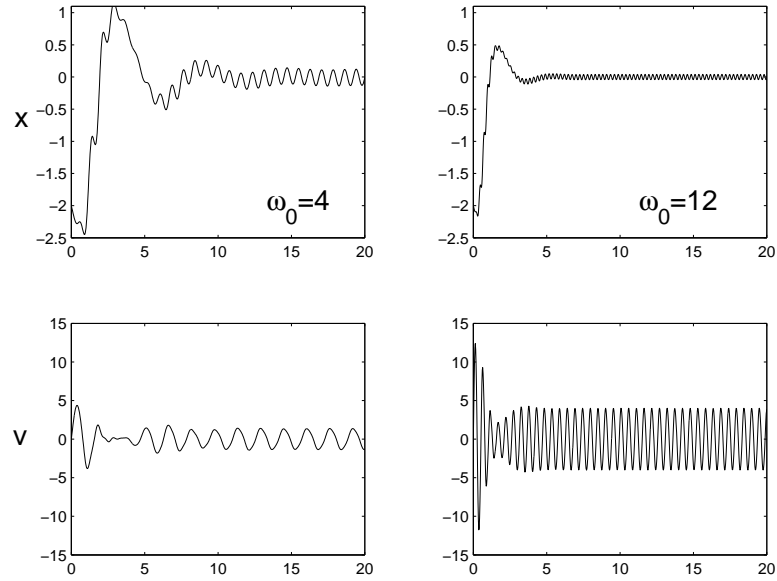
Figure 4.13: Close loop system of Example 4.4.2 for different values of the resonant frequency ω_0. State x (*top*). Input v (*bottom*).

for different values of Q. Figure 4.12 shows that a larger quality factor requires a smaller magnitude for the control input v, but the convergence to the steady state of the variable x is slower. This is because the dynamics of the mechanical system becomes slower as Q increases. In fact, the poles of the mechanical system are given by:

$$\lambda = \frac{\omega_0}{2Q} \pm j\omega_0 \sqrt{1 - \frac{1}{4Q^2}} \approx \frac{\omega_0}{2Q} \pm j\omega_0 = \frac{1}{\tau_c} \pm j\frac{2\pi}{T}$$

where the approximation holds for $Q > 2$, $\tau_c = \frac{2Q}{\omega_0}$ is the time constant associated with the exponential decay of the mechanical system, and $T = \frac{2\pi}{\omega_0}$ is the period of the resonant frequency, i.e. the modes of the mechanical system are $e^{-\frac{t}{\tau_c}} \sin(\frac{2\pi}{T})$ and $e^{-\frac{t}{\tau_c}} \cos(\frac{2\pi}{T})$. It is clear that a larger value of Q corresponds to a longer settling time.

If we keep the quality factor Q constant and we vary the resonant frequency ω_0, then the overall system is more responsive since τ_c decreases, and the magnitude of the limit cycle decreases since T decreases. However, the magnitude of the control input increases, as shown in Figure 4.13. Let us now explore the change in dynamics when one of the physical parameters of the mechanical systems is changed. In general, it is hard to modify the viscous damping b, therefore we focus only on the stiffness k and the mass m. Suppose first that the mass is constant and we vary the stiffness. Figure 4.14 shows how a larger k decreases the magnitude of the ripple in the variable
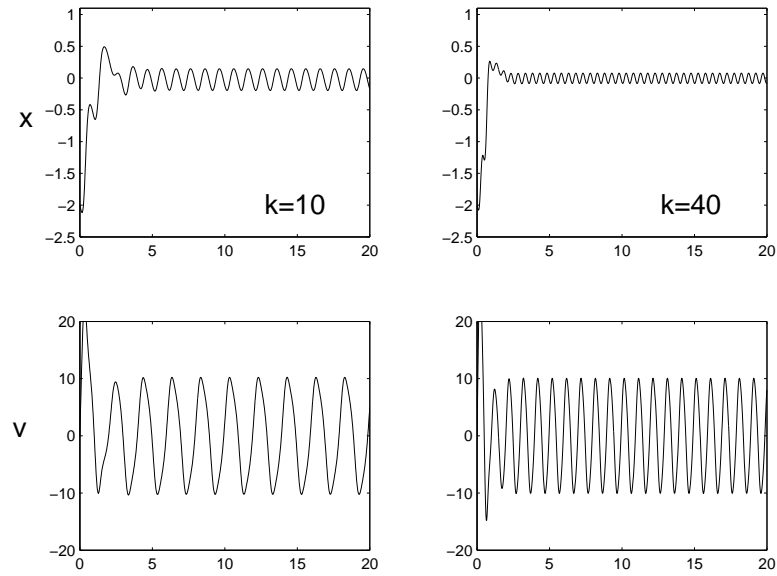
Figure 4.14: Close loop system of Example 4.4.2 for different values of the stiffness k. State x (*top*). Input v (*bottom*).

x, while the responsiveness and the magnitude of the input v are constant. This can be understood by observing that the time constant of the decay $\tau_c = \frac{2Q}{\omega_0} = \frac{2m}{b}$ remains constant, the time period of the frequency $T = \frac{2\pi}{\omega_0} = 2\pi\sqrt{\frac{m}{k}}$ decreases, and the amplification M of the input $v = Mu\sin(\omega_0 t)$ given by $M = \frac{1}{\omega_0 A} = \frac{Q}{\omega_0} = \frac{m}{b}$ is constant. Suppose first that the stiffness is constant and we vary the mass. Figure 4.15 shows how a larger m increases the magnitude of the ripple in the variable x, reduces the responsiveness of x, but also reduces magnitude of the input v. As above, this can be understood by observing that the time constant of the decay $\tau_c = \frac{2Q}{\omega_0} = \frac{2m}{b}$ increases, the time period of the frequency $T = 2\pi\sqrt{\frac{m}{k}}$ increases, and the amplification of the input v given by $M = \frac{m}{b}$ increases. Table 4.4 summarizes the affect of the mechanical parameters on the dynamics of the system. Clearly, it highlights the main tradeoffs of each parameter. In fact, requiring a better

	Ripple magnitude	Responsiveness	Input amplification	Period of forcing
Q	const.	$\frac{1}{Q}$	Q	constant
ω_0	$\frac{1}{\omega_0}$	ω_0	$\frac{1}{\omega_0}$	$\frac{1}{\omega_0}$
k	$\frac{1}{\sqrt{k}}$	const.	const.	$\frac{1}{\sqrt{k}}$
m	$\sqrt{m}$	$\frac{1}{m}$	m	$\sqrt{m}$

Table 4.1: Variations of dynamical parameters versus mechanical parameter of second order mechanical system. The variations are to be intended to be proportional to values in the table entries.
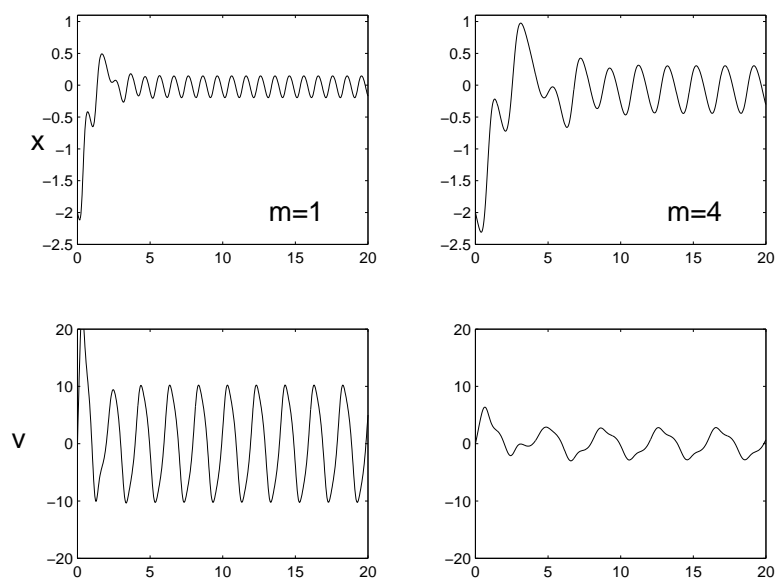
Figure 4.15: Close loop system of Example 4.4.2 for different values of the mass *m*. State *x* (*top*). Input *v* (*bottom*).

performance on one of the performance metrics necessarily leads to a worse performance for some others. Therefore, the optimal choice of mechanical parameters is dictated by the specific dynamical system and the constraints in the design.

4.5   Conclusions

In this chapter we presented the mathematical tools necessary to analyze insect flight and to design flight controllers. These tools are based on averaging theory, which approximates periodic time-varying vector fields with their averages. We showed that if the period of the vector field is sufficiently small, the trajectories of systems remain close to the trajectories obtained considering the average of the vector field over a period. Besides, if the averaged system is exponentially stable then the original system converges to a periodic limit cycle which is close to the equilibrium point of the averaged system. The first original contribution of this chapter is to extend this fact to controlled systems using high-frequency control feedback (Theorem 4.3.1). This approach requires the design of a T-periodic time-varying feedback $u = g(v,t)$, where v is a parameter vector corresponding to virtual inputs. The major advantage is that for some particular systems in which the input u appears in a non-affine form, and with an appropriate function $g(v,t)$, the averaged system

$\bar{x} = \bar{f}_g(x, v) = \frac{1}{T} \int_0^T f(x, g(v, t)) dt$ can have a larger number of independent inputs than the original system $\dot{x} = f(x, u)$, as shown in Example 4.3.3. Therefore, this kind of control is particularly suitable for underactuated control systems. The major problem with this approach is that it is in general difficult to know how many *independent* virtual inputs can be obtained by using periodic feedback, and there is no constructive way to design the function $g(v, t)$. Moreover, different periodic functions $g_1(v, t)$ and $g_2(v, t)$ can lead to the same averaged system, i.e. $\bar{f}_{g_1}(x, v) = \bar{f}_{g_2}(x, v)$, but the approximation between the original system and the averaged system can differ substantially, as shown in Examples 4.3.1 and 4.3.2. These are fundamental problems and considerable current research goes into addressing them by using differential geometry and averaging as mentioned in the introduction of this dissertation. Particular attention has been given to sinusoidal control feedback of the kind $u(t) = \sum_{i=1}^n v_i \sin(\omega_i t + \phi_i)$ [73] [53] [80], since it is amenable to systematic analysis. However, it cannot be applied applied to systems that are not in affine form, i.e. that are not in the form $\dot{x} = f_0(x) + \sum_{i=1}^n g_i(x) u_i$. Although it always possible to transform a non-affine system $\dot{x} = f(x, u)$ into an affine system by adding integrators to the input, i.e. $u = y$ and $\dot{y} = v$, so that the system becomes

$$\dot{z} = \tilde{f}(z) + G(z)v = \begin{bmatrix} \dot{x} \\ \dot{y} \end{bmatrix} = \begin{bmatrix} f(x, y) \\ 0 \end{bmatrix} + \begin{bmatrix} 0 \\ I \end{bmatrix} v.$$

This extended system always has a drift, i.e. $f_0(x) \neq 0$, which makes its analysis much harder. This is the case for insect flight. As will be shown in the next chapter, the problem of designing the function $g(v, t)$ for insect flight will be solved using biomimetic principles, i.e. mimicking periodic trajectories as observed in real flying insects.

In the second part of this chapter, we considered systems for which the control input u cannot be controlled directly, but it is the output of another dynamical system, described by Equations (4.28)-(4.29). We showed that if the dynamics of the system (4.29) is linear, stable, and sufficiently faster than the system (4.28), then one can simply study the two systems separately as if they were disconnected. It is sufficient to find the steady state solution of the fast system as a function of the input parameters $h_T(v, t)$ and then substitute it into the slow system so that it appears as if the slow system can be controlled directly through the input v, i.e. $\dot{x} = f(x, h_T(v, t)) = \tilde{f}(x, v, t)$. This approach considerably simplifies the design of controllers.

It is important to note that all the theorems presented are existential, i.e. they only guarantee that if the system is sufficiently fast and the forcing period is sufficiently small, then the original system is stable, but they do not give a quantitative measure of the actual values. Proofs are based on Lyapunov theory, which is a worst case analysis, therefore a quantitative estimation of the values

would be overconservative. In practice, as a rule of thumb, the averaging theory can be applied to systems for which the frequency of the forcing is at least $3 - 5$ times larger than the bandwidth of the slow system, and separation of timescales can be applied to systems for which the bandwidth of the fast system is $3 - 5$ times larger than the bandwidth of the slow system, as shown in Examples 4.4.1 and 4.4.2.

4.6 Appendix

Theorem 4.6.1. Implicit Function Theorem

Assume that $f : \mathbb{R}^n \times \mathbb{R}^m \to \mathbb{R}^n$ is continuously differentiable at each point (x, y) of an open set $S \subset \mathbb{R}^n \times \mathbb{R}^m$. Let (x_0, y_0) be a point in S for which $f(x_0, y_0) = 0$ and for which the Jacobian matrix $\frac{\partial f}{\partial x}(x_0, y_0)$ is nonsingular. Then there exists a neighborhoods $U \subset \mathbb{R}^n$ of x_0 and neighborhoods $V \subset \mathbb{R}^m$ of y_0 such that for each $y \in V$ the equation $f(x, y) = 0$ has a unique solution $x \in U$. Moreover, the solution can be given as $x = g(y)$, where g is continuously differentiable at $y = y_0$.

Proof. The proof can be found in any advanced calculus textbook such as [2]. □

Proof of Theorem 4.4.1

Proof. Let us consider the function $h(z, \varepsilon) = h((x, y), \varepsilon) \triangleq (f(x, y), A_y y + \varepsilon p(x, y))$, where $z = (x, y)$. Clearly, for $\varepsilon \neq 0$, the equilibria of system given by Equations (4.31) and (4.32) are the same as the zeros of $h(z, \varepsilon) = 0$. Note that $h(0, 0) = 0$. Let us consider the matrix

$$\frac{\partial h}{\partial z}(0,0) = \left[\begin{array}{cc} \frac{\partial f}{\partial x}(0,0) & \frac{\partial f}{\partial y}(0,0) \\ \varepsilon \frac{\partial p}{\partial x}(0,0) & A_z + \varepsilon \frac{\partial p}{\partial y}(0,0) \end{array} \right]\Bigg|_{\varepsilon = 0} = \left[\begin{array}{cc} A_x & \frac{\partial f}{\partial y}(0,0) \\ 0 & A_z \end{array} \right]$$

Since A_x and A_y are Hurwitz matrices, then also $\frac{\partial h}{\partial z}(0,0)$ is Hurwitz, and therefore nonsingular. By the implicit function theorem, we have that, for all ε, $h(z, \varepsilon) = 0$ has a unique solution, and there exists a function $z^*(\varepsilon)$ such that $z^*(0) = 0$, $\frac{dz^*}{d\varepsilon}(0)$ exists, and $h(z^*(\varepsilon), \varepsilon) = 0$. As a consequence, there exists a positive ε^*, such that $||z^*|| < k\varepsilon$, and thus $||x^*|| < k\varepsilon$ and $||y^*|| < k\varepsilon$ for all $0 < \varepsilon < \varepsilon^*$. Note that if $p(0, 0) = 0$, then the origin of the system is an equilibrium point for all ε. Therefore, by uniqueness of solution, $(x^*, y^*) = (0, 0)$, for all $0 < \varepsilon < \varepsilon^*$. This proves the first part of the theorem.

Consider the following change of variables $\tilde{x} = x - x^*$ and $\tilde{y} = y - y^*$, to get the system:

$$\dot{\tilde{x}} = \varepsilon f(\tilde{x} + x^*, \tilde{y} + y^*) \tag{4.47}$$

$$\dot{\tilde{y}} = A_y \tilde{y} + A_y y^* + \varepsilon p(\tilde{x} + x^*, \tilde{y} + y^*) \tag{4.48}$$

By construction, the origin of this system is an equilibrium point. We now want to show that it is locally exponentially stable using Lyapunov arguments. Let the candidate Lyapunov function

$$V(\tilde{x}, \tilde{y}) \triangleq \tilde{x}^T P_x \tilde{x} + \tilde{y}^T P_y \tilde{y}$$

where P_x and P_y are positive definite matrices that solve the following Lyapunov equations $P_x A_x + A_x^T P_x = -I$ and $P_y A_y + A_y^T P_y = -I$. The matrices P_x and P_y exist since the matrices A_x and A_y are Hurwitz. In preparation to prove that the candidate Lyapunov function is indeed a Lyapunov function, let us note the following estimates in the neighborhood of the origin, for $||\tilde{x}|| \leq r$ and $||\tilde{y}|| \leq r$:

$$
\begin{aligned}
\left\| f(\tilde{x} + x^*, \tilde{y} + y^*) - \tfrac{\partial f}{\partial x}(x^*, y^*)\tilde{x} - \tfrac{\partial f}{\partial y}(x^*, y^*)\tilde{y} \right\| &\leq L_1(||\tilde{x}|| + ||\tilde{y}||)^2 \\
||\tfrac{\partial f}{\partial y}(x^*, y^*)|| &= L_2 \\
||\tfrac{\partial f}{\partial x}(x^*, y^*) - A_x|| &\leq \phi(\varepsilon) \\
||p(\tilde{x} + x^*, \tilde{y} + y^*) - p(x^*, y^*)|| &\leq L_3(||\tilde{x}|| + ||\tilde{y}||) \\
||P_x \tilde{x}|| &\leq L_4||\tilde{x}|| \\
||P_y \tilde{y}|| &\leq L_5||\tilde{y}|| \\
-||y||^2 + \varepsilon a ||y|| \, ||x|| &\leq -\tfrac{1}{2}||y||^2 + \varepsilon^2 a^2 ||x||^2
\end{aligned}
$$

where $\phi(\varepsilon)$ is a continuous strictly positive monotonic function with the property $\phi(0) = 0$. The existence of the function ϕ is guaranteed by the continuity of the functions $\frac{\partial f}{\partial x}(x^*, y^*)$, $x^* = x^*(\varepsilon)$ and $y^* = y^*(\varepsilon)$, and the fact $A_x = \frac{\partial f}{\partial x}(0, 0)$. Then the derivative of the Lyapunov candidate function V along the trajectories of system (4.47)-(4.48) is given by:

$$
\begin{aligned}
\dot{V} &= \varepsilon[\tilde{x}^T P_y f(\tilde{x} + x^*, \tilde{y} + y^*) + f^T(\tilde{x} + x^*, \tilde{y} + y^*)P_y \tilde{x}] + \tilde{y}^T(P_y A_y + A_y^T P_y)\tilde{y} + \\
&\quad + \varepsilon[\tilde{y}^T P_y p(\tilde{x} + x^*, \tilde{y} + y^*) + p^T(\tilde{x} + x^*, \tilde{y} + y^*)P_y \tilde{y}] + y^{*T}(P_y A_y + A_y^T P_y)\tilde{y}^* \\
&\leq \varepsilon\left[\tilde{x}^T(P_x A_x + A_x^T P_x)\tilde{x} + 2L_1 L_4 ||\tilde{x}||(||\tilde{x}|| + ||\tilde{y}||)^2 + 2\phi(\varepsilon)L_4||\tilde{x}||^2 + 2L_2 L_4||\tilde{x}|| \, ||\tilde{y}||\right] + \\
&\quad + \tilde{y}^T(P_y A_y + A_y^T P_y)\tilde{y} + 2\varepsilon L_3 L_5||\tilde{y}||(||\tilde{x}|| + ||\tilde{y}||) \\
&\leq -\varepsilon(1 - 4rL_1 L_4 - 2L_4\phi(\varepsilon))||\tilde{x}||^2 - (1 - 2\varepsilon L_3 L_5)||\tilde{y}||^2 + \\
&\quad + \varepsilon(4rL_1 L_4 + 2L_2 L_4 + 2L_3 L_5)||\tilde{x}|| \, ||\tilde{y}|| \\
&\leq -\varepsilon(1 - 4rL_1 L_4 - 2L_4\phi(\varepsilon))||\tilde{x}||^2 - (\tfrac{1}{2} - 2\varepsilon L_3 L_5)||\tilde{y}||^2 + \\
&\quad + \varepsilon^2(4rL_1 L_4 + 2L_2 L_4 + 2L_3 L_5)^2||\tilde{x}||^2 \\
&= -\varepsilon(1 - 4rL_1 L_4 - 2L_4\phi(\varepsilon) - L_6\varepsilon)||\tilde{x}||^2 - (\tfrac{1}{2} - 2\varepsilon L_3 L_5)||\tilde{y}||^2 \\
&\leq -\tfrac{\varepsilon}{2}||\tilde{x}||^2 - \tfrac{1}{4}||\tilde{y}||^2
\end{aligned}
$$

$$(4.49)$$

where $L_6 = (4rL_1L_4 + 2L_2L_4 + 2L_3L_5)^2$, and we used the fact $(||\tilde{x}|| + ||\tilde{y}||) \leq 2r$. The last inequality is true for all $0 < \varepsilon < \varepsilon^*$, $||\tilde{x}|| \leq r^*$ and $||\tilde{y}|| \leq r^*$, for some ε^* and r^* sufficiently small. This proves that the equilibrium point (x^*, y^*) for system (4.31)-(4.32) is locally exponentially stable. $\qquad \square$

Chapter 5

Attitude Control Design for MFIs

In this chapter we show how flapping flight belongs to the class of systems studied in the previous chapter, and we apply the techniques developed there in order to understand flapping flight dynamics and to design flight controllers.

As shown in Chapter 3, the insect dynamics can be written as:

$$
\begin{aligned}
\ddot{\Theta} &= (IW)^{-1}[\tau_a^b(t) - W\dot{\Theta} \times IW\dot{\Theta} - I\dot{W}\dot{\Theta}] \\
\ddot{\mathbf{p}} &= -\frac{c}{m}\dot{\mathbf{p}} - \mathbf{g} + \frac{1}{m}Rf_a^b(t)
\end{aligned}
\tag{5.1}
$$

where the vector $\Theta = [\varphi\ \theta\ \psi]^T$ represents the ZYX Euler angles, $W = W(\Theta)$ is transformation matrix from Euler angular velocity, $\dot{\Theta}$, to body angular velocity, ω^b, i.e. $\dot{\omega}^b = W\dot{\Theta}$, I is the insect moment of inertia relative to the body frame, $\mathbf{p}$ is the position of the insect center of mass relative to the fixed frame, c is the linear damping coefficient, and $R(\Theta) = e^{\hat{z}\psi}e^{\hat{y}\theta}e^{\hat{x}\varphi}$ is the rotation matrix. The matrices R and W are given by:

$$
R(\Theta) = \begin{bmatrix} c_\theta c_\psi & s_\phi s_\theta c_\psi - c_\phi s_\psi & c_\phi s_\theta c_\psi + s_\phi s_\psi \\ c_\theta s_\psi & s_\phi s_\theta s_\psi + c_\phi c_\psi & c_\phi s_\theta s_\psi - s_\phi c_\psi \\ -s_\theta & s_\phi c_\theta & c_\phi c_\theta \end{bmatrix}, \quad W(\Theta) = \begin{bmatrix} 1 & 0 & -s_\theta \\ 0 & c_\psi & s_\psi c_\theta \\ 0 & -s_\psi & c_\psi c_\theta \end{bmatrix}
\tag{5.2}
$$

where $c_\phi \equiv \cos\phi$ and $s_\phi \equiv \sin\phi$. An excellent account of kinematics and dynamics of rigid bodies can be found in [83].

The wrench due to the aerodynamic forces is a nonlinear function of the position and velocity of the wing stroke angle, ϕ, and the angle of attack, α, of both wings, i.e.

$$
\begin{aligned}
f_a^b(t) &= f_a^b(\phi_r,\dot{\phi}_r,\alpha_r,\dot{\alpha}_r,\phi_l,\dot{\phi}_l,\alpha_l,\dot{\alpha}_l) \\
\tau_a^b(t) &= \tau_a^b(\phi_r,\dot{\phi}_r,\alpha_r,\dot{\alpha}_r,\phi_l,\dot{\phi}_l,\alpha_l,\dot{\alpha}_l)
\end{aligned}
\tag{5.3}
$$

where the subscripts r, l stand for right and left wing, respectively. A mathematical model for these forces is given in Section 3.1.1.

The dynamics of the insect obtained by combining Equations (5.1) and (5.3) can be written in compact form as follows:

$$\dot{x} = f(x, u) = s(x) + S(x)w(u, \dot{u}) \tag{5.4}$$

$$w(u, \dot{u}) = \begin{bmatrix} f_a^b(u, \dot{u}) \\ \tau_a^b(u, \dot{u}) \end{bmatrix} \tag{5.5}$$

where $x = (\mathbf{p}, \dot{\mathbf{p}}, \Theta, \dot{\Theta})$ is the state vector, $u = (\phi_r, \alpha_r, \phi_l, \alpha_l)$ is the control vector, w is the wrench, and $s(x)$ and $S(x)$ are appropriate functions. The goal of this chapter is to design control laws $u = u(x, t)$, and then generate a desired trajectory or flight maneuver $x^*(t)$.

Let us focus on the stabilization of hovering flight, i.e. stabilization about the origin of the system $x^*(t) = 0$. We will see that stabilization of different flight modes can be synthesized using the same methodology developed for hovering. First of all it is clear that the origin $x = 0$ is not an equilibrium point for the system (5.4)-(5.5), i.e. there is no input $u^*(t)$ such that $s(0) + S(0)w(u^*(t), \dot{u}^*(t)) = 0$. This is because the wings need to flap back and forth to generate sufficient lift to balance the insect weight, thus making the insect body position, represented by x, oscillate. Therefore, there is no hope in finding a control feedback $u = u(x, t)$ that will stabilize the insect about the origin. The best that we can hope for is to find a feasible trajectory that is close to the hovering condition, i.e. $x^*(t)$ and $u^*(t)$ such that $\dot{x}^*(t) = s(x^*(t)) + S(x^*(t))w(u^*(t))$ for all t, and $||x^*(t)||$ is small, and then linearize the system about the trajectory $(x^*(t), u^*(t))$ to get a time varying linear system $\dot{\tilde{x}} = A(t)\tilde{x} + B(t)\tilde{u}$, where $\tilde{x} = x - x^*(t)$ and $\tilde{u} = u - u^*(t)$. Besides being difficult to find the pair $(x^*(t), u^*(t))$, the time-varying linear system is not any easier to stabilize about its origin than the exact system. We will tackle this problem differently.

As described in Chapter 2, flying insects require several wingbeats to complete a full maneuver such as a saccade, which means that the period of the wingbeat is smaller then the dynamics of the body. This observation suggests that averaging techniques such as those developed in the previous chapter are likely to be effective. Therefore we will look for periodic feedback laws $u = g(x, t)$ such that the origin of the averaged system is exponentially stable. If this is possible, then the original system will be stabilized about a periodic trajectory $x_T(t)$ that is close to the hovering flight mode (see Theorem 4.3.1). As explained in the previous chapter the "goodness" of the approximation between the exact system and the averaged system depends on how large the frequency of the wingbeat is relative to the bandwidth of dynamics of the body. Indeed, we will show that

in flapping flight the magnitude of the periodic trajectory $||x_T(t)||$ is practically undistinguishable from the origin, i.e. $||x_T(t)|| \simeq 0$.

The major difficulty with this approach resides in finding the function $g(x,t)$. As explained in the previous chapter, this is in general a difficult task and few tools are available to synthesize the function $g(x,t)$ starting from the structure of the system $\dot{x} = f(x,u)$. Moreover, in insect flight the aerodynamic forces and torques given by Equations (5.3) are complex functions of the position and velocity of the wings, which limit even further the use of analytical tools. We will solve the problem of synthesizing $g(x,t)$ by adopting biomimetic principles. In particular, we will first parameterize the trajectories of the wings according to a family of periodic functions that depend affinely on the parameters, i.e. $u = g(v,t) = g_0(t) + G(t)v$, where the vector $g_0(t)$ and the matrix $G(t)$ are T-periodic. This parametrization is chosen such that the wings trajectories mimic some of the wing kinematics observed in biological insects during flight. Then, we will estimate the mean vector field $\bar{f}(x,v) = \frac{1}{T} \int_0^T f(x,g(v,t))dt$ based on simulations, and finally we will design a feedback law $v = l(x)$ so that the origin of the mean vector field $\bar{f}(x,v)$ is exponentially stable. The critical step in this approach is the first one; as we will see, if the parametrization is chosen correctly, the design of the feedback law can be obtained using standard control theory tools for autonomous systems. Besides, once the mean vector field $\bar{f}(x,v)$ is known, the design of other flight modes such as cruising or steering, follows analogously.

The second part of this chapter will explore a simpler mechanical wing-thorax structure in which only the stroke angle ϕ can be controlled, while the angle of attack α is kept constant at 45° during both downstroke and upstroke and goes though a passive rotation at the inversion of motion. Moreover, the wing actuators are driven by a PWM control input, where the duty cycle, the amplitude, and the offset are changed on a wingbeat-by-wingbeat basis. This simpler electromechanical design is motivated by the fact that it is technologically easier to fabricate than a two-degree of freedom wing with analog feedback. We will show how this simpler design can still guarantee controllability of insect flight, thus making it viable alternative solution to the full two-degree of freedom wing with analog control of actuators.

5.1 Wing Kinematic Parametrization

In this section we describe how the wing trajectories $u(t)$ are parameterized according to biomimetic principles and how to compute the mean vector field.

The vector field for the insect dynamics given by Equations (5.4)-(5.5) has a particular

structure such that the averaged system for any input parametrization $u = g(v,t)$ is given by:

$$\begin{aligned}
\dot{\bar{x}} &= \bar{f}(\bar{x}, v) = \frac{1}{T} \int_0^T f(x, g(v,t))dt = s(\bar{x}) + S(\bar{x})\frac{1}{T} \int_0^T w(g(v,t), \dot{g}(v,t))dt \\
&= s(\bar{x}) + S(\bar{x})\bar{w}(v)
\end{aligned} \tag{5.6}$$

where

$$\bar{w}(v) = \frac{1}{T} \int_0^T w(g(v,t), \dot{g}(v,t))dt \tag{5.7}$$

Therefore, it is sufficient to calculate the mean wrench over a wingbeat $\bar{w}$ as a function of the wing trajectory parameters v, and then by substituting it into Equations (5.1), find the mean vector field $\bar{f}(x, v)$.

As described in Section 2.4 in Chapter 2, biological insects control aerodynamic torques and forces by modulating the kinematics of the wings, so that a small set of wing kinematics might be sufficient to generate all possible flight maneuvers. Among others, three main wing kinematic mechanisms adopted by insects seem to be particularly important for flight control purposes: *timing of rotation*, *stroke angle offset* and *stroke angle amplitude*. There is a strong evidence that if these parameters can be controlled independently, then it is possible to control the torque and force generation during flapping [77]. For example, a large (small) stroke angle amplitude would generate a large (small) lift. A positive (negative) stroke angle offset results in a nose-up (down) pitch torque. An advanced (delayed) timing of rotation at the end of the downstroke produces a backward (forward) thrust. Most real insects flap their wings along a symmetric trajectory with a stroke angle amplitude of around 120° and mean angle of attack of 45° on both downstroke and upstroke [27]. However, during saccades and other maneuvers, they modify their wing trajectory by changing the kinematic parameters described above. Based on these biologically inspired arguments, the problem of finding a good parametrization of wing trajectory to control the body dynamics reduces to parameterizing the wing trajectory in such a way to be able to *independently* control the three biokinematic parameters described above, i.e. timing of rotation, stroke angle offset and stroke angle amplitude. We will show how the biokinematic parameters map linearly to the mean torques and forces, and thus simplify the design of flight controllers.

The wing trajectory during a wingbeat is described using the stroke angle, ϕ and the rotation angle φ. The rotation angle is defined as the angle between the vertical plane and the wing profile (see Figure 5.1). It corresponds to the complement of the angle of attack α, i.e. $\varphi = 90^o - \alpha$. In particular, we want to find three parameters $\upsilon = (\beta, \rho, \gamma)$ and an affine parametrization of the wing
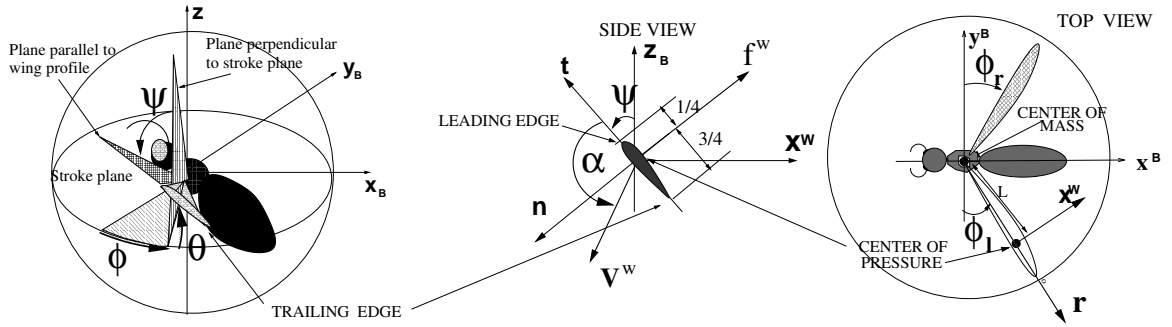
Figure 5.1: Definition of wing kinematic parameters: (*left*) 3D view of left wing, (*center*) side view of wing perpendicular to wing axis of rotation $\vec{r}$, (*right*) top view of insect stroke plane

angles as follow:

$$\phi(t;\upsilon) \quad = \quad g_\phi(t) + \gamma g_\gamma(t) + \rho g_\rho(t) \tag{5.8}$$

$$\varphi(t;\upsilon) \quad = \quad g_\varphi(t) + \beta g_\beta(t) \tag{5.9}$$

where the functions $g_i(t)$ are T-periodic functions, i.e. $g_i(t+T) = g_i(t)$. These functions are chosen based on the considerations above. In particular, $g_\varphi(t)$ and $g_\phi(t)$ generate a symmetric motion with maximum lift production, $g_\gamma(t)$ modifies only the stroke angle amplitude, $g_\beta(t)$ modifies only the timing of rotation of the angle of attack at the end of the downstroke, and $g_\rho(t)$ modifies only the offset of the stroke angle. Based on observations of real insect flight, we choose the following functions:

$$g_\phi(t) \quad = \quad \frac{\pi}{3} \cos(\frac{2\pi}{T}t) \tag{5.10}$$

$$g_\varphi(t) \quad = \quad \frac{\pi}{4} \sin(\frac{2\pi}{T}t) \tag{5.11}$$

$$g_\gamma(t) \quad = \quad g_\beta(t) = \frac{\pi}{15} \sin^3(\frac{\pi}{T}t) \tag{5.12}$$

$$g_\rho(t) \quad = \quad \frac{\pi}{15} \tag{5.13}$$

which are defined on the interval $t \in [0,T)$ and extended by periodicity so that $g_i(t+T) = g_i(t)$. A graphical representation is shown in Figure 5.2. This choice of the wing parametrization is not unique and it is the result of a sensible guess based on biomimetic principles. In fact, even if the parametrization given by Equations (5.10)-(5.13) might seem obscure at first sight, it gives rise to wing trajectories that mimic some of the trajectories observed in real insect. In fact, a positive (negative) value for γ results in a large (small) stroke angle amplitude; a positive (negative) value
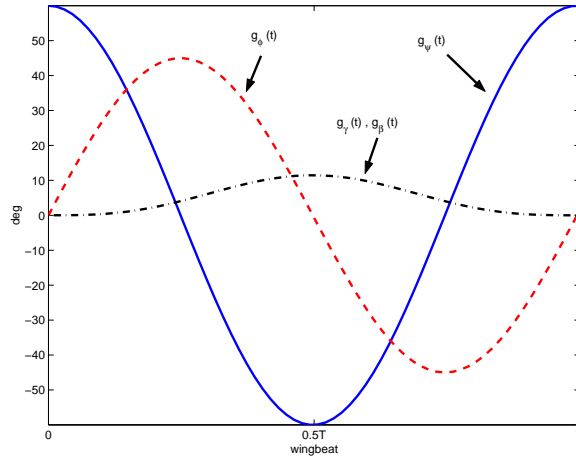
Figure 5.2: Wing kinematic parameterizing functions: $g_\phi(t)$ (*solid*), $g_\varphi(t)$ (*dashed*), $g_\gamma(t) = g_\beta(t)$ (*dashed-dotted*).

for β results in a delayed (advanced) timing of rotation at the end of the downstroke; a positive (negative) value of ρ shifts forward (backward) the offset of the stroke angle. If this parametrization above is mirrored for both wings, the wings kinematics $u = (\phi_r, \phi_l, \varphi_r, \varphi_l)$ can be written more compactly in terms of the kinematic parameters $v = (\gamma_r, \gamma_l, \beta_r, \beta_l, \rho_r, \rho_l)$ as follows:

$$u(v,t) = g_0(t) + G(t)v \tag{5.14}$$

$$g_0 = \begin{bmatrix} g_\phi \\ g_\phi \\ g_\varphi \\ g_\varphi \end{bmatrix}, \quad G = \begin{bmatrix} g_\gamma & 0 & 0 & 0 & g_\rho & 0 \\ 0 & g_\gamma & 0 & 0 & 0 & g_\rho \\ 0 & 0 & g_\beta & 0 & 0 & 0 \\ 0 & 0 & 0 & g_\beta & 0 & 0 \end{bmatrix}$$

where $g_0(t)$ and $G(t)$ are a T-periodic vector and matrix, respectively, whose entries are defined in Equations (5.10)-(5.13).

It is now possible to study the effect of the chosen parametrization on the mean wrench. In fact, if we substitute Equation (5.14) into Equation (5.7), we obtain a static map $\bar{w} : \mathbb{R}^6 \to \mathbb{R}^6$ from the wing parameters $v \in \mathbb{R}^6$ to the mean wrench $(\bar{f}_a^b, \bar{\tau}_a^b) \in \mathbb{R}^6$:

$$\bar{w}(v) = \begin{bmatrix} \bar{f}_a^b \\ \bar{\tau}_a^b \end{bmatrix} \tag{5.15}$$

This is a nonlinear map and cannot be computed analytically since the aerodynamic force and torque are complex functions of the wings angles and velocities (see Section 3.1.1). However, one can look

at its linearization at the origin of the wing parameters:

$$\bar{w}(v) = w_0 + Wv + \delta(v) \tag{5.16}$$

where $w_0 \triangleq w(0) \in \mathbb{R}^6$, $W \triangleq \frac{\partial w}{\partial v}(0) \in \mathbb{R}^{6\times 6}$, and $||\delta(v)|| = o(||v||)$ is the approximation error. Although, it is not possible to linearize analytically Equation (5.16) to obtain w_0 and W explicitly, one can try to estimate it. In fact, it is possible to randomly select different values for the parameter vector v, then substitute them into the parametrization given by Equation (5.14), and finally compute the mean wrench $\bar{w} = (\bar{f}_a^b, \bar{\tau}_a^b)$ via simulations. The approximating w_0 and W can then be found by rewriting Equation (5.16) as a least square (LS) problem where (w_0, W) are the unknowns. Simulations are performed based on the aerodynamic model described in Section 3.1.1, and on the morphological body parameters, such as wing length and position of the center of mass, of a typical blowfly, the MFI target model [82]. The approximating affine map is found to be:

$$w_0 = \begin{bmatrix} 0 \\ 0 \\ f_0 \\ 0 \\ 0 \\ 0 \end{bmatrix}, \quad W = \begin{bmatrix} W_f \\ W_\tau \end{bmatrix} = \begin{bmatrix} 0 & 0 & 0.1f_0 & 0.1f_0 & 0 & 0 \\ 0 & 0 & 0 & 0 & 0 & 0 \\ 0.15f_0 & 0.15f_0 & 0 & 0 & 0 & 0 \\ 0.05\tau_0 & -0.05\tau_0 & 0 & 0 & 0 & 0 \\ 0 & 0 & 0.01\tau_0 & -0.01\tau_0 & 0.05\tau_0 & 0.05\tau_0 \\ 0 & 0 & 0.06\tau_0 & -0.06\tau_0 & 0 & 0 \end{bmatrix} \tag{5.17}$$

where $W_f \triangleq \frac{\partial \bar{f}_a^b}{\partial v}|_{v=0}$ and $W_\tau \triangleq \frac{\partial \bar{\tau}_a^b}{\partial v}|_{v=0}$, $f_0 = mg$, $\tau_0 = mgR$. The parameters m, g and R are the insect mass, the gravity constant and wing length, respectively. The zeros entries correspond to estimated values that were negligible relative to the largest entries in same row. This approximation is quite accurate for values of the kinematic parameters smaller then unity, $||v||_\infty \leq 1$[1]. Figure 5.3 shows the predicted mean wrench $\hat{w}(v) \triangleq w_0 + Wv$ versus the exact mean wrench $\bar{w}(v)$ obtained from simulations for 200 random values of the wing parameter vector v in the unit box, i.e. $||v||_\infty \leq 1$.

The sparse structure of the matrix W is a consequence of the "good" parameterization based on the biological insights described at the beginning of this section and in Section 2.4. In fact, as expected, any component of the wrench depends additively or differentially on two parameters, depending if the wings are moving symmetrically or anti-symmetrically. Note that along the z-component the symmetrical wing motion, equivalent of setting $v = 0$ in Equation (5.14), generates a vertical lift sufficient to balance the insect body weight. The magnitude of the coefficients in the map are considerable: in fact the insect can generate forward or vertical thrust on the order of $0.2 - 0.4mg$, and angular torques of order $0.1 - 0.2mRg$, where R is the length of the wing. Only

---

[1]Let $v = (v_1, v_2, \ldots, v_n) \in \mathbb{R}^n$, then $||v||_\infty \triangleq \max_i |v_i|$
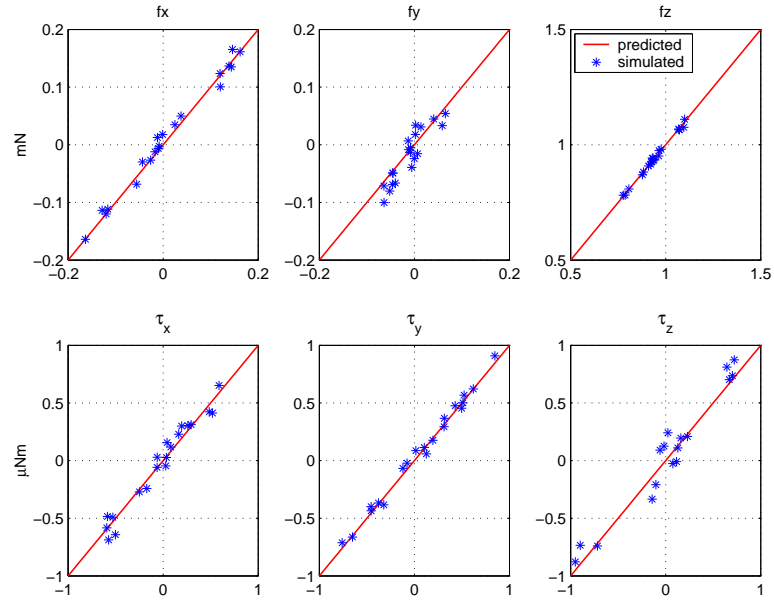
Figure 5.3: Simulations of exact mean wrench $\bar{w}$ (y-axes) versus the predicted mean wrench $\hat{w}$ (x-axes) given by map (5.17).

the lateral component of the wrench cannot be controlled, as one would expect since aerodynamic forces are almost perpendicular to the *y*-axis of the body frame.

From the map it is also clear that the three mean torques and the vertical and forward thrust can be controlled independently by choosing appropriately the values for the six wings parameters *v*. Equivalently, this means that there exists a matrix $T \in \mathbb{R}^{6 \times 5}$, such that the transformation $v = T\tilde{v}$ where $\tilde{v} = (\tilde{v}_1, \tilde{v}_2, \tilde{v}_3, \tilde{v}_4, \tilde{v}_5)$ gives:

$$\bar{w}(\tilde{v}) = w_0 + WT\tilde{v} + \delta(\tilde{v}) = \begin{bmatrix} 0 \\ 0 \\ f_0 \\ 0 \\ 0 \\ 0 \end{bmatrix} + \begin{bmatrix} \tilde{v}_1 \\ 0 \\ \tilde{v}_2 \\ \tilde{v}_3 \\ \tilde{v}_4 \\ \tilde{v}_5 \end{bmatrix} \tag{5.18}$$

Therefore, the wing kinematic parametrization chosen allows independent control of five degrees of freedom, as suggested by many biologists (see Section 2.4).

Now that we have an expression for the mean wrench as a function of the kinematic parameters, we can easily design a feedback controller to make the origin of the averaged dynamics

of the insect exponentially stable. This is done in the next section.

5.2 Control design for Hovering and Cruising flight Modes

Hovering

Following the guidelines described in the previous chapter, we can now look for a stabilizing controller for hovering by designing a feedback law $v = l(x)$ such that the origin of the averaged system (5.6) is exponentially stable. Consider the averaged system:

$$
\begin{aligned}
\ddot{\Theta} &= (WI)^{-1}[\bar{\tau}_a^b(v) - W\dot{\Theta} \times IW\dot{\Theta} - I\dot{W}\dot{\Theta}] \\
\ddot{\mathbf{p}} &= -\frac{c}{m}\dot{\mathbf{p}} - \mathbf{g} + \frac{1}{m}R\bar{f}_a^b(v)
\end{aligned}
\tag{5.19}
$$

which is obtained by substituting the mean wrench given by Equation (5.17) into the insect dynamics Equations (5.1). The origin of the system is an equilibrium point for $v = 0$. We linearize the system about the origin to get:

$$
\begin{aligned}
\ddot{\Theta} &= I^{-1}W_\tau v \\
\ddot{\mathbf{p}} &= -\frac{c}{m}\dot{\mathbf{p}} + \frac{1}{m}W_f v + g \begin{bmatrix} \bar{\theta} \\ -\bar{\varphi} \\ 0 \end{bmatrix}
\end{aligned}
\tag{5.20}
$$

where we used the assumption that $f_0 = mg$, W_τ and W_f are defined in Equation (5.17), and $\Theta = (\varphi, \theta, \psi)$. The averaged system can be written in state space representation as follows:

$$
\begin{bmatrix} \dot{\Theta} \\ \ddot{\Theta} \\ \dot{\mathbf{p}} \\ \ddot{\mathbf{p}} \end{bmatrix} = \begin{bmatrix} 0 & I & 0 & 0 \\ 0 & 0 & 0 & 0 \\ 0 & 0 & 0 & I \\ M & 0 & -\frac{c}{m}I & 0 \end{bmatrix} \begin{bmatrix} \bar{\Theta} \\ \dot{\bar{\Theta}} \\ \bar{\mathbf{p}} \\ \dot{\bar{\mathbf{p}}} \end{bmatrix} + \begin{bmatrix} 0 \\ I^{-1}W_\tau \\ 0 \\ \frac{1}{m}W_f \end{bmatrix} v, \quad M = \begin{bmatrix} 0 & g & 0 \\ -g & 0 & 0 \\ 0 & 0 & 0 \end{bmatrix}
\tag{5.21}
$$

where $I \in \mathbb{R}^{3\times3}$ is the identity matrix. This linear system is unstable but controllable, and therefore there exists a linear feedback law:

$$
v = l(x) = K_h x
\tag{5.22}
$$

that stabilizes the system, where $x = (\bar{\Theta}, \dot{\bar{\Theta}}, \bar{\mathbf{p}}, \dot{\bar{\mathbf{p}}})$. The matrix K_h can be found using standard techniques such as pole placement or linear quadratic regulation (LQR). For more details we refer the reader to [16]. Therefore using the following T-periodic feedback control
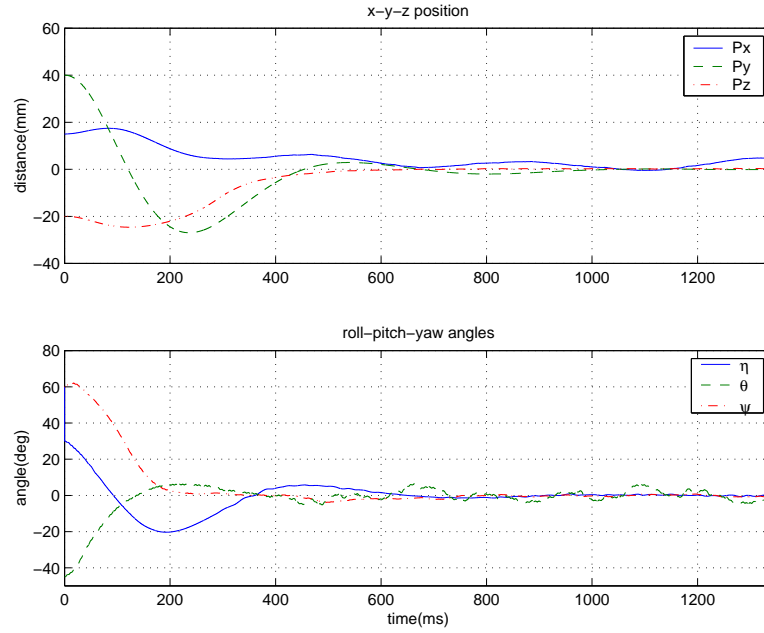
Figure 5.4: Hovering stabilization: Position (*top*). Euler angles (*bottom*)

$$u = u(K_h x, t) = g_0(t) + G(t)K_h x = g_0(t) + \tilde{G}_h(t)x \qquad (5.23)$$

where $g_0(t)$ and $G(t)$ are given by Equations (5.14), and $g_0(t)$ and $\tilde{G}(t)$ are T-periodic, the averaged system is locally exponentially stable. Therefore by Theorem 4.3.1, the original system exponentially converges to a periodic limit cycle $x_T(t)$. Figure 5.4 and 5.5 show the stabilization of hovering using the feedback law (5.23), where the matrix K has been designed using LQR. The weights in the LQR design have been chosen to take into consideration input saturation and system bandwidth. See [16] for additional details. In particular, the kinematic parameters v are voluntarily limited to unity , i.e. $||v||_\infty \leq 1$, to avoid excitation of nonlinearities, while the bandwidth of the closed loop system must be smaller than the frequency of the wingbeat to apply averaging arguments as explained in the previous chapter.

As predicted by the averaging theory, the dynamics for hovering stabilization exponentially converges to a periodic limit cycle. This can be clearly seen in the oscillation of pitch velocity displayed in center-right plot in Figure 5.5 which does not converge to zero. However, the magnitude of the oscillations of the body angles of the insect are so small that they are undetectable from a practical point of view; in fact, only the pitch angle exhibits an oscillatory behavior, but the amplitude of the ripple is smaller then 1° (barely noticeable in center-left plot in Figure 5.5).
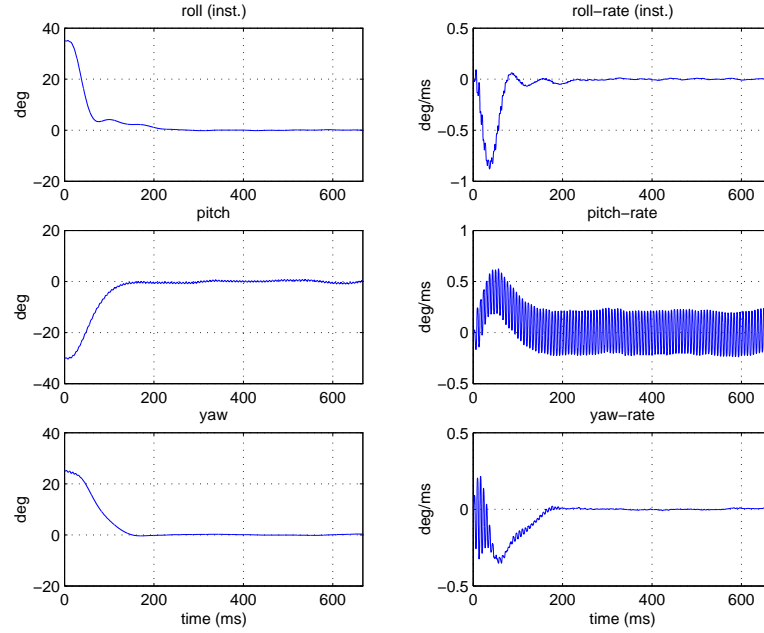
Figure 5.5: Hovering stabilization: detail of Euler angles (*left*), and corresponding angular velocities (*right*).

Cruising

We can follow the same methodology as given above to design controllers for cruising, i.e. to design a controller that stabilizes the trajectory $\dot{\mathbf{p}} = \mathbf{v}^*$ where $\mathbf{v}^*$ is the desired velocity. First we need to find a body configuration that makes the trajectory feasible. The choice is not unique since the flapping flight allows independent control of torques and vertical and forward thrust, as explained in the previous section. In general real insects pitch their body such that the mean force production balances the insect weight and the damping force. Therefore we will consider the configuration depicted in Figure 5.6. Without loss of generality we assume that the yaw angle is zero, i.e. the insect heading has the same direction as the desired velocity, so that the desired velocity can be written as $\mathbf{v}^* = (v_x^*, 0, v_z^*)$. The cruising pitch angle θ_0 is given by:

$$\theta_0 = \tan^{-1}\left(\frac{cv_x^*}{cv_z^* + mg}\right)$$

and the mean aerodynamic thrust f_0 is given by:

$$f_0 = \sqrt{(cv_z^* + mg)^2 + (cv_x^*)^2}$$

Therefore the configuration $x = (\Theta_0, \dot{\Theta}_0, \dot{\mathbf{p}}) = ((0, \theta_0, 0), (0, 0, 0), (v_x^*, 0, v_z^*))$ and $\bar{w}(0) = (\bar{\tau}_a^b, \bar{f}_a^b) = (0, 0, f_0, 0, 0, 0)$ is feasible for the averaged system. Let us linearize Equations (5.19) about the
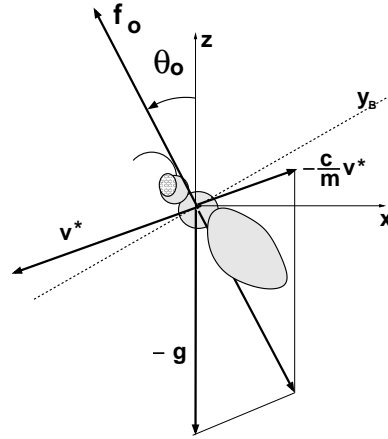
Figure 5.6: Cruising Configuration

feasible configuration to get:

$$
\begin{bmatrix} \dot{\Theta} \\ \ddot{\Theta} \\ \dot{\mathbf{v}} \end{bmatrix} = \begin{bmatrix} 0 & I & 0 \\ 0 & 0 & 0 \\ N_1 & 0 & -\frac{c}{m}I \end{bmatrix} \begin{bmatrix} (\Theta - \Theta_0) \\ \dot{\Theta} \\ (\overline{\mathbf{v}} - \mathbf{v}^*) \end{bmatrix} + \begin{bmatrix} 0 \\ (N_2 I)^{-1}W_\tau \\ 0 \\ \frac{1}{m}W_f \end{bmatrix} v
$$

$$
N_1 = \begin{bmatrix} 0 & \frac{f_0}{m}\cos\theta_0 & 0 \\ -\frac{f_0}{m} & 0 & \frac{f_0}{m}\sin\theta_0 \\ 0 & -\frac{f_0}{m}\sin\theta_0 & 0 \end{bmatrix}, \; N_2 = \begin{bmatrix} 1 & 0 & -\sin\theta_0 \\ 0 & 1 & 0 \\ 0 & 0 & \cos\theta_0 \end{bmatrix} \tag{5.24}
$$

where we defined $\mathbf{v} = \dot{\mathbf{p}}$. Once again, this linear system is unstable but controllable, therefore there exists a linear feedback law:

$$
v = l(x) = K_c x \tag{5.25}
$$

which stabilizes the linearized averaged system, where $x = (\Theta - \Theta_0, \dot{\Theta}, \overline{\mathbf{v}} - \mathbf{v}^*)$. Following the same reasoning as above, the following periodic feedback control:

$$
u = u(K_c x, t) = g_0(t) + G(t)K_c x = g_0(t) + \tilde{G}_c(t)x \tag{5.26}
$$

stabilizes the insect motion to a straight trajectory with constant velocity.

Steering

Designing feedback laws that generate steering behaviors can be done along the same lines as the design of stabilizing feedback laws for hovering and cruising. We start by considering

the (nonlinear) averaged system 5.19, we look for a feasible trajectory, then we linearize the system about that trajectory, and finally we design a stabilizing feedback law $v = K_s x$ for the linearized system. The substitution of the feedback law into the input control $u = u(K_s x, t) = g_0(t) + G(t)K_s x = g_0(t) + \tilde{G}_s(t)x$ gives rise to the desired controller for the original system.

Steering can be obtained through different maneuvers. For example, steering behaviors can be obtained by yawing while hovering, i.e. steering on the spot, or by performing a banking maneuver while translating, i.e. the insect orientation is rolled on the side of the desired steering. The banked steering would generate a lateral acceleration, that combined with the forward motion of the insect, would give rise to a saccade, much in the same way as airplanes. Both these two maneuvers are feasible for the averaged system; therefore, it is not difficult to stabilize the dynamics for these maneuvers. Other acrobatic maneuvers can be conceived to generate steering, such as the combination of a half killer loop together with a 180° roll rotation, but their analysis goes beyond the scope of this dissertation.

5.3 Wing Trajectory Tracking and Actuator control

The previous section described how to design wing trajectories that can generate desired mean forces and torque during a wingbeat period. However, the wing trajectory cannot be controlled directly, and appropriate input voltages to the thorax actuators must be devised to track the desired wing trajectory. As described in Section 3.3.3, the dynamics of the thorax-wing structure can be approximated as a stable two-degree of freedom second order linear system. Given a desired wing trajectory $(\phi^*(t), \varphi^*(t))$, we can calculate the corresponding steady-state input voltages $(V_1^*(t), V_2^*(t))$ by substitution :

$$\begin{bmatrix} V_1^*(t) \\ V_2^*(t) \end{bmatrix} = T_0^{-1}\left(M_0 \begin{bmatrix} \ddot{\phi}^*(t) \\ \ddot{\varphi}^*(t) \end{bmatrix} + B_0 \begin{bmatrix} \dot{\phi}^*(t) \\ \dot{\varphi}^*(t) \end{bmatrix} + K_0 \begin{bmatrix} \phi^*(t) \\ \varphi^*(t) \end{bmatrix} \right) \tag{5.27}$$

where $T_0, M_0, B_0, K_0 \in \mathbb{R}^{2\times 2}$ are constant matrices, and V_1, V_2 are the input voltages to the wing actuators. Let $V = (V_1^l, V_1^r, V_2^l, V_2^r)$ be the input voltages for the two wings, and $u = (\phi_r, \phi_l, \varphi_r, \varphi_l)$, then the wing-thorax dynamics for both wings can be rewritten in state space as follows:

$$\begin{bmatrix} \dot{u} \\ \ddot{u} \end{bmatrix} = \begin{bmatrix} 0 & I \\ -M^{-1}K & -M^{-1}B \end{bmatrix} \begin{bmatrix} u \\ \dot{u} \end{bmatrix} + \begin{bmatrix} 0 \\ M^{-1} \end{bmatrix} V \tag{5.28}$$

where the matrices M, B, K depend on T_0, M_0, B_0, K_0, and the dynamics is stable and controllable. Therefore, the total dynamics of the insect is given by Equations (5.1), (5.3) and (5.28). Following

the notation of Section 4.4, the dynamics of the insect given by Equations (5.1) corresponds to the slow dynamics, while the dynamics of the actuators given by Equation (5.28) corresponds to the fast dynamics.

In the previous section, we assumed that wings would follow the desired trajectories parameterized as:

$$u(v,t) \quad = \quad g_0(t) + G(t)v \tag{5.29}$$

where $g(t)$ and $G(t)$ are defined in Equation (5.14). If we substitute Equation (5.29) into Equation (5.28) we formally obtain:

$$V(v,t) \quad = \quad q(t) + Q(t)v \tag{5.30}$$
$$q(t) \quad = \quad M\ddot{g}(t) + B\dot{g}(t) + Kg(t)$$
$$Q(t) \quad = \quad M\ddot{G}(t) + B\dot{G}(t) + KG(t)$$

where $q(t)$ and $Q(t)$ are a T-periodic vector and matrix, respectively. Following the notation of Lemma 4.4.1 in Chapter 4, we have that for $g(v,t) = q(t) + Q(t)v$ the corresponding steady state solution of the fast system (5.28) is $u = h_T(v,t) = g(t) + G(t)v$, since $\frac{dh_T(v,t)}{dt} = q(t) + Q(t)v$. By construction, the mean vector field of the slow system $\bar{f}(x,v)$ defined as $\bar{f}(x,v) = \frac{1}{T} \int_0^T f(x, h_T(v,t))dt$, is exactly the same as given by Equations (5.17) and (5.1). Therefore, by Lemma 4.4.1, if we choose the same feedback laws $v = Kx$ obtained as described in Section 5.2, the insect dynamics including the actuators dynamics will be stabilized about the desired configuration or trajectory if the bandwidth of the actuators is sufficiently larger than the bandwidth of the insect closed loop dynamics. For example, if we want to stabilize hovering, we can use $v = l(x) = K_h x$ where the gain K_h is the same gain given by Equation (5.22), so that the overall control feedback is:

$$V = V(Kx,t) = q(t) + Q(t)K_h x = q(t) + \tilde{Q}(t)x \tag{5.31}$$

where $q(t)$ and $\tilde{Q}(t) = Q(t)K_h$ are T-periodic continuous functions.

It is very important to remark is that the above equation is the simplest feedback law possible, since it is a periodic affine feedback of the state, and does not require the computation of complex nonlinear functions. It is also very important to note that when designing the matrix K_h, the bandwidth of the linearized closed loop dynamics of the hovering $\dot{x} = \bar{f}(x, K_h x)$ must be chosen to be smaller than the bandwidth of the actuators, otherwise the assumption of separation of time scale is likely to fail and give rise to an unstable system. This last requirement can be enforced by appropriately choosing the weights for the LQR design of the feedback matrix gain K_h.

5.4   1-d.o.f. wing with PWM actuator control

In the previous section we considered a wing-thorax structure which allowed the direct control of two degrees of freedom: the stroke angle ϕ and the rotation angle φ. Moreover, we assumed that the voltage input could be controlled analogously, i.e. we did not impose any constraints on functions $h(t)$ and $H(t)$ besides input and rate limitations. Although these specifics are feasible for the target design of the MFI, we want to explore alternative structures that can simplify the overall design of the MFI from an electromechanical perspective.

First, we will consider a rigid wing where only the leading edge is actuated, and the trailing edge is free to rotate. When the leading edge is actuated to perform an oscillatory trajectory, the wing undergoes a passive rotation at the inversion of motion of the leading edge due to inertial and aerodynamic forces. If the wing mass is sufficiently small, the aerodynamic forces will tilt the wing such that the angle of attack could be much smaller than 45°. Therefore, if the wing angle of attack is mechanically limited to 45°, the wing will have a mean angle of attack of approximately 45° for most of the time, except at the inversion of motion. In order to simplify the analysis we assume that this rotation is instantaneous and the angle of attack is always set to 45°. Although this is a crude approximation, we believe that the qualitative results obtained while using this assumption will not be disrupted even when a more realistic model is adopted.

Second, we will consider only a pulse width modulation (PWM) scheme for the input voltage to the wing actuator, where only voltage offset, the voltage magnitude, and duty cycle can be controlled. This scheme is particularly suitable from a power electronic perspective, since it is easier to build and more compact than a fully analogical input voltage control. In order to simplify the analysis, we model the wing-thorax structure as a second order linear model.

In the next two subsections we show how controllability is still preserved and it is possible to design stabilizing feedback control laws in the same spirit as in the previous sections. In particular, in the next subsection we show how two wings with one active degree of freedom and passive rotation can still control independently 5 degrees of freedom. In the following subsection, we include the dynamics of the actuators driven by a PWM voltage input and show that controllability is preserved, once again.

5.4.1   Saw-tooth wing motion

As mentioned above, we assume that wing rotation is instantaneous at the wing's inversion of motion thus maintaining the same angle of attack during upstroke and downstroke, i.e. $\alpha(t) =$
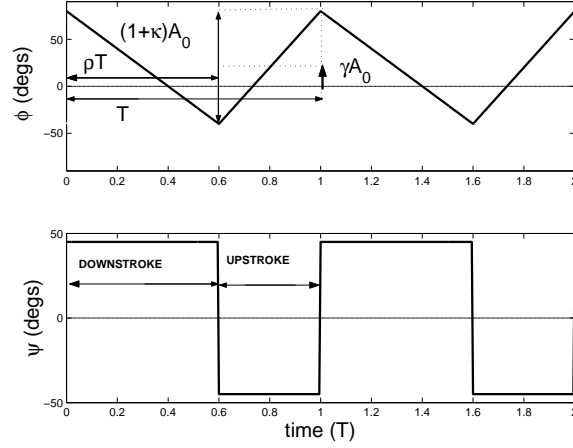
Figure 5.7: Wing kinematics during two wingbeat periods: (*top*) stroke angle, (*bottom*) rotation angle

45°. Also we assume that the wings move at constant angular velocity during the upstroke and the downstroke, i.e. the stroke angle $\phi(t)$ moves according to a sawtooth-like motion as shown in Figure 5.7. Mathematically, each wing trajectory within a single wingbeat is described by the following equations:

$$\phi(t) = \begin{cases} A_0(1+\kappa)\left(1 - \frac{2t}{\rho T}\right) + \gamma A_0 & 0 \leq t \leq \rho T \\ A_0(1+\kappa)\left(2\frac{t-\rho T}{(1-\rho)T} - 1\right) + \gamma A_0 & \rho T < t \leq T \end{cases}$$

$$\psi(t) = 45^o \, \text{sign}(\rho T - t) \qquad\qquad 0 \leq t \leq T \qquad (5.32)$$

where $\text{sign}(x) = \frac{x}{|x|}$, T is the wingbeat period, A_0 is the stroke amplitude range, κ is a tunable parameter that controls the stroke amplitude, ρ is the ratio of downstroke duration to total wingbeat period, and γ is the relative stroke angle offset. We assume that the wingbeat period, T, and the stroke amplitude range, A_0, are fixed, while the three dimensionless parameters (κ, ρ, γ) can be changed on a wingbeat-by-wingbeat basis. The angle of attack is fixed at 45°, because it is the angle that generates maximum vertical thrust.

To further simplify the mathematical analysis, we consider only the delayed stall aerodynamic forces perpendicular to the wing surface given by Equation (3.6), which we report here for ease of consultation:

$$F_{tr,N} = \frac{1}{2}\rho_a C \sin(\alpha) A_w \hat{r}_2^2 R^2 \dot{\phi}^2 \qquad (5.33)$$

where $C = 3.5$ is the delayed stall force coefficient, α is the angle of attack, A_w is the total wing area, ρ_a is the air density, $\hat{r}_2$ is the normalized center of pressure, and R is the wing length. The lift

and drag components of this force can be obtained by using Equation (3.11)-(3.12) to get:

$$F_D = -\frac{1}{4}\rho_a C A_w \hat{r}_2^2 R^2 |\dot{\phi}|\dot{\phi} = -A |\dot{\phi}|\dot{\phi} \tag{5.34}$$

$$F_L = \frac{1}{4}\rho_a C A_w \hat{r}_2^2 R^2 \dot{\phi}^2 = A \dot{\phi}^2 \tag{5.35}$$

where we used the fact $\alpha = 45^o$, and the fact that the drag force is always in the opposite direction of the wing velocity. Substituting the equations above into Equation (3.16)-(3.17) we get:

$$f_a^b(u) = A \begin{bmatrix} -|\dot{\phi}_l|\dot{\phi}_l \cos\phi_l - |\dot{\phi}_r|\dot{\phi}_r \cos\phi_l \\ |\dot{\phi}_l|\dot{\phi}_l \sin\phi_l - |\dot{\phi}_r|\dot{\phi}_r \sin\phi_l \\ \dot{\phi}_l^2 + \dot{\phi}_r^2 \end{bmatrix} \tag{5.36}$$

$$\tau_a^b(u) = A\hat{r}_2 R \begin{bmatrix} \dot{\phi}_l^2 \cos\phi_l - \dot{\phi}_r^2 \cos\phi_r \\ -\dot{\phi}_l^2 \sin\phi_l - \dot{\phi}_r^2 \sin\phi_r \\ |\dot{\phi}_l|\dot{\phi}_l - |\dot{\phi}_r|\dot{\phi}_r \end{bmatrix} \tag{5.37}$$

where $u = (\phi_l, \phi_r)$ is the input vector. We assume that the stroke plane frame and the body frame coincide, i.e. the aerodynamic forces and torque acting on the center of mass are given by the equations above.

Following the notation developed in the previous chapter, the input vector $u = (\phi_l, \phi_r)$ is parameterized as $u = g(v,t)$, where $v = (\rho_l, \rho_r, \kappa_l, \kappa_r, \gamma_l, \gamma_r)$ is the kinematic parameter vector or simply virtual input, and the function $g(v,t)$ is given by Equation (5.32). The aerodynamic forces and torques are thus periodic functions parameterized by v, i.e. $f_a^b = f_a^b(u) = f_a^b(t,v)$ and $\tau_a^b = \tau_a^b(u) = \tau_a^b(t,v)$ obtained by substituting Equations (5.32) into Equations (5.36)-(5.37).

As in the previous sections, we consider now the mean aerodynamic force, $\bar{f}_a^b(v) = \frac{1}{T}\int_0^T f^b(t)dt$, and torque, $\bar{\tau}_a^b(v) = \frac{1}{T}\int_0^T \tau^b(t)dt$, that can be computed analytically after some tedious but straightforward calculations as follows:

$$\bar{f}_a^b(v) = \frac{4FA_0^2}{T^2} \begin{bmatrix} \frac{\text{sinc}(\frac{A_0}{4})\cos(\gamma_l A_0)(1+\kappa_l)^2(1-2\rho_l)}{\rho_l(1-\rho_l)} + \frac{\text{sinc}(\frac{A_0}{4})\cos(\gamma_r A_0)(1+\kappa_r)^2(1-2\rho_r)}{\rho_r(1-\rho_r)} \\ -\frac{\text{sinc}(\frac{A_0}{4})\sin(\gamma_l A_0)(1+\kappa_l)^2(1-2\rho_l)}{\rho_l(1-\rho_l)} + \frac{\text{sinc}(\frac{A_0}{4})\sin(\gamma_r A_0)(1+\kappa_r)^2(1-2\rho_r)}{\rho_r(1-\rho_r)} \\ \frac{(1+\kappa_l)^2}{\rho_l(1-\rho_l)} + \frac{(1+\kappa_r)^2}{\rho_r(1-\rho_r)} \end{bmatrix} \tag{5.38}$$

$$\bar{\tau}_a^b(v) = \frac{4FLA_0^3}{T^2} \begin{bmatrix} -\frac{\text{sinc}(\frac{A_0}{4})\cos(\gamma_l A_0)(1+\kappa_l)^2}{\rho_l(1-\rho_l)} + \frac{\text{sinc}(\frac{A_0}{4})\cos(\gamma_r A_0)(1+\kappa_r)^2}{\rho_r(1-\rho_r)} \\ -\frac{2\text{sinc}(\frac{A_0}{4})\sin(\gamma_l A_0)(1+\kappa_l)^2}{A_0\rho_l(1-\rho_l)} - \frac{2\text{sinc}(\frac{A_0}{4})\sin(\gamma_r A_0)(1+\kappa_r)^2}{A_0\rho_r(1-\rho_r)} \\ -\frac{(1+\kappa_l)^2(1-2\rho_l)}{\rho_l(1-\rho_l)} + \frac{(1+\kappa_r)^2(1-2\rho_r)}{\rho_r(1-\rho_r)} \end{bmatrix} \tag{5.39}$$

where $\text{sinc}(x) = \frac{\sin x}{x}$. The equations above can be linearized about the symmetric wing motions corresponding to $v_0 = (\rho_l, \rho_r, \kappa_l, \kappa_r, \gamma_l, \gamma_r) = (\frac{1}{2}, \frac{1}{2}, 0, 0, 0, 0)$ to give:

$$
\begin{bmatrix} \bar{f}_a^b(v) \\ \bar{\tau}_a^b(v) \end{bmatrix} = \begin{bmatrix} \bar{f}_a^b(v_0) \\ \bar{\tau}_a^b(v_0) \end{bmatrix} + \begin{bmatrix} \frac{\partial \bar{f}_a^b(v_0)}{\partial v} \\ \frac{\partial \bar{\tau}_a^b(v_0)}{\partial v} \end{bmatrix} (v - v_0) + o(\|v - v_0\|) \tag{5.40}
$$

$$
= \begin{bmatrix} 0 \\ 0 \\ f_0 \\ 0 \\ 0 \\ 0 \end{bmatrix} + \begin{bmatrix} -af_0 & -af_0 & 0 & 0 & 0 & 0 \\ 0 & 0 & 0 & 0 & 0 & 0 \\ 0 & 0 & f_0 & f_0 & 0 & 0 \\ 0 & 0 & -a\tau_0 & a\tau_0 & 0 & 0 \\ 0 & 0 & 0 & 0 & -a\tau_0 & -a\tau_0 \\ \tau_0 & -\tau_0 & 0 & 0 & 0 & 0 \end{bmatrix} \begin{bmatrix} \rho_l - \frac{1}{2} \\ \rho_r - \frac{1}{2} \\ \kappa_l \\ \kappa_r \\ \gamma_l \\ \gamma_r \end{bmatrix} \tag{5.41}
$$

where $a = \text{sinc}(\frac{A_0}{4})$, $f_0 = \frac{32AA_0^2}{T^2}$, and $\tau_0 = \frac{32AR\hat{r}_2 A_0^3}{T^2}$.

To further simplify results, consider the following input parameter:

$$
\begin{aligned}
w_1 &= -\text{sinc}(\tfrac{A_0}{4})[(\rho_l - \tfrac{1}{2}) + (\rho_r - \tfrac{1}{2})] \\
w_2 &= \kappa_l + \kappa_r \\
w_3 &= -\text{sinc}(\tfrac{A_0}{4})[\kappa_l - \kappa_r] \\
w_4 &= -\text{sinc}(\tfrac{A_0}{4})[\gamma_l + \gamma_r] \\
w_5 &= (\rho_l - \tfrac{1}{2}) - (\rho_r - \tfrac{1}{2})
\end{aligned} \tag{5.42}
$$

to obtain:

$$
f_a^b(w) = f_0 \begin{bmatrix} 0 \\ 0 \\ 1 \end{bmatrix} + f_0 \begin{bmatrix} w_1 \\ 0 \\ w_2 \end{bmatrix} \tag{5.43}
$$

$$
\bar{\tau}_a^b(w) = \tau_0 \begin{bmatrix} w_3 \\ w_4 \\ w_5 \end{bmatrix} \tag{5.44}
$$

Note that the mean stroke amplitude A_0 and wingbeat period T can be chosen to exactly balance the gravity force mg, i.e. $f_0 = mg$. The linearized wrench clearly shows how the kinematic parameters can be combined to control *independently* all the forces and torques about the insect center of mass, except for the force component along the y-direction of the body frame. In particular, a difference in amplitude in the two wings would result in a net roll torque and the increase in amplitude of both wings would result in a larger vertical thrust. A difference in speed between downstroke and upstroke on both wings simultaneously leads to a net forward thrust, while a difference in speed

between the two wings leads to a net yaw torque. Finally, an analogous change in the offset of stroke motion on both wings gives rise to a net pitch torque. Equation (5.42) can be thought as a linear map $B \in \mathbb{R}^{5\times6}$ from the wing kinematic parameters, $\nu = (\rho_l, \kappa_l, \gamma_l, \rho_r, \kappa_r, \gamma_r)$, to the virtual control inputs $w = (w_1, w_2, w_3, w_4, w_5)$, i.e. $w = B\nu$. Although the map B is not invertible since it is not a square matrix, it is always possible to find a linear map $B^\dagger \in \mathbb{R}^{6\times5}$ such that, for any vector w the vector $\nu = B^\dagger w$ and satisfies $w = BB^\dagger w$, i.e. $BB^\dagger = I_{5\times5}$. One natural choice is to use the pseudoinverse of the matrix B, i.e. $B^\dagger = (B^T B)^{-1} B^T$. It is clear that the wing kinematic parametrization chosen in Equations (5.32) is sufficient to move the insect in any direction, since it is possible to synthesize feedback laws based on the parameter vector v and the map given by Equation (5.40) in the same way as explained in the previous sections, where we just need to substitute the map given by Equation (5.17) with map given by Equation (5.40).

5.4.2 Attitude stabilization with PWM actuator control

A simplified model of the actuator-thorax-wing system is considered here. As shown in [70], the piezoelectric actuator can be seen as a pure force generator with a parallel stiffness, where the output force is proportional to the input voltage $V(t)$. The thorax, which basically consists of a 4-bar mechanism, is deployed to transform the force/linear displacement at the tip of the actuator into torque/angular displacement at the base of the wing, as explained in Section 3.3.3. The wing will contribute to the dynamics with its rotary inertia and its aerodynamic damping. In order to elicit the principal features of flapping flight, a simplified electromechanical model will be used. A detailed model for a 2 degree of freedom (d.o.f.) thorax-wing can be found in [4], while here only 1 d.o.f. will be considered, as the one sketched in Figure 5.8, where the rotation along the wing axis is passive, i.e. the trailing edge of the wing simply follows the leading edge (see Figure 5.1). With reference to Figure 5.8, the thorax transmission will be modelled as a static linear relation, i.e. nonlinearities at high fields will be neglected, and the aerodynamic damping will be considered as a linear function of the wing speed, although a more faithful model should consider a quadratic dependence on the wing speed as suggested by Equation (5.33). In [70] is shown how to relate geometrical and physical characteristics of the actuator-thorax-wing system to the parameters that characterize a second order system, i.e. DC gain K, resonant frequency ω_0, and quality factor Q. The actual values for these parameters have been chosen based on those experimentally observed in blowflies, the target size of the MFI [82]. In fact, the actuator stiffness is tuned with wing inertia and the thorax transmission ratio in order to resonate at $150Hz$, i.e. $\omega_0 = 2\pi150\ rad/sec$, while the
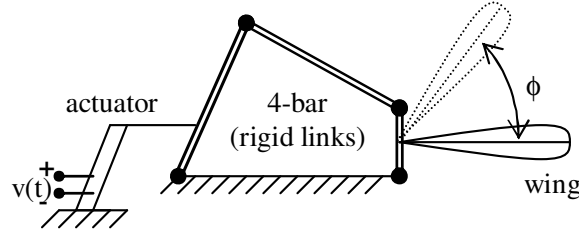
Figure 5.8: Actuator, 4-bar, wing system.

quality factor is typically $Q = 3$, as shown in [70] [4].

Let $V(t)$, $\phi(t)$ and $\dot{\phi}(t)$ be respectively the input voltage, the output wing displacement and the output wing speed and $\mathcal{V}$, Φ, and $\dot{\Phi}$ be their Laplace transforms. The dynamics of the second order system in the time domain are determined by:

$$\begin{bmatrix} \dot{\phi}(t) \\ \ddot{\phi}(t) \end{bmatrix} = \begin{bmatrix} 0 & 1 \\ -\omega_0^2 & -\frac{\omega_0}{Q} \end{bmatrix} \begin{bmatrix} \phi(t) \\ \dot{\phi}(t) \end{bmatrix} + \begin{bmatrix} 0 \\ K \end{bmatrix} V(t) \tag{5.45}$$

while in the Laplace domain it can be expressed as:

$$\begin{bmatrix} \Phi \\ \dot{\Phi} \end{bmatrix} = \frac{K\,\omega_0^2}{s^2 + \frac{\omega_0}{Q}s + \omega_0^2} \begin{bmatrix} 1 \\ s \end{bmatrix} \mathcal{V} = \begin{bmatrix} F(s) \\ \dot{F}(s) \end{bmatrix} \mathcal{V} \tag{5.46}$$

In a previous section, forces and torque were derived after parameterizing wing kinematics with input parameters (κ, ρ, γ). Here the motion of the wings is determined by the wing-thorax electromechanical system driven by a piezoelectric actuator. A piezoelectric actuator is capable of transforming an input voltage into an output mechanical displacement. Its parasitic capacitance mainly affects the efficiency of such a conversion [14]. Due to energy/size constraints [70], a binary input voltage ($\pm V_a$), i.e. a switching stage, with possibly a voltage offset V_{off} will be employed. It is important to limit the number of switches per cycle because each switch leads to unavoidable losses [14], and, for this reason, only square waves with variable duty cycle will be considered. Therefore, a PWM will be employed and the input parameters will be related to the input voltage $V(t)$, i.e. its amplitude V_a, its offset V_{off} and its duty cycle d, as follows:

$$V(t) = V_a\,\mathrm{sign}(dT - t) + V_{off} \qquad 0 \le t \le T \tag{5.47}$$

where $T = \frac{2\pi}{\omega_0}$. In order to simplify the notation we rewrite the equation above as follows:

$$V(t) = V_0(1 + \nu)\,\mathrm{sign}(dT - t) + V_0\delta \qquad 0 \le t \le T \tag{5.48}$$

	$g(v,t)$	$h(v,t)$	$\dot{h}(v,t)$
a_{DC}	$V_a(2d-1)+V_{off}$	$K(V_a(2d-1)+V_{off})$	0
$\lvert a_n \rvert$	$4\frac{\sin(\pi dn)}{\pi n}$	$4\frac{\sin(\pi dn)}{\pi n}\lvert F(n\,j\omega_0)\rvert$	$4\frac{\omega_0\sin(\pi dn)}{\pi n}\lvert F(n\,j\omega_0)\rvert$
$\angle a_n$	$-\pi dn$	$-\pi dn + \angle F(n\,j\omega_0)$	$-\pi dn + \angle F(n\,j\omega_0) + \frac{\pi}{2}$

Table 5.1: Fourier coefficients for $v(t)$, $\phi(t)$, and $\dot{\phi}(t)$.

where the voltage amplitude V_0 is constant, and the new parameters (v,d,δ) play the role of (κ,ρ,γ) in the previous section. Let us define the input parameter vector $v \overset{\Delta}{=} (v,d,\delta)$. For each choice of the the input parameter vector, the input voltages to the wing actuators $V(t) = g(v,t)$, given by Equation (5.48) are T-periodic functions. Since system (5.45) is a linear stable system, then the steady state solution to the input voltage $V(t) = g(v,t)$ is a periodic T-periodic function $\phi_v(t) = h_T(v,t)$ parameterized by the parameter vector v. The function $h_T(v,t)$, which is the steady state solution of system (5.45) subject to periodic input (5.48), can be obtained using Fourier series. A generic periodic function $w(t)$ can be written as:

$$w(t) = a_{DC} + \sum_{n=1}^{\infty} \lvert a_n \rvert \cos(n\omega_0 t + \angle a_n) \tag{5.49}$$

where ω_0 is the input frequency, a_{DC} is the DC component of $w(t)$, a_n (generally a complex number) is the Fourier coefficient, and $\lvert a_n \rvert$ and $\angle a_n$ represent its modulus and phase, respectively. The output $y(t)$ of a linear system with transfer function $F(s)$ in the Laplace domain subject to a periodic input $w(t)$ is given by:

$$y(t) = a_{DC}F(0) + \sum_{n=1}^{\infty} \lvert a_n \rvert \lvert F(jn\omega_0)\rvert \cos(n\omega_0 t + \angle a_n + \angle F(jn\omega_0)) \tag{5.50}$$

Therefore the steady state solution $h(v,t)$ and its derivative $\dot{h}(v,t)$ can be written in Fourier series analogous to Equation (5.49), whose coefficients are given in Table 5.1, as follows:

$$h(v,t) = K(V_a(2d-1)+V_{off}) + \sum_{n=1}^{\infty} 4V_a\frac{\sin(\pi dn)}{\pi n}\lvert F(n\,j\omega_0)\rvert \cos\left(n\omega_0 t - \pi dn + \angle F(jn\omega_0)\right) \tag{5.51}$$

where F is the transfer function given by Equation (5.46).

Following the same notation as in Lemma 4.4.1, with a little abuse of notation we redefine the input parameter vector $v \overset{\Delta}{=} (d_l, d_r, v_l, v_r, \delta_l, \delta_r)$ for both wings, the input voltage vector as $V = (V_l, V_r) = g(v,t)$ given by Equation (5.48), and the corresponding steady state solution $u_h(t) = (\phi_l, \phi_r) = h(v,t)$ given by Equation (5.51), where the subscripts l, r stand for left and right wing, respectively. Then we compute the mean vector field of the insect dynamics corresponding to

the steady state solution $u_h = h_T(v,t)$. This is equivalent to computing the mean wrench obtained by substituting the steady state solution $u_h = h(v,t)$ into Equations (5.36)-(5.37), and then taking the average as in Equations (5.38)-(5.39). Unfortunately, it is not possible to derive a closed form solution for the average wrench $\bar{w}(v) = (\bar{f}^b_a(v), \bar{\tau}^b_a(v))$ or for its linearization. Therefore, we will resort to an empirical linearization similarly to that adopted in the map given by Equation (5.17); we generate a random set of parameter vectors $\{v_n\}$ centered about the linearization input vector $v_0 = (\frac{1}{2}, \frac{1}{2}, 0, 0, 0, 0)$ and we compute the corresponding mean wrench $\{\bar{w}(v_n)\}$ via simulations. Then we look for a first order approximation map $\hat{w}(v) = w_0 + W(v - v_0)$, where the vector w_0 and the matrix W are derived via least squares (LS) applied to the set of empirically derived pairs $\{v_n, \bar{w}(v_n)\}$. The empirical map obtained by choosing target parameters for the MFI, i.e. resonant frequency $\omega_0 = 2\pi 150\ rad/sec$, quality factor $Q = 3$, and voltage amplitude V_0 necessary to generate a stroke amplitude of 120°, is the following:

$$
\begin{bmatrix} \hat{f}^b_a(v) \\ \hat{\tau}^b_a(v) \end{bmatrix} = w_0 + W(v - v_0)
$$

$$
= \begin{bmatrix} 0 \\ 0 \\ f_0 \\ 0 \\ 0 \\ 0 \end{bmatrix} + \begin{bmatrix} -0.1f_0 & -0.1f_0 & 0 & 0 & 0 & 0 \\ 0 & 0 & 0 & 0 & 0 & 0 \\ 0 & 0 & f_0 & f_0 & 0 & 0 \\ 0 & 0 & -\tau_0 & \tau_0 & 0 & 0 \\ -0.3\tau_0 & -0.3\tau_0 & 0 & 0 & -0.3\tau_0 & -0.3\tau_0 \\ -0.15\tau_0 & 0.15\tau_0 & 0 & 0 & 0 & 0 \end{bmatrix} \begin{bmatrix} d_l - \frac{1}{2} \\ d - \frac{1}{2} \\ v_l \\ v_r \\ \delta_l \\ \delta_r \end{bmatrix} \quad (5.52)
$$

where $f_0 = mg$, and $\tau_0 = mg\hat{r}_2 R$, and the zero entries correspond to estimated values that are much smaller than the values of the largest entries in the same row. The random set for the LS is obtained by uniformly selecting random parameters in the set $||v - v_0||_\infty \le 0.2$ to avoid nonlinearities or unfeasible wing trajectories. The validity of a linear approximation of the mean wrench is illustrated in Figure 5.9 where the predicted mean wrench $\hat{w}$ (x-axes) given by map (5.52) is compared with the exact mean wrench obtained via simulations by randomly selecting 200 points in the set $||v - v_0||_\infty \le 0.2$.

The map given by Equation (5.52) is very similar to the map given by Equation (5.43), but there are important differences. The most important is that the mean force along the x-direction, $\bar{f}_x$, and the mean yaw torque, $\bar{\tau}_z$, are controllable in both maps by changing the duty cycle ρ or d appropriately, but the coefficients in map (5.52) are almost an order of magnitude smaller, since the coefficient a in map (5.43) is typically around $a \simeq 0.9$. Therefore, from a practical point of view, it is much harder to generate large forces along the x-direction or large yaw moments. This is the price to pay when considering only a wing with a single degree of freedom, in fact a large yaw torque
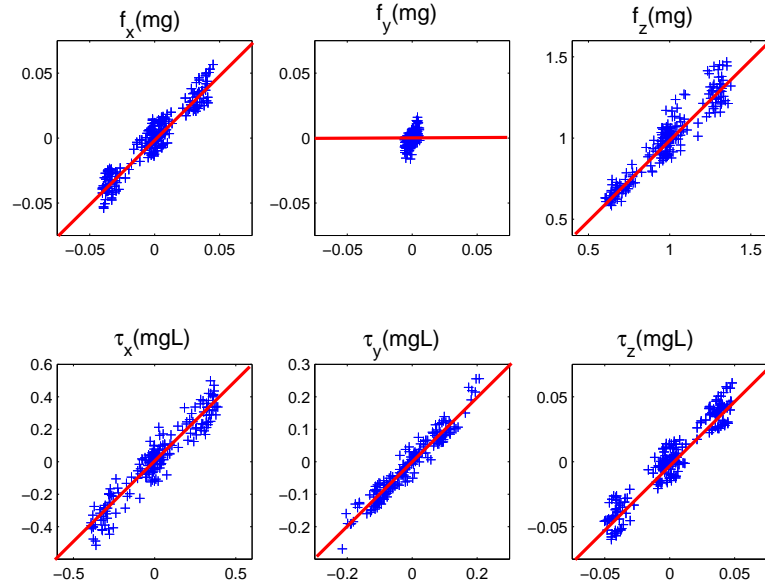
Figure 5.9: Simulations of exact mean wrench $\bar{w}$ (y-axes) versus the predicted mean wrench $\hat{w}$ (x-axes) given by map (5.52). The solid lines correspond to the ideal case when predicted mean wrench and exact mean wrench would coincide. Units in the plots are normalized to $f_0 = mg$ for the forces and to $\tau_0 = mg\hat{r}_2R$ for the torques.

or forward thrust could be obtained easily by changing the angle of attack, as shown in map (5.17) where it is possible to generate comparable torques or forces along any axis, except for the force along the y-axis.

The second difference is that the pitch torque $\bar{\tau}_y$ is affected by both the duty cycle d and the voltage offset δV_0. This is to be expected since they both affect the offset of the stroke angle, $\Phi_{off} = K(V_a(2d-1) + \delta V_0)$ as shown in Equation (5.51), and the offset of stroke angle is the parameter that mostly affects the pitch torque generation by shifting the center of pressure of the aerodynamic forces forward or backward from the center of mass.

Since the mean wrench map shows the possibility of independently controlling the three torques and the force components along the x and z-axes, it is possible to design a feedback law

$$v = Kx \tag{5.53}$$

that stabilizes the flight dynamics following the same lines of Section 5.2, where we just need to substitute the mean wrench map given by Equation (5.17) with the map given by Equation (5.52). According to Lemma 4.4.1, the closed loop system given by Equations (5.1),(5.36)-(5.37), (5.45), (5.48), and (5.53) is stable if the dynamics of the slow system, i.e. the flight dynamics of Equation

(5.1) of the closed loop averaged system, is considerably slower than the dynamics of the fast systems, i.e. the actuator dynamics given by Equation (5.45). The bandwidth of the slow system is determined by the feedback law (5.53), since it determines the bandwidth of the insect dynamics of the averaged system, therefore it is necessary to set some bandwidth constraints during the design process. In Example 6 in Chapter 4, we explored the effect of the mechanical parameters Q and ω_0 in the dynamics of the overall system. We showed how they both need to be sufficiently large to apply averaging and separation of timescales arguments. As a rule of thumb, the bandwidth of the slow system must be at least a few times smaller than the bandwidth of the fast system and the frequency of the forcing periodic signal. For a value of the quality factor $Q = 2$ to 4, the bandwidth of the actuators is approximately the same as its resonant frequency, therefore when designing the feedback law (5.53), we need to set the bandwidth of the closed loop dynamics to be a few times smaller than the wingbeat frequency. This simple rule of thumb seems to be confirmed by several species of insects of different sizes and wingbeat frequency which require several wingbeats to complete a full maneuver such as a saccade. In particular, the highly maneuverable fruit flies complete a 90° saccade in about 10 wingbeats [31], houseflies in about 20 wingbeats [81], and tsetse flies complete a 180° saccade in about 20 wingbeats [10].

5.5 Conclusions

In this chapter, insect flight has been analyzed and studied from a mathematical perspective. In this context, flapping flight belongs to the group of underactuated systems, i.e. systems where the number of inputs is smaller than the number of degrees of freedom, yet where any desired configuration can be reached. Specifically, in the case of insect flight the inputs are the trajectories of the wings, and the degrees of freedom are the position and the orientation of the insect body in the environment. We showed how averaging and separations of timescales tools developed in chapter 4 can be applied to design stabilizing feedback control laws for different flight modes such as hovering and cruising. The key idea in designing stabilizing controllers was to parameterize the wing trajectories such that the mean torque and forces could be controlled independently. The process of designing suitable parametrization of wing trajectories such that the mean torques and forces have a simple dependence on the parameters is a formidable task. There is a vast literature on the synthesis of periodic feedbacks that artificially increases the number of inputs and that allow simple design of stabilizing laws, based on the particular mechanical structure of the dynamics of the system, see for example [9], [80], [13] and the references in the introduction to this thesis. However, these tools

cannot be applied directly to insect flight since aerodynamic forces are complex functions of the angles and velocity of the wings. Instead of trying to synthesize the parametrization of the wings starting directly from the dynamics, we adopted a biomimetic approach, i.e. motions of wings were parameterized based on observations of insect wing motions during free flight maneuvers as described in Section 2.4. Such parametrization allows direct control of the three mean aerodynamic torques and the x and z components of the mean aerodynamic force as shown by the map 5.17, thus confirming the hypothesis of many biologists that insect can control five degree of freedom independently [77].

Another advantage of this approach is that the mean wrench map has been obtained via simulations, but it could also be computed using experimental data if available. This means that the methodology developed in this chapter is not critically bound to the aerodynamic model presented in Section 3.3.1, and it is likely to very effective in a realistic setting.

We also extended the controller design to include the dynamics of the actuators, based on the separation of timescales. Formally, the controller design procedure does not change, but it relies on the implicit assumption that the dynamics of the actuators is faster than the dynamics of the insect body, therefore a constraint on the bandwidth of the closed loop dynamics of body must be imposed. One of the most important features of the final feedback structure is that the voltage input is simply a linear, periodic, proportional feedback of the insect dynamics as given by Equation (5.31). This is very important from a technological point of view, since it is sufficient to compute off-line the vector $q(t)$ and the matrix $\tilde{Q}(t)$, and then store them onboard the MFI. The output to the actuators will be computed by multiplying on-line the sensor measurements by the functions $q(t)$ and $\tilde{Q}(t)$.

Finally, we explore the consequences of considering a simpler electromechanical structure where the rotation of the wing is passive, and the actuators are controlled via PWM voltage input. Despite the simpler structure, controllability of the 5 degrees of freedom is still preserved, however the authority of the controller decreases, i.e. the torque and force generation mechanisms are smaller in magnitude than the equivalent ones in the case of a two degree of freedom wing with analog voltage input control. This simplified architecture is promising from a technological point of view since it is easier to fabricate and implement; however, further analysis including experimental data are necessary before we can draw a definite conclusion.

Chapter 6

Conclusions

In this dissertation, flapping flight as an effective form of locomotion for robotic insects was analyzed rigorously. The most important contribution of this dissertation is to show how the application of averaging theory and biomimetic principles to both the wing trajectory parametrization and the complex time-varying dynamics of the insect body simplifies the analysis of flapping flight which is then amenable to standard control theory. This methodology confirms the intuition of many biologists that insects can independently control five degrees of freedom out of the six degrees of freedom.

Compared to helicopter flight, flapping flight has two major advantages. The first is that, unlike in helicopter flight, flapping flight allows the control of horizontal thrust generation to be independent of than of pitch, and thus provides greater maneuverability during hovering as well as faster forward acceleration. The second is the production of large torque of up to $10 - 20\%$ of the weight of the insect times their wing length. This torque is larger than those produced by helicopters in relative terms, thus giving rise to larger angular accelerations.

Another interesting result of this dissertation is that the final feedback control for the stabilization of several flight modes such as hovering, cruising and steering, can be achieved with a simple proportional T-periodic feedback, where T is the wingbeat period. This holds true even when the actuators dynamics are included, under the assumption that their dynamics can be approximated by a linear stable system. The input voltages to the actuators, given by Equation (5.31), can be interpreted as the linear sum of periodic functions whose magnitude depends on the sensor measurements. These functions can be computed off-line and stored onboard the MFI. From a computational point of view, a T-periodic feedback gain is very attractive since it is equivalent to a static gain. In fact, it simply requires the computation of a few multiplications and additions of

the sensor measurements, besides a slightly larger memory to store the periodic functions. Memory is not a major concern for the limited resources of the MFIs, however, computational complexity is, since wings actuators need to be controlled faster than a wingbeat-by-wingbeat basis. A more complicated control scheme involving complex algebraic computations or nonlinear gains would be useless from a practical point of view.

The results in this dissertation are based on a mathematical model for the aerodynamic forces that do not include the wake capture. This might place some concerns about the validity of the results obtained. However, the controller design methodology developed can be adapted to include experimental data that does include wake capture. The only difference would appear in the estimation of the mean wrench map given by Equation (5.17), where the mean forces and torques computed using simulations must be substituted with the mean forces and torques measured with a force platform that are generated, for example, by a dynamically scaled model of a wing or a MFI prototype. The proposed approach would still work as long as the map could be approximated by a similar linear map. This will likely be the case even when including the wake capture, since the parametrization given by Equations (5.14) is based on biomimetic principles, i.e. it gives rise to wing trajectories that are observed in real insects during free flight. Therefore, there is no reason to think that the wake capture would destroy controllability of flight.

Finally, a simpler electromechanical design with a single active degree of freedom and passive rotation, and PWM actuator control was considered. It was shown that controllability of 5 degrees of freedom for the body dynamics is preserved, but the maximum magnitude of the forces and torques that can be generated are smaller than the more sophisticated design. Although experimental results are necessary to validate these theoretical results, this simpler electromechanical design could be viable alternative to the more complex one.

6.1 Future Directions

To the author's knowledge, this thesis is one of the first attempts to study flapping flight from a control theory perspective, and it is therefore far from being complete and exclusive. Several directions can be pursued.

Optimal wing trajectory parametrization. The parameterizations proposed in this dissertation are based on biomimetic principles, which means that they are based on calculated guesses. Although they were shown to be quite effective, this is an unsatisfactory approach from a theoretical

perspective. Besides, insects can and do change other kinematic parameters than those considered in this work. Therefore, a more systematic methodology to optimize the wing trajectory with respect to some metrics, such as aerodynamic power or torque magnitude, is sought.

Actuator control for trajectory tracking.   One of the major assumptions about the actuator dynamics was linearity, so that wing trajectory tracking could be easily solved using a pseudo-inverse to compute the control input for the actuators. This is true only to first order, as shown in [3] and [4], since nonlinearities become important particularly when aggressive maneuvers and rapid wing rotations at the end of the half-strokes are necessary. Novel approaches need to be considered in this scenario.

Sensory system and navigation.   In this work the sensory information processing for stabilization purposes and navigation for MFIs was not considered, other than the sensory and neuromotor architecture adopted as a model for the design of the control unit. Some work in respect to output feedback for attitude stabilization has been given in [67], but many open questions remain about insect sensor-based navigation.

Control of underactuated nonlinear systems.   Flapping flight is a compelling example of an application of high-frequency control of an underactuated system in the biological realm. In this thesis, specific tools were developed to analyze flapping flight. However, flapping flight shares many similarities with fish locomotion, which has been shown to be amenable to being analyzed using geometric control theory and averaging [50] [47] [80]. A similar approach is likely to be applicable to flapping flight.

Limits of performance of biomimetic locomotion.   Biologically inspired locomotion is thought to have several advantages in many regards with respect to today's manmade vehicles: more silent and power efficient (fish locomotion), more versatile to heterogeneous terrains (hexapod locomotion), and more maneuverable (insect). In this dissertation, it has been shown that there is a tradeoff between input efficiency and responsiveness of the system and how this is related to some mechanical parameter such as the quality factor. A quality factor of about $2-3$ observed in many animals could be related to some trade-offs between mechanical efficiency, responsiveness to external disturbances, stability, and maneuverability. Similar trade-offs have been observed in legged insects [32], but little is available about similar considerations for flying insects. A deeper understanding

of these trade-offs from a control perspective can help the design of better biomimetic vehicles.

Bibliography

[1] R. Abraham and J.E. Marsden. *Foundations of Mechanics*. Addison-Wesley, 1978.

[2] T.M. Apostol. *Mathematical Analysis*. Addison-Wesley, 1957.

[3] S. Avadhanula. The design and fabrication of the MFI thorax based on optimal dynamics. Master's thesis, University of California at Berkeley, 2001.

[4] S. Avadhanula, R.J. Wood, D. Campolo, and R.S. Fearing. Dynamically tuned design of the MFI thorax. In *Proc of the IEEE International Conference on Robotics and Automation*, Washington, DC, May 2002.

[5] J. Baillieul. *Mathematical Control Theory*, chapter The geometry of controlled mechanical systems, pages 322–354. Springer-Verlag, 1998.

[6] J.M. Birch and M.H. Dickinson. Spanwise flow and the attachment of the leading-edge vortex on insect wings. *Nature*, 412(6848):729–733, 2001.

[7] J.M. Birch and M.H. Dickinson. The influence of wing wake interactions on the production of aerodynamic forces in flapping flight. *Journal of Experimental Biology*, 206, 2003.

[8] A. M. Bloch, P. S. Krishnaprasad, J. E. Marsden, and R. M. Murray. Nonholonomic mechanical systems with symmetry. *Archives for Rational Mechanics and Analysis*, 136:21–99, 1996.

[9] A.M. Bloch. *Nonholonomic Mechanics and Control*. Interdisciplinary Applied Mathematics. Springer-Verlag, 2003.

[10] J. Brady. Flying mate detection and chasing by tsetse flies (*Glossina*). *Physiol. Ent.*, 16:153–161, 1991.

[11] R. Brockett. On the rectification of vibratory motion. *SIAM Journal of Control and Optimization*, 20:91–96, 1989.

[12] R.W. Brockett. Asymptotic stability and feedback stabilization. *Differential Geometric Control Theory*, pages 181–191, 1993.

[13] F. Bullo. Averaging and vibrational control of mechanical systems. *SIAM Journal of Control and Optimization*, 41(2):542–562, 2002.

[14] D. Campolo, M. Sitti, and R.S. Fearing. Efficient charge recovery method for driving piezo-electric actuators with quasi-square waves. *IEEE Transaction on Ultrasonics, Ferroelectrics, and Frequency Control*, to appear 2003.

[15] W.P. Chan, F. Prete, and M.H. Dickinson. Visual input to the efferent control system of a fly's "gyroscope". *Science*, 280(5361):289–292, 1998.

[16] X. Deng, L. Schenato, and S. Sastry. Attitude control for a micromechanical flying insect including thorax and sensor models. In *Proc. of the IEEE International Conference on Robotics and Automation*, Taipei, Taiwan, May 2003.

[17] M.H. Dickinson. Linear and nonlinear encoding properties of an identified mechanoreceptor on the fly wing measured with mechanical noise stimuli. *Journal of Experimental Biology*, 151:219–244, 1990.

[18] M.H. Dickinson. Directional sensitivity and mechanical coupling dynamics of campaniform sensilla during chordwise deformations of the fly wing. *Journal of Experimental Biology*, 169:221–233, 1992.

[19] M.H. Dickinson. The effects of wing rotation on unsteady aerodynamic performance at low Reynolds numbers. *Journal of Experimental Biology*, 192:179–206, 1994.

[20] M.H. Dickinson. Force generation in locomotion: unsteady mechanisms. *Amer. Zool.*, 36:537–554, 1996.

[21] M.H. Dickinson. Haltere-mediated equilibrium reflexes of the fruit fly, *Drosophila melanogaster*. *Phil. Trans. R. Soc. Lond. B*, 354(903-916), 1999.

[22] M.H. Dickinson. Unsteady mechanicsms of force generation in aquatic and aerial locomotion. *American Zoology*, 56(537-554), 1999.

[23] M.H. Dickinson and F. O. Lehmann. The active control of wing rotation by *Drosophila*. *Journal of Experimental Biology*, 182:173–189, 1993.

[24] M.H. Dickinson, F.-O Lehmann, and S.S. Sane. Wing rotation and the aerodynamic basis of insect flight. *Science*, 284(5422), 1999.

[25] M.H. Dickinson and M.S. Tu. The function of dipteran flight muscle. *Comp. Biochem. Physiol. A*, 116(3):223–238, 1997.

[26] R. Dudley. *The Biomechanics of Insect Flight: Form, Function, Evolution*. Princeton: University Press, 2000.

[27] C.P. Ellington. The aerodynamics of hovering insect flight. I-VI. *Phil. Trans. R. Soc. London B*, 305:1–181, 1984.

[28] C.P. Ellington, A.P. Willmott, C. van den Berg, and A.L.R Thomas. Leading-edge vortices in insect flight. *Nature*, 384:626–630, 1996.

[29] A. Fayyazuddin and M.H. Dickinson. Halter afferents provide direct, electrotonic input to a steering motor neuron of the blowfly. *J. of Neuroscience*, 16(16):5225–5232, 1996.

[30] G. Fraenkel and J.W.S. Pringle. Halteres of flies as gyroscopic organs of equilibrium. *Nature*, 141:919–921, 1938.

[31] S.N. Fry, R. Sayaman, and M. H. Dickinson. The aerodynamics of free-flight maneuvers in *Drosophila*. *Science*, 300(5618):495–498, April 2003.

[32] R.J. Full, T. Kubow, J. Schmitt, P. Holmes, and D. Koditschek. Quantifying dynamic stability and maneuverability in legged locomotion. *Int. and Comp. Biology*, 42:129–157, 2002.

[33] Y.C. Fung. *An Introduction to the Theory of Aeroelasticity*. New York, Dover, 1969.

[34] R. Hengstenberg. Mechanosensory control of compensatory head roll during flight in the blowfly *Calliphora erythrocephala. J. Comp. Physiol. A*, 163:151–165, 1988.

[35] R. Hengstenberg. Multisensory control in insect oculomotor systems. *Visual Motion and its Role in the Stabilization of Gaze*, pages 285–298, 1993.

[36] R.G. Kastberger. The ocelli control the flight course in honeybees. *Physiological Entomology*, 15:337–346, 1990.

[37] H.K. Khalil. *Nonlinear Systems*. Prentice Hall, third edition, 2002.

[38] P.V. Kokotovic, H.K. Khalil, and J.O'Reilly. *Singular pertubations methods in Control: Analysis and Design*. SIAM, 1999.

[39] T. J. Koo, B. Sinopoli, A. Sangiovanni-Vincentelli, and S. Sastry. A formal approach to reactive system design: A UAV flight management system design example. In *Proceedings of IEEE International symposium on Computer-Aided Control System Design*, Kohala Coast, Hawaii, U.S.A, 1999.

[40] R.G. Krapp, B. Hengstenberg, and R. Hengstenberg. Dendritic structure and receptive-field organization of optic flow processing interneurons in the fly. *Journal of Neurophysiology*, 79:1902–1917, 1998.

[41] R.G. Krapp and R. Hengstenberg. Estimation of self-motion by optic flow processing in single visual interneurons. *Nature*, 384:463–466, 1996.

[42] A.M. Kuethe and C.Y. Chow. *Foundations of Aerodynamics*. John Wiley and Sons, 1986.

[43] F.O. Lehemann and M.H. Dickinson. The control of wing kinematics and flight forces in fruit flies *Drosophila*. *Journal of Experimental Biology*, 201(3):385–401, 1998.

[44] N.E. Leonard. Periodic forcing, dynamics and control of underactuated spacecraft and underwater vehicles. In *Proceedings of 34th IEEE Conference on Decision and Control*, 1995.

[45] J.E. Marsden and T.S. Ratiu. *Introduction to Mechanics and Symmetry*, volume 17 of *TAM*. Springer-Verlag, 1994.

[46] S. Martínez, J. Cortés, and F. Bullo. On analysis and design of oscillatory control systems. *IEEE Transactions Automation and Control*, 2003.

[47] R.J. Mason. *Fluid Locomotion and Trajectory Planning for Shape-Changing Robots*. PhD thesis, California Institute of Technology, 2003.

[48] K.A. McIsaac and J.P. Ostrowski. Motion planning for anguilliform locomotion. *IEEE Transactions on Robotics and Automation*, 19(4):637–652, 2003.

[49] M. Mizunami. *Atlas of Arthropod Sensory Receptors: Dynamic Morphology in Relation to Function*, chapter Ocelli, pages 71–78. Springer, 1999.

[50] K.A. Morgansen, V. Duindam, R.J. Mason, J.W. Burdick, and R.M. Murray. Nonlinear control methods for planar carangiform robot fish locomotion. In *Proc of the IEEE International Conference on Robotics and Automation*, Seoul, South Korea, May 2001.

[51] B. Motazed, D. Vos, and M. Drela. Aerodynamics and flight control design for hovering MAVs. In *Proceedings of American Control Conference*, Philadelphia, PA, June 1998.

[52] R. M. Murray, Z. Li, and S.S. Sastry. *A Mathematical Introduction to Robotic Manipulation*. CRC Press, 1994.

[53] R. M. Murray and S.S. Sastry. Nonholonommic motion planning: Steering using sinusoids. *IEEE Transaction on Automation and Control*, 38(5):700–716, 1993.

[54] G. Nalbach. The halteres of the blowfly *Calliphora*: I. kinematics and dynamics. *Journal of Comparative Physiology A*, 173:293–300, 1993.

[55] G. Nalbach and R. Hengstenberg. The halteres of the blowfly *Calliphora*: Ii. three-dimensional organization of compensatory reactions to real and simulated rotations. *Journal of Comparative Physiology A*, 175:695–708, 1994.

[56] T.R. Neumann. Modeling insect compound eyes: Space-variant spherical vision. In T. Poggio H.H. Blthoff, S.-W. Lee and C. Wallraven, editors, *Proceedings of the 2nd International Workshop on Biologically Motivated Computer Vision BMCV*, volume 2525, pages 360–367, Berlin, Germany, 2002. Springer-Verlag.

[57] T.R. Neumann and H.H. Blthoff. Behavior-oriented vision for biomimetic flight control. In *Proceedings of the EPSRC/BBSRC International Workshop on Biologically Inspired Robotics: The Legacy of W. Grey Walter*, pages 196–203, HP Labs Bristol, UK, 2002.

[58] J. Ostrowski and J.W. Burdick. The mechanics and control of undulatory locomotion. *International Journal of Robotics Research*, 17(7):683–701, 1998.

[59] R. Ramamurti and W.C. Sandberg. A three-dimensional computational study of the aerodynamic mechanisms of insect flight. *Journal of Experimental Biology*, 205(10):1507–1518, 2002.

[60] W. Reichardt and T. Poggio. Visual control of orientation behavior in the fly. Part I: A quantitative analysis. *Quarterly Review of Biophysics*, 3:311–375, 1976.

[61] J.A. Sanders and F. Verhulst. *Averaging methods in Nonlinear Dynamical Systems*. Springer-Verlag, New York, N.Y., 1985.

[62] G. Sandini, F. Panerai, and F.A. Miles. The role of inertial and visual mechanisms in the stabilization of gaze in natural and artificial systems. *Motion Vision - Computational, Neural, and Ecological Constraints*, 2001.

[63] S.P. Sane and M.H. Dickinson. The control of flight force by a flapping wing: Lift and drag production. *Journal of Experimental Biology*, 204(15):2607–2626, 2001.

[64] S.P. Sane and M.H. Dickinson. The aerodynamic effects of wing rotation and a revised quasi-steady model of flapping flight. *Journal of Experimental Biology*, 205:10871096, 2002.

[65] S.S. Sastry. *Nonlinear systems: analysis, stability and control*. Springer-Verlag, New York, N.Y., 1999.

[66] S.S. Sastry and M. Bodson. *Adaptive Control: Stability, Convergence and Robustness*. Prentice Hall, 1988.

[67] L. Schenato, W.C. Wu, and S.S. Sastry. Attitude control for a micromechanical flying insect via sensor output feedback. To appear in *IEEE Transactions on Robotics and Automation*, April 2004.

[68] H. Schuppe and R. Hengstenberg. Optical properties of the ocelli of *Calliphora erythrocephala* and their role in the dorsal light response. *Journal of Comparative Biology A*, 173:143–149, 1993.

[69] A. Sherman and M.H. Dickinson. A comparison of visual and haltere-mediated equilibrium reflexes in the fruit fly *Drosophila melanogaster*. *Journal of Experimental Biology*, 206:295–302, 2003.

[70] M. Sitti, D. Campolo, J. Yan, R.S. Fearing, T. Su, D. Taylor, and T. Sands. Development of PZT and PZN-PT based unimorph actuators for micromechanical flapping mechanisms. In *Proc. of the IEEE International Conference on Robotics and Automation*, pages 3839–3846, Seoul, South Korea, May 2001.

[71] M. Sun and J. Tang. Lift and power requirements of hovering flight in *Drosophila virilis*. *Journal of Experimental Biology*, 205(10):2413–2427, 2002.

[72] H.J. Sussmann. New differential geometric methods in nonholonomic path finding. *Systems, Models, and Feedback: Theory and Applications*, pages 365–384, 1992.

[73] H.J. Sussmann and W Liu. Limits of highly oscillatory controls and the approximation of general paths by admissible trajectories. In *Proceedings of the 30th IEEE Conference on Decision and Control*, volume 1, pages 437–42, 2001.

[74] L. Tammero and M.H. Dickinson. The influence of visual landscape on the free flight behavior of the fruit fly *Drosophila melanogaster*. *Journal of Experimental Biology*, 205:327–343, 2002.

[75] L. Tammero and M.H. Dickinson. Collision avoidance and landing responses are mediated by separate pathways in the fruit fly, *Drosophila melanogaster*. *Journal of Experimental Biology*, in press.

[76] C.P. Taylor. Contribution of compound eyes and ocelli to steering of locusts in flight: I-II. *Journal of Experimental Biology*, 93:1–31, 1981.

[77] G.K. Taylor. Mechanics and aerodynamics of insect flight control. *Biol. Rev.*, 76(4):449–471, 2001.

[78] M.S. Tu and M. H. Dickinson. The control of wing kinematics by two steering muscles of the blowfly *Calliphora vicina*.

[79] P. Vela, K. Morgansen, and J.W. Burdick. Trajectory stabilization for a planar carangiform fish. In *Proc of the IEEE International Conference on Robotics and Automation*, Washington DC, U.S.A, May 2002.

[80] P.A. Vela. *Averaging and Control of Nonlinear systems (with application to Biomimetic Locomotion)*. PhD thesis, California Institute of Technology, 2003.

[81] H. Wagner. Flight performance and visual control of the free-flying housefly *Musca domestica L*. I. Organization of the flight motor. *Philosophical Transactions of the Royal Society of London. Series B*, 312:527–551, 1986.

[82] Micromechanical Flying Insect website. http://robotics.eecs.berkeley.edu/~ronf/mfi.html.

[83] B. Wie. *Space vehicle dynamics and control*. AIAA Educational Series, Reston, VA, 1998.

[84] A.P. Willmott, C.P Ellington, C. van den Berg, and A.L.R Thomas. Flow visualization and unsteady aerodynamics in the flight of the hawkmoth *Manduca sexta*. *Phil. Trans. R. Soc. Lond. B*, 352:303–316, 1997.

[85] T.W. Wu. On theoretical modeling of aquatic and aerial animal locomotion. *Advances in Applied Mechanics*, 38:292–353, 2001.

[86] J. Yan. *Design, Fabrication and Wing Force Control for a Micromechanical Flying Insect*. PhD thesis, University of California at Berkeley, 2002.

[87] J. Yan, R. Wood, S. Avandhanula, M. Sitti, and R.S. Fearing. Towards flapping wing control for a micromechanical flying insect. In *Proc. of the IEEE International Conference on Robotics and Automation*, volume 4, pages 3901–3908, 2001.

[88] J.M. Zanker. On the mechanism of speed and altitude control in *Drosophila melanogaster*. *Physiological Entomology*, 13:351–361, 1988.

[89] L. Zhou, J.M. Kahn, and K.S.J. Pister. Corner-cube reflectors based on structure-assisted assembly for free-space optical communication. *Journal of Microelectromechanical Systems*, 12(3):233–242, June 2003.